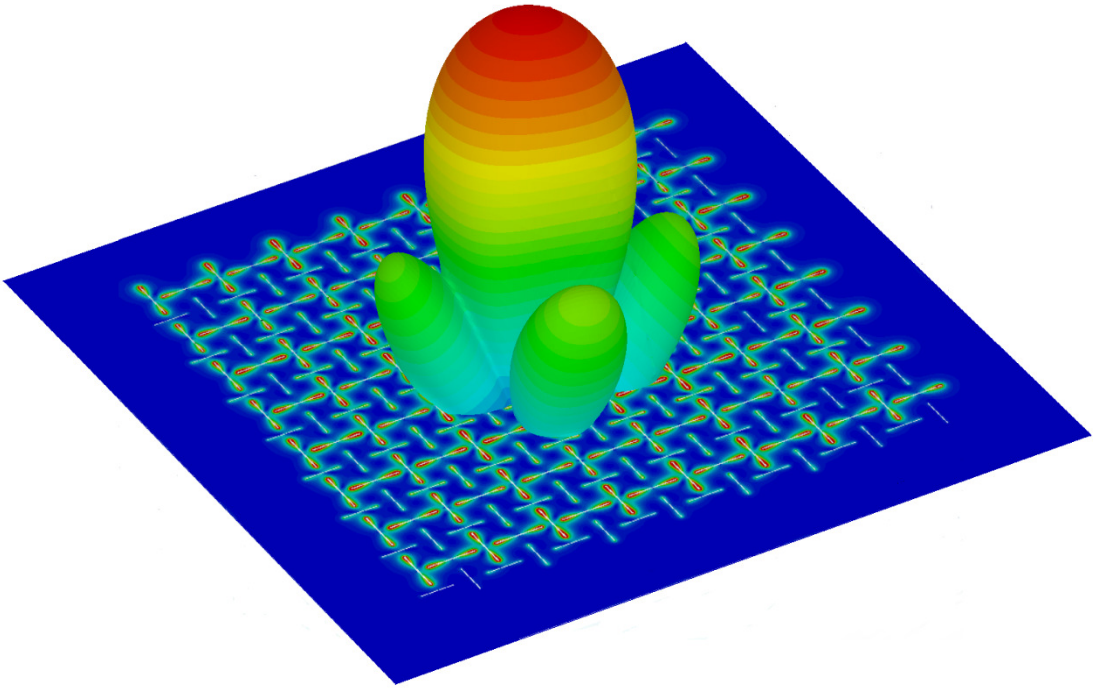

Ultrasensitive Superconducting Cold-Electron Bolometer Coupled to Multi-frequency Phased Antenna Array for Polarization Detection of the Cosmic Microwave Background

Thesis for the Degree of Erasmus Mundus Master of Nanoscience and Nanotechnology

MOHAMED SALEH

Quantum Device Physics Laboratory
Department of Microtechnology and Nanoscience-MC2
CHALMERS UNIVERSITY OF TECHNOLOGY
Gothenburg, Sweden, 2014

Ultrasensitive Superconducting Cold-Electron Bolometer Coupled to Multi-frequency Phased Antenna Array for Polarization Detection of the Cosmic Microwave Background

MOHAMED SALEH

Promoter:
Prof. Leonid Kuzmin
Chalmers University of technology, Sweden

Co-promoter:
Prof. Jean-Pierre Locquet
KU Leuven, Belgium

External Examiner:
Dr. Serguei Cherednichenko
Chalmers University of technology, Sweden

Quantum Device Physics Laboratory
Department of Microtechnology and Nanoscience – MC2
CHALMERS UNIVERSITY OF TECHNOLOGY
Gothenburg, Sweden 2014

Ultrasensitive Superconducting Cold-Electron Bolometer
Coupled to Multi-frequency Phased Antenna Array for
Polarization Detection of the Cosmic Microwave Background
MOHAMED SALEH

Quantum Device Physics Laboratory
Department of Microtechnology and Nanoscience – MC2
Chalmers University of Technology
SE-412 96 Gothenburg
Sweden
Telephone + 46 (0)73-758 0788

Cover:
Current distribution and beam pattern of the rectangular dual polarized phased array of slot antennas working at 75 GHz and 105 GHz simulated using CST MWS.

Printed by Reproservice
Gothenburg, Sweden 2014

Contents

List of Figures

List of Tables

This page intentionally contains only this sentence.

Abstract

We describe the design and simulation of a novel dual-polarized multi-frequency single-pixel for next-generation Cosmic Microwave Background (CMB) polarization detection. The pixel consists of a phased array of planar antennas known as slot antennas coupled to millimeter-wave cryogenic detector by superconducting transmission lines. The pixel separates the incoming radiation into two linear polarizations with high polarization purity and operates at two frequencies (75 GHz and 105 GHz) as well. This completely lithographed planar technology will enable us to squeeze the size of the focal plane to avoid aberration problems. This will also enable us to realize bolometer arrays with thousands of pixels needed to meet the sensitivity requirements of future CMB polarization experiments and to achieve better resolutions and higher scan speeds. Having multiple frequencies is important to differentiate the CMB from the galactic foreground contamination. Those goals are difficult to achieve with the current technology which uses feed horn for each pixel.

The detector is a superconducting Cold Electron Bolometer (CEB), which have several advantages over current technologies. The main component of the CEB is a Normal-Insulator-Superconductor (NIS) tunnel junction, which acts as a thermometer. The CEB could implement an additional spectral filtering feature, which obviates the need for external filters.

This technology is a candidate for use in the European Space Agency (ESA) Cosmic Vision Program (2015-2025) to detect the B-mode of the CMB, which will be considered as an indirect detection of the gravitational waves that followed the Big Bang.

This page intentionally contains only this sentence.

Acknowledgements

I would like thank my examiner and promoter, Prof. Leonid Kuzmin, for giving me the opportunity to be a member of his group. He was always supportive and had time to discuss the results and guide me no matter how busy he was. He was very friendly; he used to bring cakes during meetings, and invite the group members to lunch from time to time.

I would also like to thank Anna Gordeeva for co-supervision and experimental help.

Many thanks to Alexander Sobolev for his insights and help in CST simulations.

I would like to express my gratitude to Sumedh Mahashabde for his continuous encouragement and motivation. I appreciate your smartness.

I consider myself lucky to work in an environment where the welfare of the researcher is of a high priority. Thanks MC2 for the cake parties, the fruits, and the unlimited coffee.

My thanks to MC2 IT support, especially Henric Fjellstedt, who was always available to install the software packages needed to complete this project.

This page intentionally contains only this sentence.

Chapter 1

Introduction

1.1 The Cosmic Microwave Background

Since the speed of light is finite, the images of far objects are late. For example, the image of our sun is eight minutes old, whereas the image of the nearest galaxy is 2 million years old! Therefore, a natural question arises: what is the oldest thing that we can observe? Fortunately, this thing turned out to be there. It is a dim radiation surrounding us. This light is the so-called Cosmic Microwave Background (CMB). The CMB is thought to have emerged about 13.7 billion years ago during the formation of our universe. Therefore, to understand the origin of CMB, we must understand how our early universe was. The next subsection elucidates briefly about the early universe.

1.1.1 The Early Universe

After 10^{-36} seconds of the Big Bang “13.7 billion years ago”, and for a short period of about 10^{-33} seconds, the universe is thought to have expanded exponentially to reach 10^{78} of its initial volume, as shown if Figure 1.1. This theory is known as Inflation theory, and it is a key theory in the Big Bang cosmological model of the universe.

The rapid expansion of universe during inflation have created ripples in the space known as primordial gravitational waves. Just as moving charges can generate electromagnetic waves, moving masses can generate gravitational waves according to General Relativity as well.

The Big Bang released hot and dense photons, electrons, and protons. At this point, photons scattered strongly by the charged electrons and protons and were not able to escape [1], so the universe was opaque. The universe cooled gradually, and after 378,000 years of the Big Bang, it was cool enough that electrons could bind to protons to form

---

[1] Charged particles are accelerated by the electric field component of the incident radiation (photons) and emit radiation at the same frequency as the incident wave, therefore the photons get scattered.

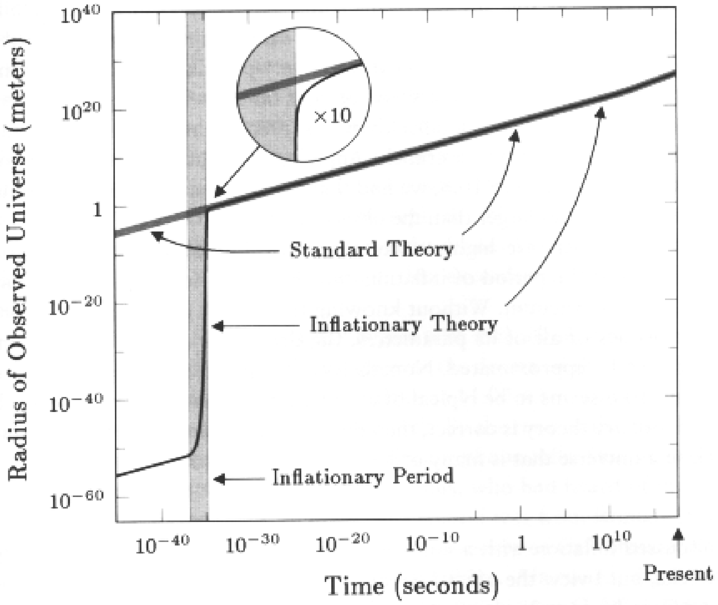

Figure 1.1 – The inflation model. The universe has expanded exponentially within a very tiny fraction of a second.

neutral hydrogen atoms. After this recombination, the scattering of photons decreased extremely since the vast majority of particles became neutral atoms rather than charged particles. The universe then became transparent and the photons could escape. Those photons still travel freely in the universe till now and they constitute the CMB radiation that we can observe today. Figure 1.2 shows a depiction of the origin of the CMB.

The CMB has the spectrum of a black body that has a temperature of 2.725 K and peaks at about 160.2 GHz. Of course it has cooled during the past 14 billion year till it reached this temperature.

1.2 Anisotropies in CMB

The CMB varies from a region to another in the sky. This spatial variation provides a snapshot of the early universe. There are two kinds of variations: intensity and polarization.

1.2.1 Temperature Anisotropy

As was mentioned before, the average temperature of CMB is 2.725 K. However, the temperature of the CMB is anisotropic. It is not the same when looking in different directions in the sky. It has small variations at the level of about ±0.00335 K. CMB temperature anisotropies dictate that there were density fluctuations in the early universe

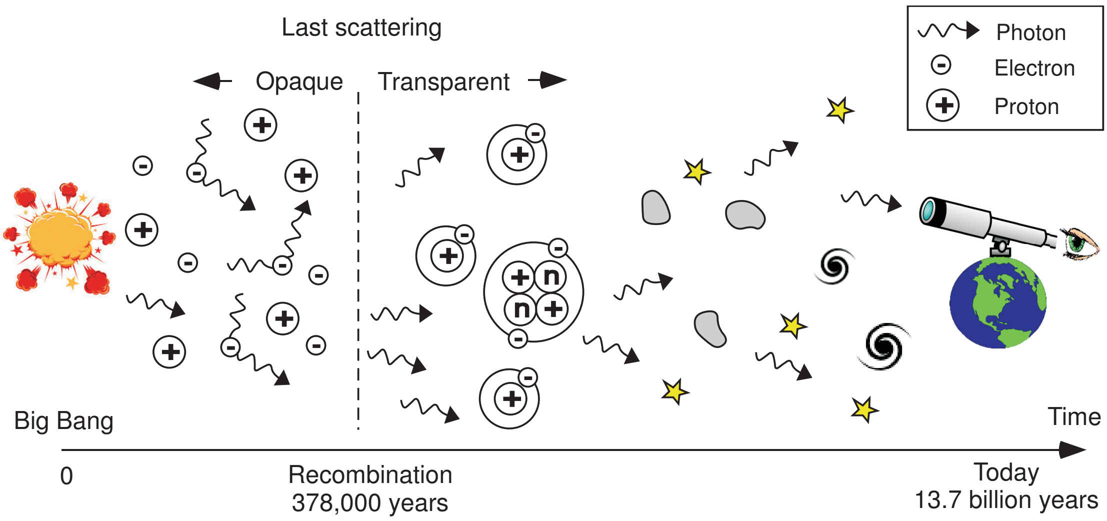

Figure 1.2 – Cartoon illustration of the origin of CMB. Before recombination, photons scattered strongly on the charged particles. After the charged particles were bound to form neutral atoms, the universe became transparent and CMB phototns could escape. It is those photon that we see today as CMB radiation. The neutral atoms joined each other due to gravity to form stars and galaxies.

known as “primordial fluctuations”.

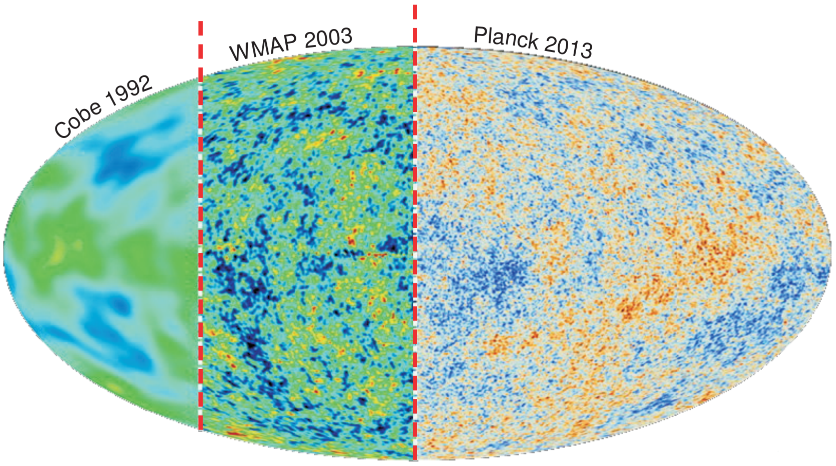

Figure 1.3 – Measured CMB Temperature Anisotropies across the sky. The figure shows how the resolution is being enhanced with time due to advancements in detectors technologies.

This pattern gives information about initial conditions of the expansion. The Big Bang model predicts in detail these anisotropies. Therefore, those measured fluctuations lend credence to the Big Bang model in general. Figure 1.3 shows the measured CMB temperature anisotropy and how the accuracy and resolution are improving.

These anisotropies were first observed in 1992 by The NASA COBE . The team received the 2006 Nobel Prize in physics for this achievement.

1.2.2 Polarization Anisotropy

It has been recently detected that the CMB radiation is also polarized besides being anisotropic in temperature. Within a short period before the end of recombination, phonons were scattered by the still free electrons left. This scattering mechanism is known as Thomson Scattering and it has caused the CMB radiation to be polarized. Thomson scattering is the scattering of electromagnetic waves by a free charged particles, where the electric field component of the incident radiation accelerates the charged particles in the direction of the electric field. This movement of the charged particles in turn causes emission of radiation at the same frequency as the incident wave, and thus the wave gets scattered.

Consider incident unpolarized light on a charged particle, the two polarization components accelerate the particle in two perpendicular directions. However, since light cannot have a component polarized along its direction of propagation, only one linear polarization is scattered. Particle acceleration in a direction parallel to the direction of propagation of the scattered light produces no radiation. In other words, an unpolarized incident wave becomes polarized after being scattered by a charged particle. The CMB polarization is not constant through the sky. Temperature anisotropies gave rise to variation in polarization magnitudes and orientations causing CMB polarization anisotropy.

The polarization of CMB can be mathematically decomposed into what is called the E-mode and the B-mode. The E-mode describes magnitude changes “or gradient” of polarization, while the B-mode describes the rotation ”or curl” of CMB polarization. Those two modes originated from different physical origins and carry complementary information about the early universe. The B-mode is the subject of next section.

Despite the fact that CMB polarization has been long predicted, it has remained undetected until recently when the DASI team first detected the E-mode polarization in 2002 [12]. The B-mode polarization is predicted to have been produced by the gravitational waves generated during the inflation. Therefore, the detection of the B-mode signal would represent the final and definitive confirmation of the inflation model and evidence of primordial gravitational waves.

By studying the CMB polarization pattern, we can know about the universe in its first tiny fraction of a second, among other things. The precise measurement of the B-mode will constrain possible inflation scenarios and fix its energy scale, which would be useful for developing theories of quantum gravity. The signal can also be used to determine the masses of the different types of neutrinos.

1.3 The B-mode Detection

Detecting B-modes is an extremely challenging task. It is extremely faint signal; whilst the temperature fluctuations of the CMB are around 160 μK, the E-mode signal is at an amplitude of order of 8 μK, and the fluctuations of B-mode signal is of the order 0.1 μK.

B-modes have been measured by South Pole Telescope in 2013 [18], and in 2014 by BICEP2 experiment [1]. However, more sensitivity and multi-frequency measurements are still needed.

1.3.1 Disadvantages of Current Technologies

Systems with millimetre-wave detectors require beam-collimation to control their illumination from the sky. The corrugated horn [9], see Figure 1.4, has been the standard antenna for this purpose for a long time due to the fact that its radiation patterns are rotationally symmetric , and it exhibits low cross-polarization (-30dB) [2], and high coupling efficiency to the beam. The corrugated horn is shown in Figure 1.4.

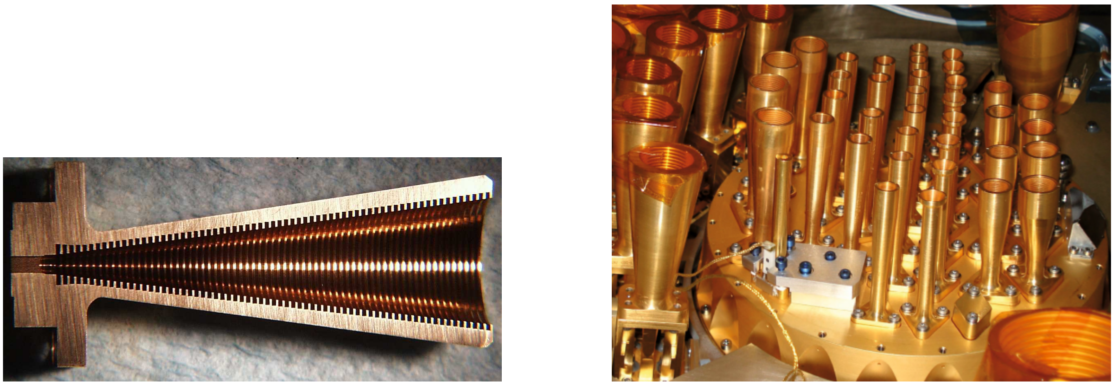

(a) **(b)**

Figure 1.4 – (a) Cross-section of a corrugated horn antenna. (b) The Focal Plane of Planck experiment [30].

This technology is very well established in CMB missions and has been the main beam forming technology in CMB experiments to date due to its unsurpassed RF performance. All the experiments that detected CMB E-mode polarization have used corrugated feed horns. These include Planck [31], WMAP [4], CAPMAP [3], DASI [12], CBI [44], Boomerang [23], and QUAD [19].

Future CMB polarization experiments will require more detectors "thousands" and measuring at larger range of frequencies. Unfortunately, corrugated feed horns have

---

[2] Cross polarization is simply the ratio between the power radiated in the unwanted polarization to the power radiated in the desired polarization, see Chapter 5 for more details.

disadvantages with increasing the number of detectors, and with increasing or lowering the frequency. The following are the disadvantages of feed horn technology

- As the number of detectors increase, more and more horns are needed to populate the focal plane [3]. Those heavy metal horns will create a significant mass and volume penalty. They have to withstand accelerations during launch. They are too heavy to be cooled to very low temperatures that detectors work at.
- Manufacturing detailed corrugations is limited by cost and time for the production of large detector arrays.
- At high frequencies "short wavelengths", the horns are relatively small and fabricating the corrugated structures is even harder.

1.3.2 Future Technologies

Clearly, new technologies are required to realize focal planes with lower mass, lower cost, and less fabrication time. An alternative is to replace the horns with planar antennas. This will allow us to have entirely lithographed focal planes, and thus large and dense detector arrays could be realized.

Planar antennas have several advantages over conventional feed horns such as

- Densely packed focal planes are possible.
- Low cost and low mass.
- Parallel fabrication.
- Fabrication simplicity.
- Mechanical robustness.
- Immunity to misalignment to the telescope optics.
- Better immunity of the detectors to cosmic rays.
- Can be dual-polarized operating in two polarizations simultaneously.
- Multiple frequency bands.
- Can include some level of spectral filtering.

---

[3] The focal plane is the plane of the detectors, it lies in the focus of the telescope optics, and hence the name.

1.4 Motivation for This Work

The detection of the B-modes component of the CMB is now the objective of the next generation CMB experiments. Those experiments will be required to reach an exquisite and unprecedented levels of sensitivity required to detect B-modes. To achieve these serious experimental challenging goals, extremely sensitive and ultra-low noise detectors are required. The pixel size also needs to be squeezed. This will help to avoid aberration problems and will enable us to populate the instrument focal plane with thousands of those detectors for increased resolution and scan speeds. Furthermore, multi-frequency coverage will be required for removal of foreground contamination, which is also polarized.

The goal of this thesis is double fold: firstly, to model the Cold-Electron Bolometer (a kind of sensitive superconducting detector) that have been fabricated in Chalmers University of Technology. Secondly, investigation of an equivalent planar antenna which would replace conventional horn antennas to achieve increased packing density in the focal plane. This antenna should also allow for multi-frequency operations and simultaneous measurement of two orthogonal polarizations.

In the framework of the European Space Agency (ESA) Cosmic Vision Program (2015-2025), Chalmers University of Technology will lead the design and manufacture of a planar demonstrator (both the detector and the planar antenna) for next generation B-mode experiments.

1.5 Structure of the Thesis

The thesis is structured as follows. Chapter 2 briefly touches upon the relevant basics of superconductivity that are necessary to understand how our bolometer works. Chapter 3 explains the idea behind bolometers generally and the Cold-Electron Bolometer especially. In Chapter 4, the modeling of the device is shown and the theoretically generated curves are fitted to the experimentally measured ones. Chapter 5 deals with the design and simulation of the antenna and antenna array that is coupled to the bolometer.

This page intentionally contains only this sentence.

Chapter 2

Superconductivity

2.1 Superconductivity Basics

In this chapter, we will cover some theoretical basics that will help to understand how a Cold-Electron Bolometer works. First, basics of superconductivity that are relevant are explained. Then the working principle of the Superconductor-Insulator-Normal tunnel junction, the heart of the Bolometer, will be touched upon. The concept of surface impedance of superconductors is finally introduced.

Superconductivity is a quantum phenomenon characterized by the complete loss of resistivity in certain kinds of metals when the temperature of the metal is lower than a threshold temperature, known as the critical temperature T_c. In 1957 Bardeen, Cooper and Schrieffer developed a microscopic theory of superconductivity that can explain mostly every property of conventional low-T_c superconductors [1] . In the next section we give a brief introduction to the BCS theory, with only the results needed reviewed.

2.1.1 BCS Theory

BCS Theory postulates that electrons in a superconductor weakly attract each other due to electron-phonon interaction at low temperatures. When a fast-moving electron passes through a lattice of heavy and stationary positive ion cores, it will attract the nearby ions. This causes lattice distortion in the vicinity of this electron and ions move slightly towards each other, increasing the positive charge density in this region. A second electron will then feel this increase in the positive charge and will move to lower its potential energy, thus becoming effectively attracted to the first electron. When the temperature is low enough, the attraction force overcome the Coulumb repulsive force. The main consequence of this weak electron-electron attraction is the formation of bound electron pairs known as Cooper Pairs.

---

[1] High-T_c superconductors cannot be explained by BCS Theory.

The two electrons forming Cooper Pairs have equal but opposite momentum and spin, therefore Cooper Pairs are bosons (zero spin) and will occupy the same lower energy state known as BCS ground state at zero temperature. They are able to carry non-dissipative super current.

2.1.2 Superconducting Gap

The binding energy per electron of a Cooper pair is called the energy gap Δ. Therefore, breaking a pair requires energy of 2Δ. Stable pair states cannot exist above the BCS ground state, so the minimum energy needed to create an excited state is that required to break a pair and remove it from the ground state, i.e. 2Δ.

BCS theory relates the gap Δ at zero temperature to the superconductor's critical temperature as follows:

$$\Delta(0) = 1.76 K_B T_C \tag{2.1.2.1}$$

Where K_B is the Boltzmann constant.

2.1.3 Temperature Dependence of The Gap

One of the BCS predictions is that the gap energy Δ is temperature dependent. The temperature dependence of the gap can be obtained to a good approximation from the simple equation

$$\frac{\Delta(T)}{\Delta(0)} = \sqrt{cos\left(\frac{\pi}{2}\frac{T}{T_C}\right)} \tag{2.1.3.1}$$

which agrees fairly well with experimental measurements. This gap temperature dependence is shown in Figure 2.1.

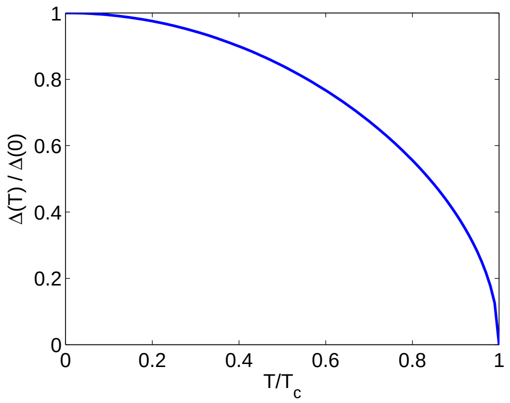

Figure 2.1 – Superconducting gap temperature dependence.

2.1.4 Quasiparticles and The Semiconductor Picture

The two electrons comprising the Cooper pair occupy the state $(\vec{k}\uparrow, -\vec{k}\downarrow)$, where $\vec{k}$ is the momentum and $\uparrow$ is the spin.

At zero temperature all electrons are paired up in Cooper pairs, but at a finite temperature some electrons exist as excitations. The excited k state implies that $(\vec{k}\uparrow$ is occupied, and $(-\vec{k}\downarrow)$ is empty. This picture has an analogy to semiconductors if we see this as creation of electron-like and hole-like excitations. However, in case of superconductors, both the excitations have charge of –e. These particles are called quasiparticles. Breaking a pair corresponds to exciting a quasiparticle above the energy gap.

It follows that the superconductor quasiparticle excitation spectrum is analogous to the semiconductor density of states. This is illustrated in Figure 2.2b of the next subsection, where the BCS ground state of the superconductor corresponds to the ground state of the superconductor. The filled band is the valence-like band formed by the bound pairs at energies Δ below the Fermi level, whereas the empty band is the conduction-like band formed by the broken pairs at energies Δ above the Fermi level. An energy gap of 2Δ separates the two bands.

At excitation, pairs of quasiparticles are created, the hole-like particles in the valence band and the electron-like particles in the conduction band. The Fermi energy E_F lies exactly in the middle of the gap since there are always equal number of hole-like and electron-like excitations.

This semiconductor picture is very helpful in understanding the tunneling properties of the NIS tunnel junction, and its utility will come to full expression in the next section.

2.1.5 BCS Density of States

The BCS theory gives a density of states of

$$D_S(E) = D_S(0)\frac{|E|}{\sqrt{E^2 - \Delta^2}} \qquad (2.1.5.1)$$

where $D_S(0)$ is the density of states “two-spin“ at the Fermi level when the superconductor is in its normal state (above T_c). Figure 2.2a shows the normalized BCS density of states.

The number of occupied states can be found by multiplying the Fermi distribution by the density of states. Figure 2.2b shows the quasiparticle occupation of a superconductor at a finite temperature below T_c.

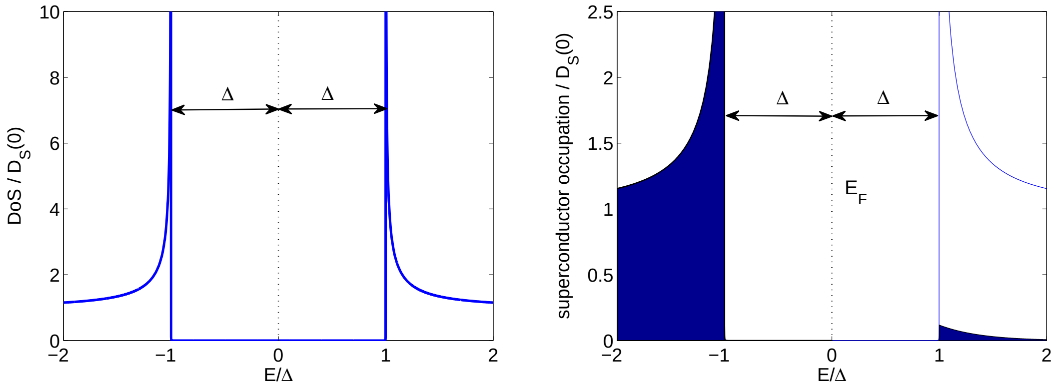

(a) (b)

Figure 2.2 – (a) The normalized BCS density of states. (b) Quasiparticle occupation.

There are no quasiparticles allowed in the gap. The lack of states in the region $E_F < E < E_F + \Delta$ is compensated by a singularity at the density of states at the gap edges at energy $E = E_F \pm \Delta$ and the DOS diverges. This leads to the non-linear NIS IV curve, as we will see later.

2.1.6 Length Scales of Superconductivity

The following are the characteristic lengths of a superconductor

- London penetration depth λ_L: A superconductor excludes the magnetic field. The magnetic field falls off exponentially inside the superconductor. The penetration depth characterizes the distance over which the magnetic field decays to 1/e of its value at the surface of the superconductor. For typical superconductors, λ_L ranges from 50 to 500 nm.

- Coherence length ζ_0: It is the distance over which the correlation between the two electrons forming a cooper pair persists. It could be thought of as the size of the cooper pair. ζ_0 typically ranges from 5 to 100 nm.

We will see in Chapter 4 that these characteristic lengths, along with others, determine the method by which we shall calculate the losses in the superconductor.

2.2 The NIS Tunnel Junction

A Normal-Insulator-Superconductor tunnel junction (NIS) consists of a very thin layer of insulator (few nm) sandwiched between two electrodes. One electrode is a normal metal, while the other electrode is a superconductor. In this case, tunneling of electrons between the two electrodes is possible. Tunneling is a quantum mechanical process in which the classically impossible penetration of potential barrier is allowed. Tunneling in superconductors was first demonstrated by in 1960 Giaever [15], who was awarded the Nobel Prize in 1973. In this section, we will briefly outline the basic theoretical concepts of NIS tunneling and how it works as a microrefregirator.

2.2.1 NIS Junction as an Electron Cooler

In this subsection we will show how an NIS tunnel junction can be used as an electron microrefregirator by removing power from the normal metal electrode. This technique was first demonstrated in 1994 [34, 40]. Figure 2.3 shows the structure of an unbiased NIS junction along with its energy band diagram.

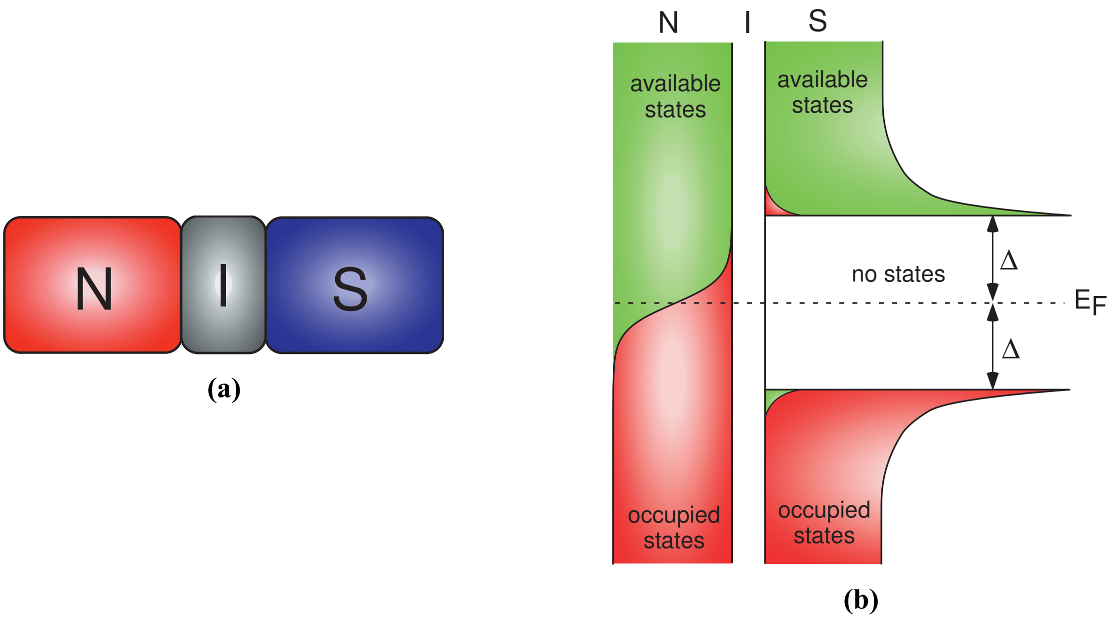

Figure 2.3 – The unbiased NIS junction. (a) Structure. (b) Energy band diagram.

For zero and low biases, the occupied states of the normal metal lie within the energy gap of the superconductor. Electrons in these states cannot tunnel because there are no available states in the superconductor.

However, for biases near $V_b = \Delta/e$, as shown if Figure 2.4, the occupied states in the Fermi distribution tail in the normal metal are above the gap edge (have energy greater than Δ) and can contribute to a tunneling current. A further small increase in the bias voltage will cause dramatic increase in the tunneling current since there is a large number of available states directly above the gap.

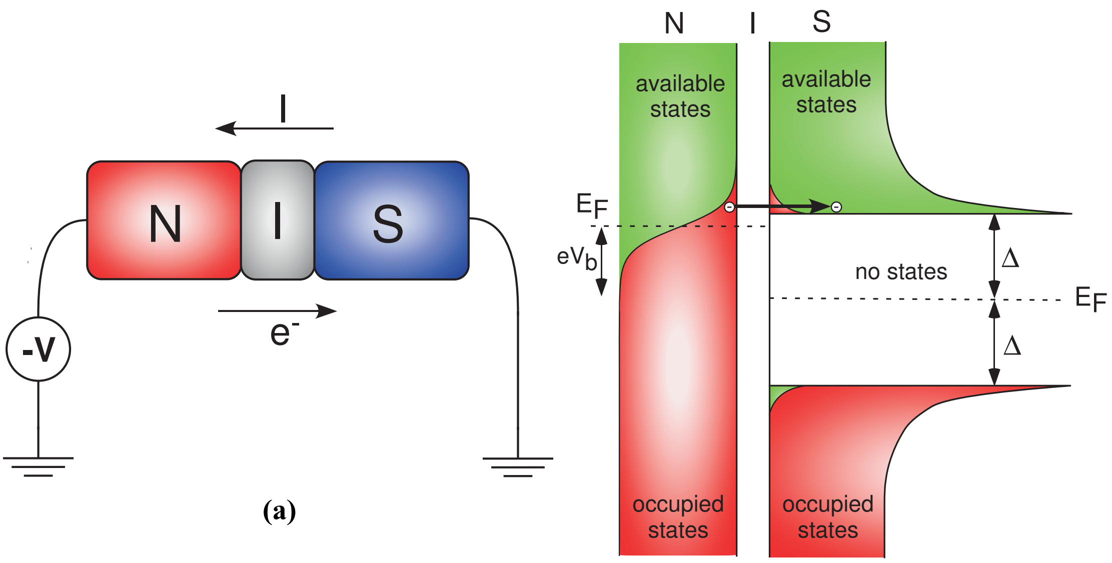

(a) **(b)**

Figure 2.4 – The biased NIS junction. (a) Structure. (b) Energy band diagram.

Therefore, a NIS junction extracts electrons having energy higher than the Fermi energy (hot electrons) from the normal metal. The removal of those high-energy electrons is corresponds to cooling the electrons in the normal metal electrode. Temperatures below 100 mK are achievable.

2.2.2 NIS Tunneling Current

As mentioned before, NIS junctions have a dependence of current on the temperature of the normal electrode. The temperature rise of the normal electrode is measured from this current temperature dependence. To find an expression of the NIS tunneling current, we first start by evaluating the tunneling rates of charge carriers. The tunneling rate from the normal electrode to the superconducting electrode $\Gamma_{N\to S}$ is

$$\Gamma_{N\to S}(V_b, T_N, T_S) = T D_N(E - eV_b) f_N(E - eV_b) D_S(E)(1 - f_S(E)) \tag{2.2.2.1}$$

where $D_N(E)$ is the density of states of the normal metal, $D_S(E)$ is the superconductor density of states and is given by Equation 2.1.5.1, and T is the tunneling rate probability. Similarly, the tunneling rate from the superconductor to the normal metal $\Gamma_{S\to N}$ is

$$\Gamma_{S\to N}(V_b, T_N, T_S) = T D_S(E) f_S(E) D_N(E - eV_b)(1 - f_N(E - eV_b)) \tag{2.2.2.2}$$

The current associated with one tunneling event is the difference between the two tunneling rates multiplied by the electron charge e. To get the total current we then integrate over all energies. This gives a current of

$$\begin{aligned} I(V_b,T_N,T_S) &= e\int_{-\infty}^{\infty}(\Gamma_{N\to S}-\Gamma_{S\to N})\,dE \\ &= \frac{e}{e^2R_n}\int_{-\infty}^{\infty}[f_N(E-eV_b)-f_S(E)]\left(\frac{|E|}{\sqrt{E^2-\Delta^2}}\right)dE \end{aligned} \tag{2.2.2.3}$$

where we have taken the density of states of both the normal metal and the superconductor to be constants and equal the density of states around the Fermi Level ($D_N(E) \approx D_N(0), D_N(E) \approx D_N(0)$). This is a valid assumption because the density of states in metals varies slowly with energy, and for small temperatures, we can take it as a constant. We have also identified $TD_N(0)D_S(0) = 1/(e^2R_n)$, which comes from the requirement that Ohm's law, $V_b = IR_n$, is satisfied for large bias voltage where the gap is insignificant and the current is linear with bias voltage. R_n is the normal state resistance of the junction (see Figure 2.5). Figure 2.5 shown IV curves calculated using Equation 2.2.2.3 for different temperatures .

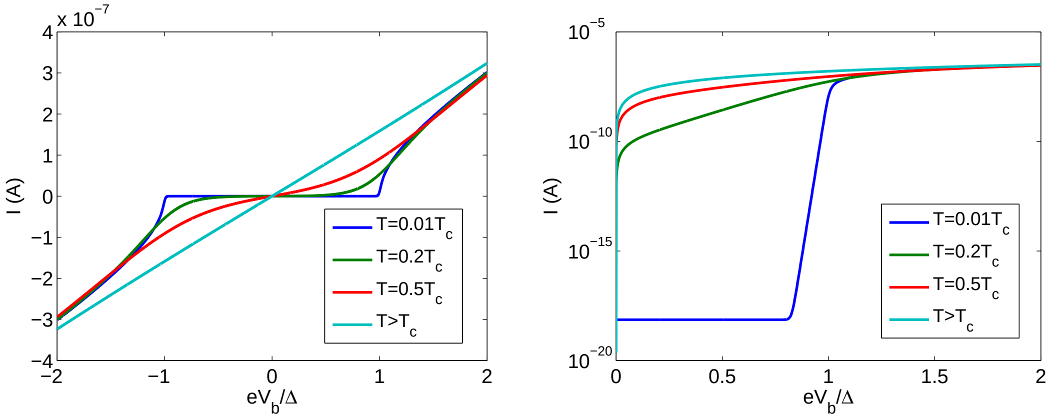

(a) **(b)**

Figure 2.5 – NIS IV curves for different temperatures on both linear and logarithmic scales. $\Delta = 174\mu$eV is used to generate these curves with no gap smearing. For $T > T_c$, we get a linear IV curve with slope of R_n. At much larger biases ($eV_b >> \Delta$), the energy gap is nearly invisible and we return back to the linear IV curve.

2.3 Superconductors at High Frequencies

At zero frequency (DC current), the resistance of the superconductor is zero, and the current does not dissipate power. However, at finite frequencies, the superconductor resistance is not zero and there is power dissipation. It is important to account for this power loss in device modeling to get the required performance. The easiest way to understand why a superconductor dissipates power at higher that zero frequencies is to consider the two-fluid model of the superconductors, which is briefly explained in the subsection to follow.

2.3.1 The Two-Fluid Model

The two-fluid model of superconductors is a pre-BCS simple model that models the free electrons in a superconductor as two fluids in parallel, “Normal” and ”Super” fluids. “Normal” electrons have a number density of n_n and they act exactly as normal electrons in metals. They are scattered by lattice impurities, and they carry a dissipative current. Under applied electric field E, those normal electrons acquire a mean drift velocity $\langle V_n \rangle = \frac{-e\tau}{m} E$ due to scattering, where e is the electron charge, τ is the scattering mean free time, and m is the electron mass. The resulting current density J_n is

$$J_n = -n_n e \langle V_n \rangle = \frac{n_n e^2 \tau}{m} E = \sigma_1 E \tag{2.3.1.1}$$

where σ is the conductivity. The conductivity is real, therefore, there is a resistance R associated with this fluid. The second fluid consists of “Super” electrons with number density n_s. They are not scattered by the impurities, and carry non-dissipative supercurrent. Since there is no scattering, those electrons are freely accelerated under an external electric filed E with velocity V_s. The equation of motion is

$$m \frac{dV_s}{dt} = -eE \tag{2.3.1.2}$$

assuming a sinusoidal electric field $E = E_0 e^{i\omega t}$ and solving we get

$$V_s = \frac{-eE}{i\omega m} \tag{2.3.1.3}$$

and the current density J_s is

$$J_s = -n_s e V_s = \frac{n_s e^2 \tau}{i m \omega} E = \sigma_2 E \tag{2.3.1.4}$$

The conductivity σ_2 is imaginary, therefore, there is an inductance L associated with this “Super” fluid, known as kinetic inductance.

Figure 2.6 depicts the two fluid model representation of a superconductor based on the aforementioned arguments.

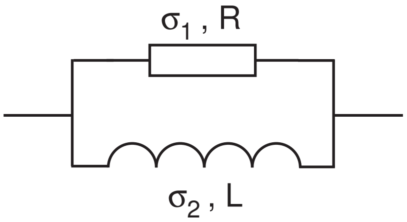

Figure 2.6 – The two-fluid model of a superconductor.

According to Equation 2.3.1.4, σ_2 is inversely proportional to the frequency. Therefore, at DC currents, the resistor R is shorted by the inductance L since it has zero impedance and all the current goes through the super fluid, dissipating no power. On the other hand, at higher frequencies, the impedance of the super fluid begins to increase and part of the current goes through the resistor, dissipating some power.

2.3.2 The Concept of Surface Impedance

For a conductor of finite conductivity σ in an electromagnetic fields, solving Maxwell's equations tells us that the intensity of the field inside the conductor decrease exponentially with the distance from the metal surface. The current flows through a thin sheet on the surface, and at a distance δ known as the skip depth, the intensity of the field decays to 1/e of its value at the surface. The skin depth is given by

$$\delta = \sqrt{\frac{2}{\omega\mu\sigma}} \tag{2.3.2.1}$$

where ω is the angular frequency of the current, and μ is the magnetic permeability of the conductor.

Therefore, for an ideal conductor of infinite conductivity, the electric field is completely excluded from the interior of the conductor.

On the other hand, the electromagnetic boundary conditions applied to the interface between two media (see for example [50]) tells us that the tangential component of the electric field in the two media should be equal at the interface. Hence, the tangential component of the electric field on the surface of an ideal conductor is always zero since the electric field inside a perfect conductor is zero. Whereas the tangential component of the electric field on the surface of a non-ideal conductor of finite conductivity is not zero since some field exists inside it. It follows that the simulation of real conductors would be a time consuming process since it requires solving Maxwell's equations inside the conductor.

The concept of surface impedance helps to avoid the complexity of solving Maxwell's equations inside the conductors. The surface impedance Z_s is defined as the ratio between the tangential components of the electric field E and the tangential component of the magnetic field H on the surface of the conductor

$$Z_s = \frac{E_t}{H_t} \tag{2.3.2.2}$$

The surface impedance therefore acts as a boundary condition for fields on the surface of the metal. By using surface impedance, the dissipation and energy stored in the superconductor are accounted for in the simulation.

The two-fluid model could be used as a first-order approximation for the surface impedance because it is simple and intuitive. However, it does not consider the energy gap, does not account for the temperature dependence of the penetration depth correctly. Hence, it is inaccurate. In Chapter 4, it will be presented how to get this surface impedance using the more accurate BCS Theory, while in Chapter 5, this surface impedance will be used in simulations.

One may argues that this model might not be useful because for devices carrying AC current, the electromagnetic wave is not normally incident on the superconductor, instead it travels along it. However, Matick [36] showed that the analysis of wave propagation parallel to the conductor yields the same surface impedance as the normal incident wave.

Chapter 3

Cold-Electron Bolometer

3.1 Bolometers

3.1.1 What Is a Bolometer

Bolometers are direct detectors of infrared and millimeter waves. They are known to be the most sensitive and broadband detectors in this range of electromagnetic spectrum. They are widely used in space-based astrophysical observations, since the early universe radiates strongly in this region of spectrum. To illustrate how a bolometer operate, consider the simple thermal model in Figure 3.1. A bolometer consists of a radiation absorptive element of heat capacity C, like a thin layer of metal, connected to a body of constant temperature (thermal reservoir) through a thermal link of a small thermal conductance G.

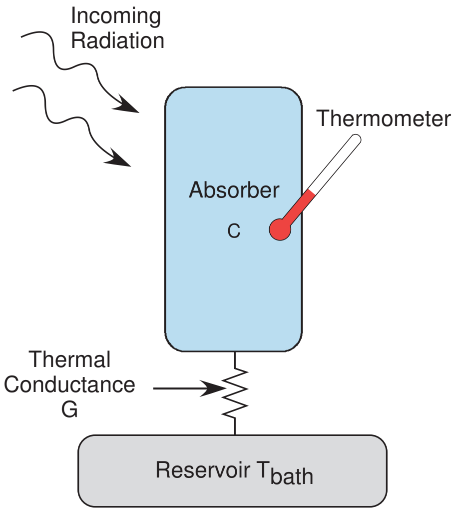

Figure 3.1 – A simple thermal model of a bolometer.

The absorber absorbs the photons of the impinging radiation and converts their energy to heat, leading to raising the temperature of the absorber above that of the reservoir. The absorber temperature change is proportional to the absorbed power; therefore measuring this temperature difference one can find the incident power. The temperature change can be measured by the attached thermometer. The thermometer is a device that has a temperature-dependent property that can be measured. Examples of those properties are the resistance of a simple resistor, the resistance of a superconductor near its critical temperature, and the tunneling current in a tunnel junction.

For the highest possible sensitivity, such detectors need to be cooled to cryogenic temperatures (below 1 K). Thermal noise decreases with decreasing the operating temperature of the bolometer. To be able to achieve the desired scientific goals, arrays of 10^3–10^5 pixels are required.

3.1.2 Bolometer Technologies

The most sensitive detectors for cosmic applications in far-infrared are the cryogenic bolometers operating typically at a temperature of about 100 mK. The noise properties of those devices are considerably improved by decreasing the operating temperature. In this section, different types of cryogenic bolometers are briefly explained.

Semiconductor Bolometers

Semiconductor bolometers constitute the classical bolometer technology. They have been around for 20 years. They exploit the fact that the resistance of a semiconductor has an exponential dependence on temperature.

The disadvantages of this technology include a small amplifier noise margin and a very difficult interface between the bolometers at 1000mK and the amplifiers at 100K [51]. They are rather difficult to fabricate and at low temperature they possess a very large time constant because of low temperature coefficient.

Kinetic Inductance Detector (KID)

This device is based on the modification of the inductance of a superconductor (called kinetic inductance) when it absorbs photons [38]. KID is very sensitive when cooled down to 100 mK, however, it is strongly influenced also by stray cosmic rays.

Hot-Electron Bolometers (HEB)

At low temperatures (less than 1K), the coupling between electrons and phonons is weak. This means that electrons are thermally isolated from phonons and can have a temperature different from that of the surrounding phonons bath. This thermal decoupling results in large temperature rise of the electrons for a small absorbed power (increased sensitivity). Those heated electrons are known as “hot electrons” [41]. Therefore for HEB, the electronic heat capacity is the relevant heat capacity, while the electron-phonon thermal conductance is the relevant thermal conductance.

Transition Edge Sensor (TES)

Transition Edge Sensor (TES) [32] exploits the fact that for a superconductor near its T_c, the change of the resistance is very sharp. TES bolometers have enhanced linearity, speed, and stability due to strong negative electrothermal feedback. The amplifiers are also superconducting, which mean they dissipate very small amount of power and produce very little noise. Its fabrication is simple, just thin-film deposition and optical lithography. One drawback of TES bolometers is that they operate at the temperature of the superconductor-normal transition. This fixed operation temperature makes the bolometers less flexible since it restricts the dynamic range.

Cold-Electron Bolometers

Like HEB bolometers, Cold-Electron Bolometer (CEB) [27, 28] make use of the weak electron-phonon at low temperatures, but they have no restrictions on the operating temperature. CEB also has the additional advantage of electron cooling thanks to NIS tunnel junction. This cooling feature results in high sensitivity, decreased noise, and high dynamic range. The Cold-Electron Bolometer is the topic of the next section.

3.2 CEB Device Structure and Principles of Operation

The Resonant CEB device considered in this work [29] is shown in Figure 3.2. It consists of two small normal metal strips acting as an absorber and forming the normal electrodes of two NIS tunnel junctions. The superconducting electrodes of the NIS junctions could be connected to the antenna or could acts themselves as an antenna. The antenna is needed to couple the radiation to the bolometer since the device is much smaller than the operating wavelength.

The NIS junctions (see section 2.2) capacitively couple the RF power from the antenna to the absorber. Upon absorping this power, the electrons system of the absorber gets hotter.

When the NIS junction is biased just below the gap voltage of the superconductor, the hottest and most energetic electrons at the tail of the Fermi distribution in the absorber rapidly tunnel through the NIS junctions, giving an increase in the bias voltage if the junctions are current biased, or an increase in the bias current if the junctions are voltage

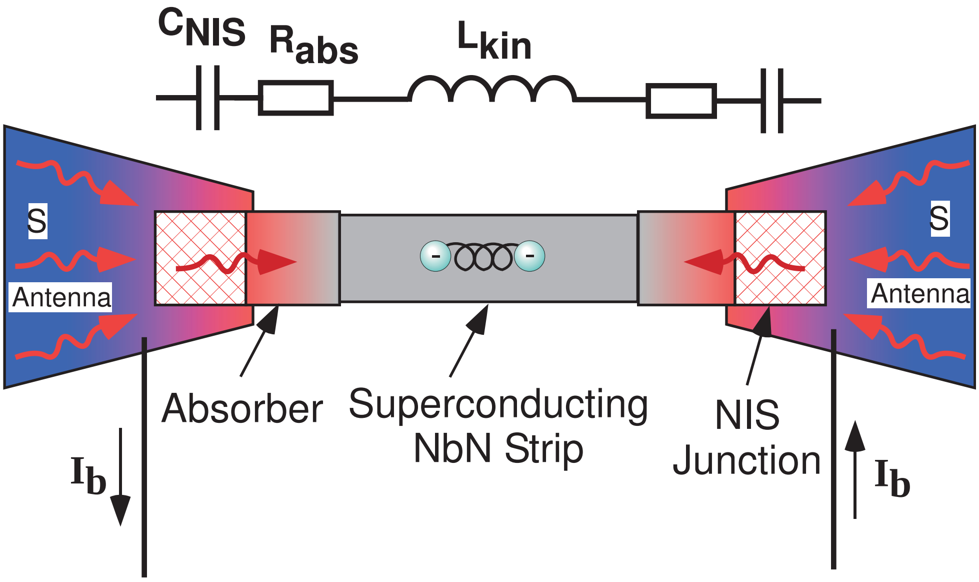

Figure 3.2 – Schematic of the Resonant Cold-Electron Bolometer. The NIS junctions capcitively couples the absorber to the antenna. The NbN strip is a part of the absorber. The resistance of the absorber, the capacitance of the NIS junction, and the kinetic inductance of the NbN strip forms an RLC filter to select the frequency band of operation.

biased. Thus, the increase in temperature is detected by the NIS junction. Due to the tunneling of those electrons, the absorber gets cooled. The role of the NIS junction is four-fold. It is used for capacitive RF coupling to the antenna, for thermal isolation of the absorber, for electron cooling, and as a thermometer as it experiences a current change if it is voltage biased, or voltage change if it is current biased.

As will be shown in subsection 4.1.1, The NIS cooling power equation is similar for positive and negative bias voltages. It follows that the heat flows out of the normal metal regardless of the sign of the bias voltage. This feature can be exploited by connecting two NIS junctions in series such that the normal metal is shared. This combined junction is known as SINIS junction. It was demonstrated experimentally [34] that SINIS structure is an efficient electron cooler. In SINIS junction, the current flows into the structure through one NIS junction, and out through the other one, whereas the heat is removed out of the normal metal absorber through both junctions. Therefore, refrigerator performance is doubled. On top of that, when compared to single asymmetric NIS junction, SINIS structure provides more efficient thermal isolation of the central metal absorber and is easier to fabricate.

The energy level diagram of the device is shown in Figure 3.3 at a voltage bias nearly equal double the tunneling threshold,$V \approx 2 \times \Delta/e$.

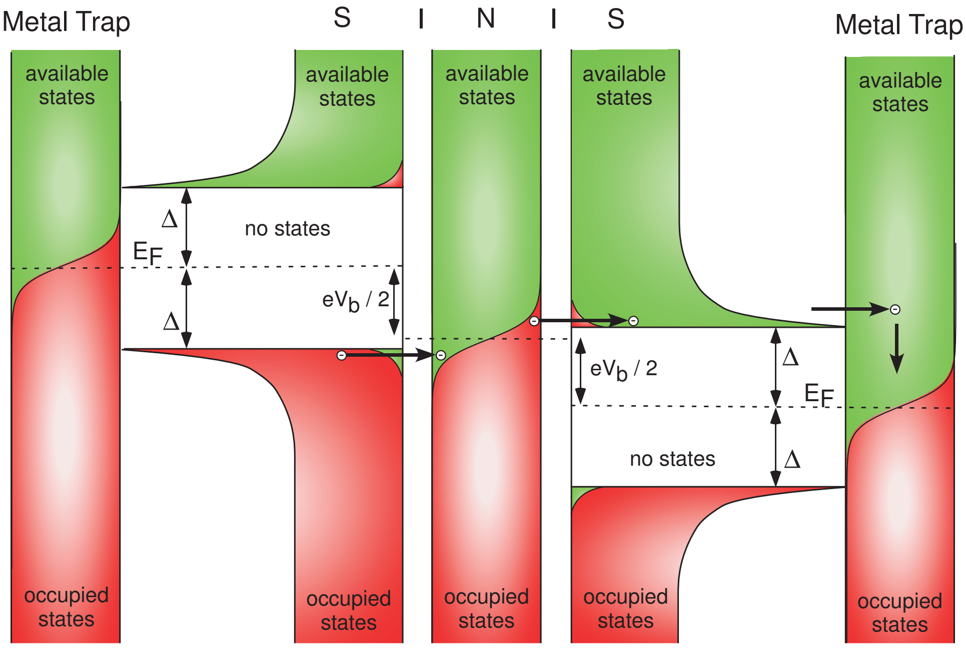

Figure 3.3 – Energy level diagram of the CEB at a voltage bias nearly equal double the tunneling threshold,$V \approx 2 \times \Delta/e$.

Shown also in Figure 3.3 is the metal traps. The power removed from the normal metal is deposited into the superconductor electrode in form of quasiparticles. This power heats up the superconductor and as a result the performance of the refrigerator is degraded. To cool down the superconductor, quasiparticles traps are used. Those quaiparticles traps acst as heatsink for the superconductor electrodes. They are basically normal metals such that quasiparticles in the superconductor can thermalize easily in those normal metal traps. The idea of quasiparticles traps for NIS junctions was introduced by Fisher et al. [14].

3.2.1 Filtering Capability

The impedance of the CEB device shown in Figure 3.2 has three components; the resistance of the absorber R_{abs}, the capacitance of the two NIS tunnel junctions C_{NIS}, and the kinetic inductance of the NbN nanostrip L_{kin}. Those three components form together an integrated band-defining nano-filter, which obviates the need for the much larger external filters usually used in radio astronomy applications. Because of this resonant feature, the device is called Resonant Cold Electron Bolometer (RCEB) [29].

3.2.2 Advantages of CEB

In this subsection we summarize the advantages of CEB. The CEB has several advantages compared to current cryogenic detectors like TES:

- The effective electron cooling by the tunneling current makes the operating temperature and noise lower.
- High dynamic range. This is true because the absorbed power is removed from the absorber, delaying its saturation.
- Easy to fabricate in arrays on planar substrate.
- Temperature stability of a cryostat is not so important since it works at temperatures far below T_c.
- Sensitivity to cosmic rays is considerably less.
- Small footprints due to the embedded filtering feature.

3.3 Figures of Merit

Figures of merit are those parameters based on which one can characterize and judge the performane of a bolometer.

3.3.1 Responsivity

The thermal isolation of the bolometer's absorber ultimately limits the sensitivity of the device. If the absorber is well isolated from the environment, a small amount of incident power will cause dramatic increase to its temperature. The volume of the absorber also plays an important role. A small absorber volume means that it heats up with the smallest amount of power. The responsivity of the CEB is very high due to the fact that the absorber is isolated by weak electron-phonon coupling and by the NIS junctions, and its small volume.

Responsivity is defined as the change in the output (voltage or current) signal per watt of absorbed power of the detected signal. In voltage biased mode, it is given by $S_{V-bias}(V) = \partial I/\partial P$, and in current biased mode is given by $S_{I-bias}(I) = \partial V/\partial P$. Explicit expressions for CEB responsivity in both voltage and current biased mode are given in next chapter.

3.3.2 Noise and Noise Equivalent Power (NEP)

Noise properties are characterized by the so-called Noise Equivalent Power (NEP). NEP is defined as the input power to a detector that will produce an output signal having the same power as the intrinsic noise of the device in one hertz output bandwidth [52]. The units of NEP is $\mathrm{W}/\sqrt{\mathrm{Hz}}$.

Two kinds of noise are prevalent in bolometer. The first one is the so-called shot noise which arises from the inherent discrete nature of both electrons and photons. The second kind is the thermal noise, associated with the quantization of energy transfer between different subsystems in the bolometer The noise of the bolometer is the sum of the following four contributions:

- The photon noise. It is a shot noise and arises from the intrinsic discrete nature of photons which causes fluctuation of the incident photon flux.
- Noise in the absorber. It is a thermal fluctuation noise and associated with the quantization of energy transferred between electrons and phonons.
- Noise in the NIS junction due to the discrete nature of the electrons that tunnel "shot noise". NIS junction has also a thermal noise component that we will speak about later.
- Noise in the amplifiers that amplify the detected signal.

In the next chapter, each of these terms will be evaluated. The brightness of the cosmic microwave background sets a photon noise level of $1 \times 10^{-17} W/\sqrt{\mathrm{Hz}}$ at the detector. Since current bolometers technology allows us to have a NEP level lower than that, we have a photon-noise limited detector, which means that the detector is limited by the photon noise of the CMB itself.

3.3.3 Time Constant

The time constant τ is a measure of how fast the bolometer respond to the incoming radiation. Referring to the thermal model in Figure 3.1, τ can be written as $\tau = C/G$ [52]. Low time constant allows the scanning telescope to have high scan speed "high RPM".

This page intentionally contains only this sentence.

Chapter 4

Modeling

In this chapter, the modeling of the Cold-Electron Bolometer is presented. The purpose of the device modeling is to extract out the device's important parameters like cooling power, sensitivity, responsivity, and noise characteristics. The methodology is to try to fit a mathematical model to the experimentally measured IV curves of the device. This is done by solving the so-called heat balance equations.

In this chapter also, the modeling of the superconducting niobium microstrip lines at low temperatures and high frequencies will be presented. This is done by solving Mattis-Bardeen Theory in the local limit to get the frequency-dependent surface impedance, which is crucial for designing and simulating the superconducting antenna that is coupled to the bolometer. The design and simulation of the antenna itself is treated in the next chapter. Modelling of both the bolometer and the superconducting niobium was carried out using MATLAB (See Appendix B).

4.1 Power Flow in CEB

This section introduces the different terms that contribute to the power flow in the device. Then those terms along with the experimentally measured IV curves of the device will be put together in one equation, the heat balance equation, whose solution gives the device parameters.

4.1.1 NIS Cooling Power

The power taken out of the normal metal due to tunneling can be evaluated by replacing a factor of e with a factor $E - eV_b$ in the NIS tunneling current equation Equation 2.2.2.3, which is the energy removed from the normal metal associated with a single tunneling event. This removed power results in cooling of the electrons system and is the basis of NIS cooling; hence it is called the cooling power. It is given by

$$P_{cool} = \frac{1}{e^2 R_n} \int_{-\infty}^{\infty} (E - eV_b)[f_N(E - eV_b) - f_S(E)] \frac{|E|}{\sqrt{E^2 - \Delta^2}} dE \qquad (4.1.1.1)$$

Figure 4.1 shows P_{cool} calculated numerically for Al for different absorber electrons and superconductor temperatures.

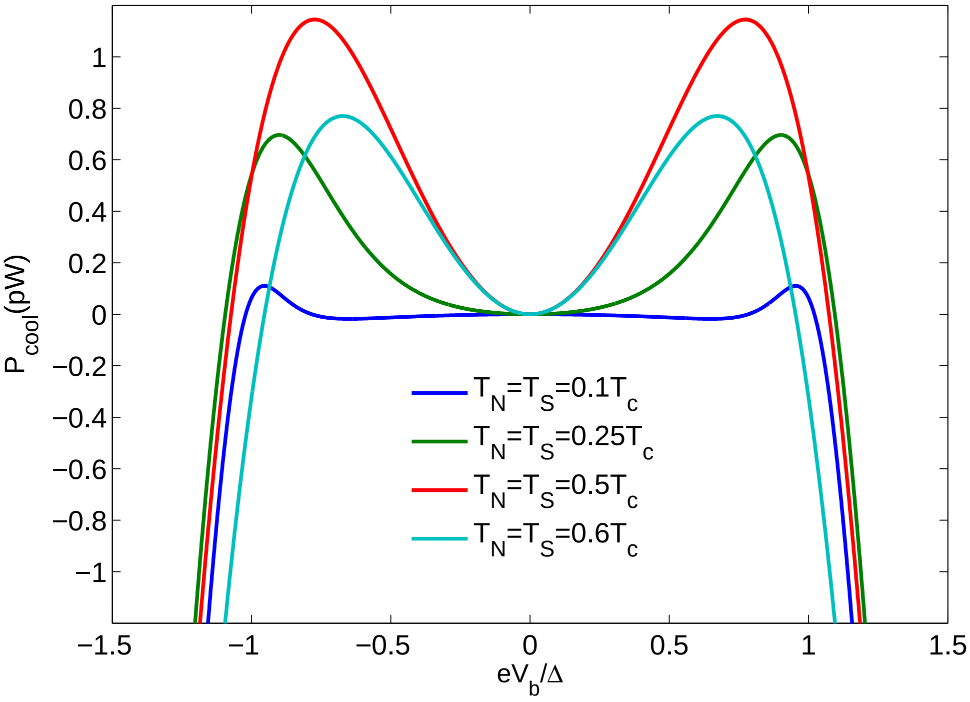

Figure 4.1 – NIS cooling power P_{Cool} vs normalized biasing voltage for different temperatures for $T_N = T_S$.

For biases near $eV_b \approx \pm\Delta$, the cooling power is maximum, meaning that efficient cooling of the absorber electron system is being achieved.

The fact that P_{cool} is even in V_b allows connecting two NIS junctions in series to double the cooling power. The two junctions have to be biased such that they have opposite sign on their voltage biases [42]. This structure is known as SINIS junction.

4.1.2 Electron-Phonon Coupling

At low temperatures (less than 1K), the coupling between electrons and phonons is weak. This is true because at low temperatures, the electron-phonon collision rate is low, and the relaxation gets very slow. Phonons in the metal are well-coupled to phonons in the substrate and typically act as a thermal reservoir. This means that electrons are thermally isolated from phonons and can have a temperature different from that of the surrounding phonons bath. In CEB, this thermal decoupling result in large temperature rise of the electrons system for a small absorbed power. This also makes significant cooling of the electrons system below the lattice temperature possible.

The heat flow from the electrons to the phonons subsystem in the normal metal is given by [43, 53, 57, 58]

$$P_{e-p} = \Sigma\Omega(T_n^5 - T_p^5) \tag{4.1.2.1}$$

where Σ is a material constant that depends on electron-phonon coupling strength, Ω the volume of the absorber, T_n is the electron temperature in the normal metal, and T_p is the phonons temperature in the substrate. $\Sigma \approx 1nW/K^5/\mu m^3$ for most metals.

As a result of lattice mismatch between the absorber and the substrate, the phonons will be scattered at the interface resulting in thermal resistance, known as Kapitza acoustic mismatch. Therefore, phonon systems in the absorber and in the substrate are two separate systems and can have different temperatures. However, at the low temperatures, the wavelength of the thermal phonons is much larger than the thickness of a typical thin film of the absorber. Hence the interface should be quite transparent to these phonons and those two subsystems are considered as one system. The Kapitza resistance will be neglected throughout [42].

4.1.3 Power Dissipated in the Superconductor

Power is deposited in the superconductor in the form of quasiparticle excitations. Both the power removed from the normal-metal absorber P_{cool} and the IV power are deposited in the superconductor. Hence the power deposited in the superconductor, P_S, can be calculated from the relation

$$P_S = P_{cool} + IV_b \tag{4.1.3.1}$$

Using Equation 2.2.2.3 and Equation 4.1.1.1, we arrive to the following expression for P_S

$$P_S = \frac{1}{e^2 R_n} \int_{-\infty}^{\infty} E[f_N(E - eV_b) - f_S(E)] \frac{|E|}{\sqrt{E^2 - \Delta^2}} dE \tag{4.1.3.2}$$

Figure 4.2 shows P_S calculated for Al for different absorber electrons temperatures and superconductor temperatures.

Heating of the superconductor will decrease the cooling power. Heating of the superconductor can be reduced by using quasiparticles traps, which are normal metals.

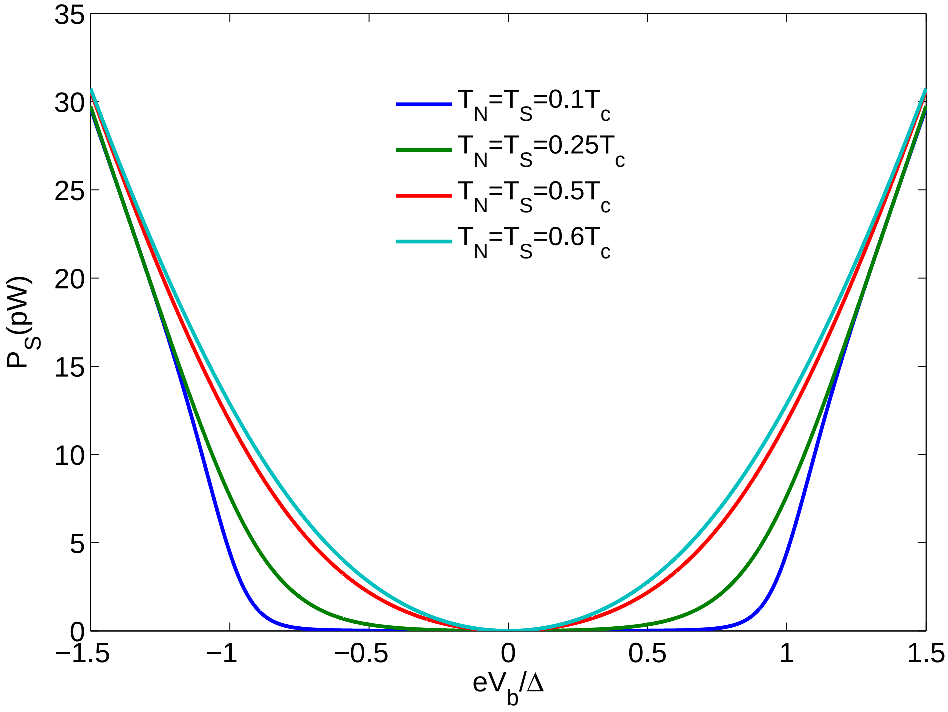

Figure 4.2 – NIS P_S vs normalized biasing voltage for different temperatures for $T_N = T_S$.

4.1.4 Power Back-flow

Electrons that tunneled into the superconductor can recombine into Cooper pairs to produce phonons that will heat the normal metal. This can be modeled as a small fraction β of the power deposited in the superconductor P_S being returned back to the absorber [14, 55, 56]. This degrades the cooling capability of the NIS junction. In the thermal model presented in this chapter, β is one of the parameters to fit.

4.1.5 Subgap Leakage

The DOS does not actually diverge but is smeared out due to the finite lifetime of the thermal electrons. The current-voltage (IV) relationship of actual tunnel junctions deviates from BCS theory, showing an extra leakage current when the bias voltage is below the gap (subgap conductance). This can be modeled by adding the so-called Dynes Parameter Γ to the density of states [11]. The Dynes Parameter smears the gap by creating finite states within the gap and decreasing the singularity at the gap-edge. The modified normalized density of states with this parameter is

$$n_s(E) = \left| \Re\left(\frac{E - i\Gamma}{\sqrt{(E - i\Gamma)^2 - \Delta^2}} \right) \right|$$

Figure 4.3 shows the modified BCS density of states with Dynes smearing.

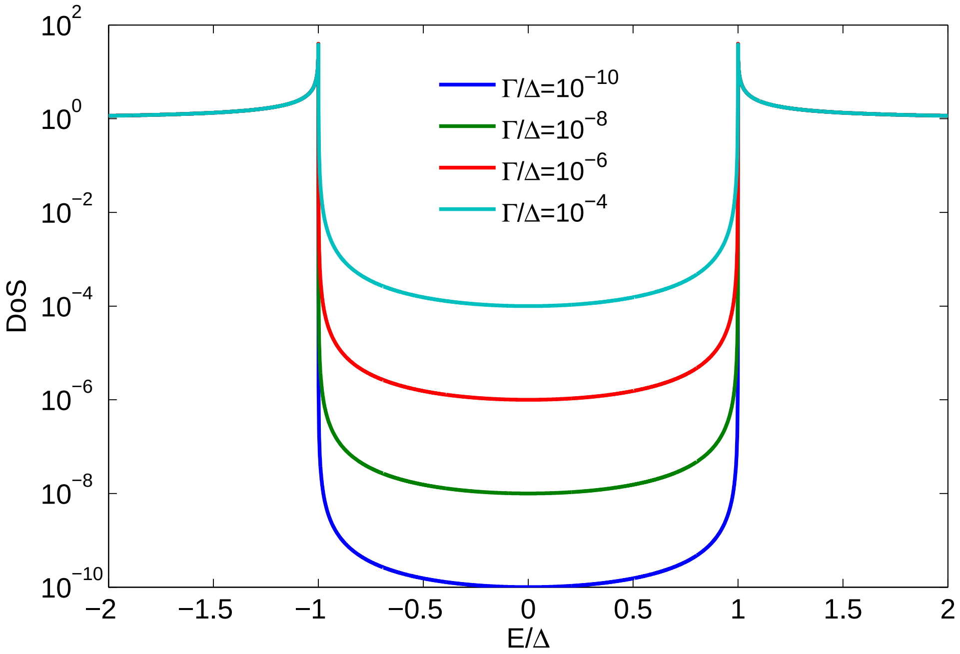

Figure 4.3 – Modified BCS density of states.

4.1.6 Joule Heating

The current passing through the normal metal absorber causes resistive heating and the associated dissipated power in the absorber P_{joule} is simply given by Ohm's law $P_{joule} = I^2 R_{abs}$, where R_{abs} is the resistance of the absorber.

4.1.7 Bringing It All Together: Heat Balance Equations

The equation that summarizes all the pervious power terms together is what is called the heat balance equation. However, we have two systems: the normal electrode "the absorber" and the superconducting electrode. Therefore, we have two heat balance equations. Two complications arise, firstly those equations are transcendental equations so they have to be solved numerically, and secondly they are coupled equations so they have to be solved simultaneously. The next subsections deals with those two equations and their solution.

Heat Balance Equation in Normal Electrode

The incident power P_0 to be measured heats the absorber along with other terms, while NIS tunneling and electron-phonon coupling cools the absorber. The heat balance equation for the normal metal absorber is

$$2P_{cool}(V_b, T_n, T_s) + P_{e-p,n}(T_n, T_p) = P_{joule}(V_b, T_n, T_s) + 2\beta P_S(V_b, T_n, T_s) + P_0 \tag{4.1.7.1}$$

The right-hand side describes the terms that causes heating, while the left-hand side describes the terms of cooling. Most of the terms are functions of the bias voltage V_b, the normal electrode temperature T_n, the quasiparticles temperature in the superconducting electrode T_s.

Given V_b , T_p, and T_s one can solve for T_n, however, T_s itself is variable because the superconductor is often heated. T_n is related to T_n through another heat balance equation, which is the topic of the next subsection.

Heat Balance Equation in Superconductor

The heat balance equation in the superconductor is

$$P_{e-p,s}(T_s, T_p) = (1 - \beta)P_S(V_b, T_n, T_s) \tag{4.1.7.2}$$

It simply says that part of the power that enters the superconductor, $(1 - \beta)P_S$, gets transferred to the phonon system of the superconductor through electron-phonon coupling. The factor of two signifies the fact that we have two NIS junctions.

4.2 Parameters Fitting

The two aforementioned heat balance equations are both functions of the electron temperature in the normal metal T_n and the quasiparticles temperature in the superconductor T_s. Solving these two equations simultaneously for many values of V_b tells us how the junction performs at different bias voltages. One therefore can choose the value of V_b that minimized T_n and hence maximizes cooling. The layout of the measured device is shown in Figure 4.4. It consists of twelve bolometers connected in series. The measurement setup is described in Appendix A.

In order to accurately fit the measured data, we require knowledge of all material parameters of the Aluminum used to fabricate the superconducting electrodes (transition temperature, gap ratio). Such measurements are not currently available. The transition temperature is different for thin film Al than the bulk Al. For a film of thickness of $70\mu m$ is 1.62 K [8] vs 1.2 for bulk. The gap ratio $2\Delta/K_BT_c$ is 3.37 according to [39] and 3.25 according to[5]. We use an average value between those two values. The

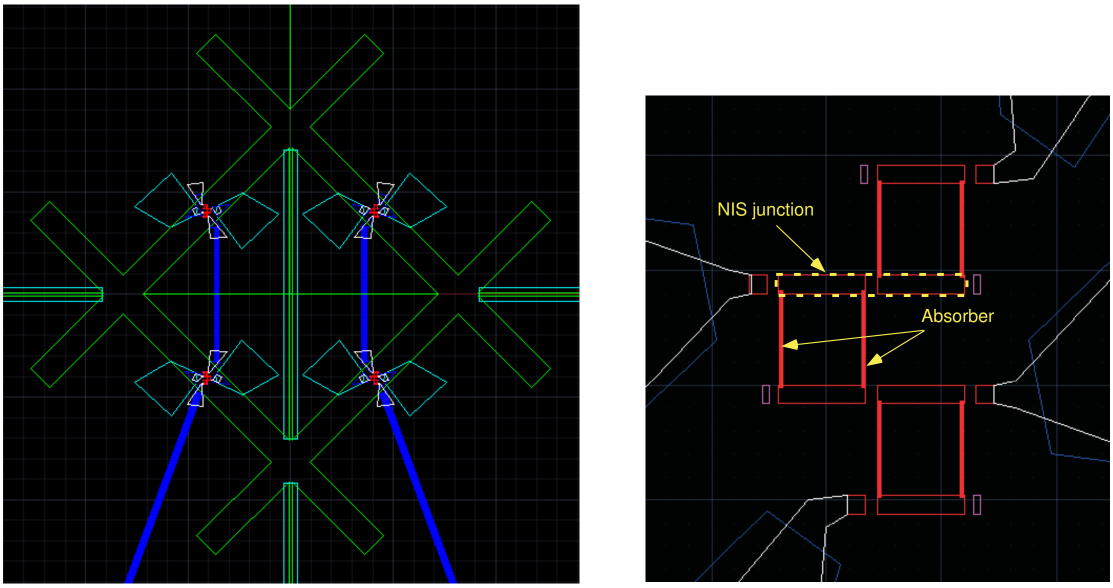

(a) **(b)**

Figure 4.4 – AutoCAD layout of the measured device. (a) Twelve bolometers are connected in series. Every arm of the cross-slot antenna contains three bolometers. (b) Zoom in to one arm of the cross slot showing three bolometers. The absorber consists of two metal strips in parallel to lower the resistance.

electron-phonon coupling strength parameter Σ in the normal metal is $1.1nW/\mu m^3K^5$ [34, 40].

To solve those two equations, I assume initially that $T_s = 0.3K$ then solve the first heat balance equation for T_n, then use this value of T_n to solve the second heat balance equation for T_s. This process is repeated four times to reach a self-consistent solution. I use the MATLAB function **fzero** to slove the equations numerically. See Appendix B.1 for the corresponding MATLAB code. After solving for T_n and T_s for a range of V_b, one can use those values to theoretically construct the IV curve of the junction using Equation 2.2.2.3. Those curves can then be compared to the experimentally measured IV curves of a given junction.

The purpose of comparing the theoretically calculated IV curves to the experimentally measured ones is to deduce the parameters that cannot be measured experimentally. Those parameters are

- Γ, the Dynes smearing parameter, see subsection 4.1.5.
- β, the fraction of the power returned to the absorber, see subsection 4.1.4.
- Ω_S, the volume of the superconductor [1].

---

[1] Metal quasiparticles trap changes the effective volume of the superconductor electrode.

- P_0, the incident power [2].

The strategy is to vary those parameters till the best fit is obtained. To make this process less time consuming, less error prone, and more efficient, one has to be able to make educated guesses while changing the parameters. Therefore, understanding the effect of each parameter individually on the IV curve is crucial.

Figure 4.5 shows the effect of each of the four parameters on the IV curve, while the other three parameters are held constant.

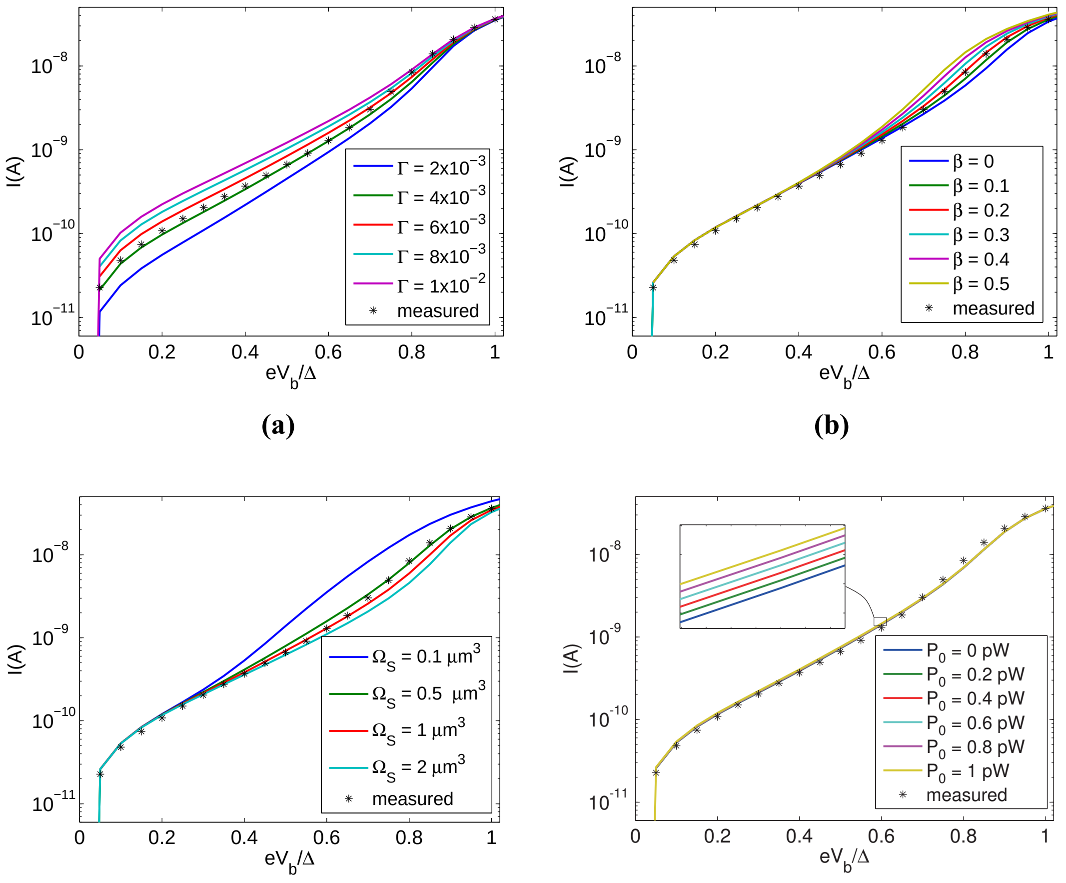

(a) **(b)**

(c) **(d)**

Figure 4.5 – Investigating the effect of different fitting parameters on IV curve. (a) Effect of varying γ. (b) Effect of varying β. (c) Effect of varying the volume of the superconductor. (d) Effect of varying the incident power.

After choosing the initial set of fitting parameters. I vary those parameters slightly around their initial values to obtain more fine-tuned fit. See Appendix A.2 for the corresponding MATLAB code. Table Table 4.1 shows the final values of the fitting parameters.

---

[2] In our measurement setup, the source of the power is a black body with known temperature and power, however, the power that the bolometer absorbs is unknown due to reflections.

Table 4.1 – Fitted parameters values.

Parameter	**Value**
Γ	6×10^{-3}
β	0.15
$Vol_{SC}(\mu m^3)$	2
$P_{bg}(pW)$	0.2

Figure 4.6 shows the electron temperature T_n as a function of bias voltage. One finds that T_n is significantly lower than the substrate phonon temperature T_p, which is the effect of NIS electron cooling. The cooling is maximized near $V_b \approx \Delta/e$.

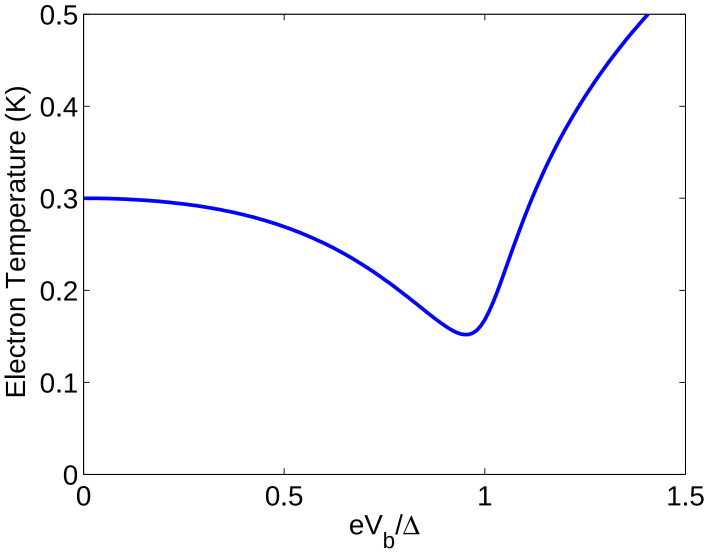

Figure 4.6 – Temperature of electrons in the normal metal as a finction of bias voltage. The temperature is lower than the phonon temperature ($T_p = 0.3K$), indicating cooling of electrons. Cooling is maximum near $V_b \approx \Delta/e$.

Figure 4.7 shows the result of the fitted IV curve.

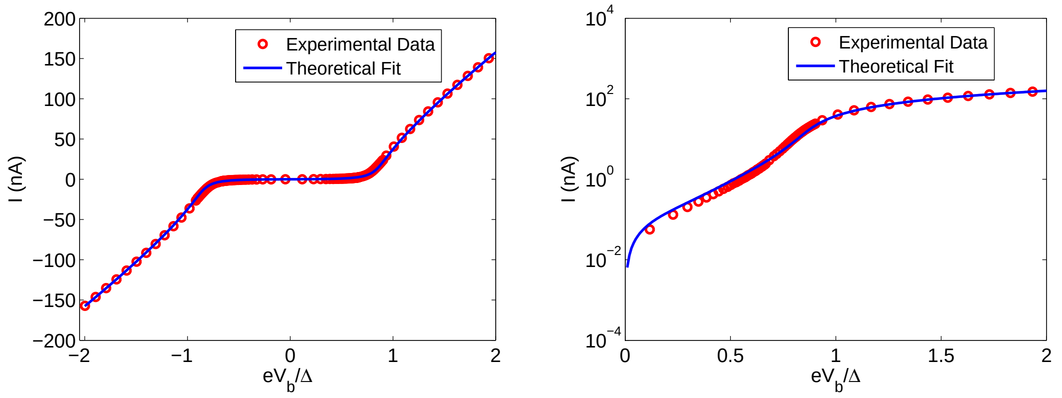

(a) **(b)**

Figure 4.7 – Fitted IV curve on both linear and logarithmic scales.

4.3 Responsivity

Low frequency responsivity in both voltage-biased mode S_{V-bias} and in current-biased mode S_{I-bias} at low frequencies are given by the following two expressions respectively

$$S_{V-bias}(V) = \frac{\partial I}{\partial P} = \frac{\frac{\partial I}{\partial T}}{5\Sigma\Omega T_e^4 + \frac{\partial P}{\partial T}} \tag{4.3.0.3}$$

$$S_{I-bias}(I) = \frac{\partial V}{\partial P} = \frac{-\frac{\partial I/\partial T}{\partial I/\partial V}}{5\Sigma\Omega T_e^4 + \frac{\partial P}{\partial T} - \frac{\partial I/\partial T}{\partial I/\partial V}\frac{\partial P}{\partial V}} \tag{4.3.0.4}$$

Figure 4.8 shows how the responsivity changes with changing the resistance of the absorber for both voltage biased and current biased modes of operation.

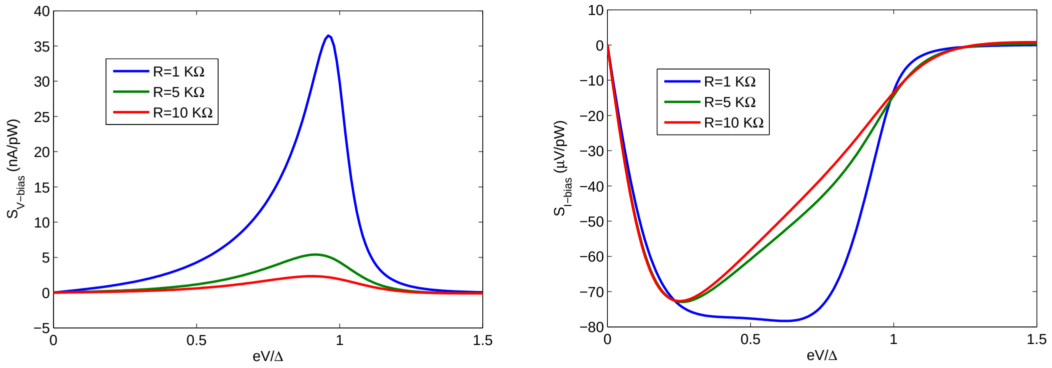

(a) **(b)**

Figure 4.8 – Responsivity for different absorber resistance values. (a) In voltage biased mode. (b) In current biased mode.

Having solved for temperatures T_n and T_s, we can evaluate the responsivity. Heat is relaxed through two mechanisms, through electron-phonon interaction, and through electron tunneling in the NIS junction. Therefore, in the expression for the voltage biased responsivity, the sum of the two heat conductances $G_{e-ph} = 5\Sigma\Omega T_e^4$ and $G_{NIS} = \frac{\partial P}{\partial T}$ appears in the denominator.

To make the evaluation of the responsivities easier, analytical expressions for the differentials was obtained first using differentiation under integration principle. Appendix B.3 shows the responsivities functions.

4.4 Noise Model

As was mentioned in subsection 3.3.2, the noise characteristics of the bolometer consists of four contributions. This section is devoted to the evaluation of these terms. Here we follow the noise model presented in [16]. The corresponding MATLAB code is in Appendix B.3.

4.4.1 Photon Noise

As was mentioned in the Introduction, CMB spectrum follows a perfect black body distribution at a temperature of 2.725K. Therefore the spectral density of radiation can be obtained from Planck's distribution and then can be used to calculate the noise in radiation received by the bolometer. An approximate result for the NEP due to photon fluctuation is [7]

$$NEP_{photon}^2 = 2K_BT_b(hf_0 + K_BT_b)BW \tag{4.4.1.1}$$

where T_b is the black body temperature and equals 2.725K for CMB, f_0 is the center frequency of the received band, and BW is the bandwidth of operation. As will be shown in the next chapter, the bolometer considered in this work operates at a frequency of nearly 100 GHz and a bandwidth of 15 GHz. Plugging the numbers gives $NEP_{photon} = 1 \times 10^{-17} W/\sqrt{\text{Hz}}$.

4.4.2 Noise in the Absorber

This contribution to noise is due to the quantization of the heat flow between electrons and phonons, and also known as thermal fluctuation noise or phonon noise.

Phonon noise in systems where electrons have different temperature than phonons was studied in [17]. A simplified version was presented in [16] and the results is

$$NEP^2_{e-p} = 10K_B\Sigma\Omega(T_e^6 + T_p^6) \tag{4.4.2.1}$$

where T_e and T_p are the temperature of the electrons and phonons respectively.

4.4.3 NIS Junction Noise

Part of this noise is associated with electrons that tunnel through the junction. Also every electron that tunnel carries energy, which introduces a thermal noise. These two noises are correlated. For voltage-biased mode, the NIS junction noise is given by

$$NEP^2_{NIS_{V-bias}} = \frac{\langle \delta I^2 \rangle}{S_I^2(V)} + \langle \delta P^2 \rangle - 2\frac{\langle \delta P \delta I \rangle}{S_I(V)} \tag{4.4.3.1}$$

and in current-biased mode by

$$NEP^2_{NIS_{I-bias}} = \frac{\langle \delta I^2 \rangle}{S_V^2(I)} \left(\frac{\partial V}{\partial I}\right)^2 + \langle \delta P^2 \rangle - 2\frac{\langle \delta P \delta I \rangle}{S_V(I)} \left(\frac{\partial V}{\partial I}\right) \tag{4.4.3.2}$$

where $\langle \delta I^2 \rangle$ is the spectral density of the shot noise due to current fluctuations, $\langle \delta P^2 \rangle$ is the spectral density of heat flow noise, and $\langle \delta P^2 \delta I^2 \rangle$ is the spectral density of the correlator of those two noises.

4.4.4 Amplifier Noise

The noise due to the readout amplifier in voltage biased mode is given by

$$NEP^2_{amp} = \frac{\langle \delta I^2 \rangle_{amp}}{S^2_{V-bias}(V)} \tag{4.4.4.1}$$

where $\langle \delta I^2 \rangle_{amp}$ is the current sensitivity of the current amplifier, and in current biased mode is given by

$$NEP^2_{amp} = \frac{\langle \delta V^2 \rangle_{amp}}{S^2_{I-bias}(V)} \tag{4.4.4.2}$$

where $\langle \delta V^2 \rangle_{amp}$ is the voltage sensitivity of the voltage amplifier.

4.4.5 Total Noise

The total noise is now given by

$$NEP_{total} = NEP^2_{e-p} + NEP^2_{NIS} + NEP^2_{amp} \tag{4.4.5.1}$$

Figure 4.9 shows the components of the NEP for both voltage biased and current biased modes for absorber resistance of $R_{abs} = 1K\Omega$.

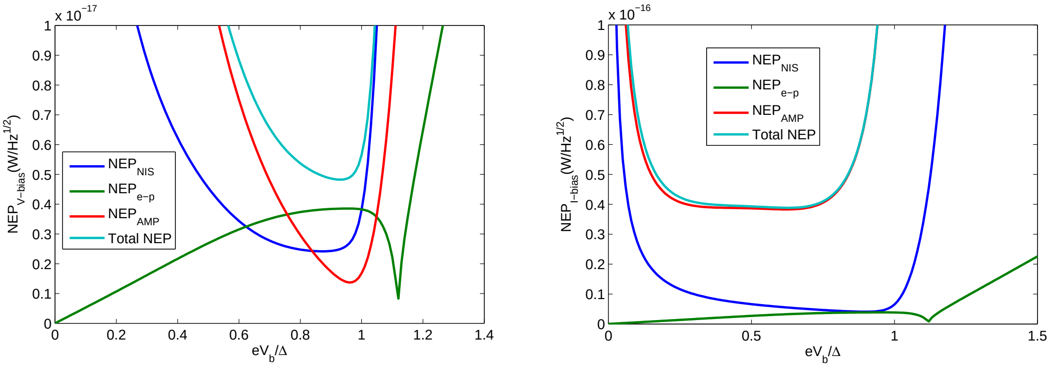

(a) **(b)**

Figure 4.9 – Noise contributions for R=1KΩ. (a) In voltage biased mode, assuming an amplifier noise of $0.05pA/\sqrt{\text{Hz}}$. (b) In current biased mode, assuming an amplifier noise of $3nV/\sqrt{\text{Hz}}$.

4.5 Time Constant

As mentioned in subsection 3.3.3, the time constant is given by $\tau = C/G$, where C is the heat capacity of the absorber, and G is the thermal conductance. Heat is relaxed through two paths; one path is the electron-phonon coupling and the other is the NIS junction through tunneling. Hence, G can be written as $G = G_{e-ph} + G_{NIS}$, and τ can be written as $\tau^{-1} = \tau^{-1}_{e-ph} + \tau^{-1}_{NIS}$. For the voltage biased operation, the time constant is therefore

$$\tau^{-1}_{V-bias} = \frac{1}{c_v \Omega}\left(5\Sigma\Omega T_e^4 + \frac{\partial P}{\partial T}\right) \tag{4.5.0.2}$$

and for the current biased is

$$\tau^{-1}_{I-bias} = \frac{1}{c_v \Omega}\left(5\Sigma\Omega T_e^4 + \frac{\partial P}{\partial T} - \frac{\partial I/\partial T}{\partial I/\partial V}\frac{\partial P}{\partial V}\right) \tag{4.5.0.3}$$

The heat capacity is related to the electron temperature by $c_v = \gamma T_e$, where γ is a material constant.

The time constant for both modes of operations is shown in Figure 4.10.

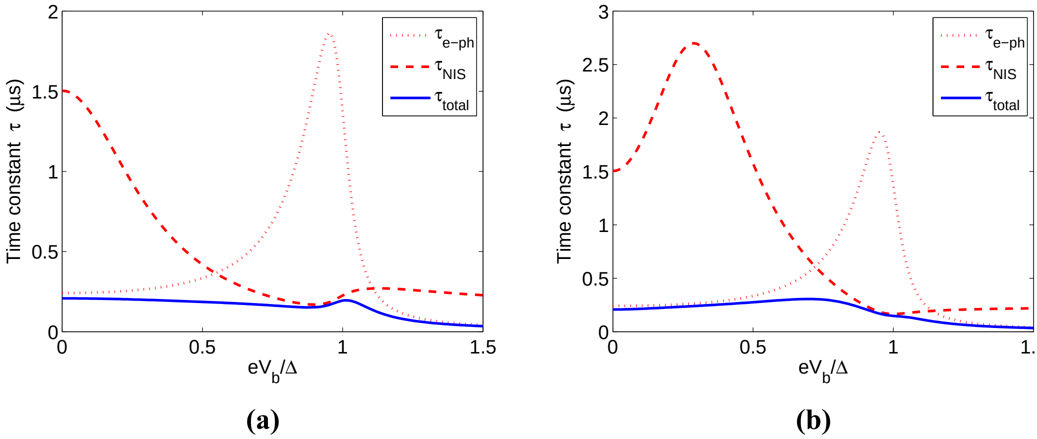

(a) **(b)**

Figure 4.10 – Time constant of the bolometer for an absorber volume of $0.05\mu m^3$, absorber resistance of 100 Ω and $\gamma = 9.77 \times 10^{-17} J/\mu m^3 K^2$. (a) For the voltage biased mode of operation. (b) For the current biased mode of operation.

4.6 Microwave Absorption and Optical Conductivity of a Superconductor

Understanding the characteristics of superconductors at high frequencies is crucial for designing devices out of them. In this section, we will introduce the anomalous skin effect, which occurs at high frequencies and very low temperatures, where Ohm's law is no longer valid. We will also calculate the surface impedance of superconducting niobium by solving Mattis-Bardeen equation in the extreme anomalous limit. Niobium will be used for microstrip lines, as will be shown in next chapter.

4.6.1 Nonlocality and The Anomalous Skin Effect

Consider a normal metal in an external field E. The celebrated Ohm's law $J = \sigma E$, where J is the current density and σ is the complex conductivity, is valid as long as the penetration depth is much larger than the electron mean free path, i.e. $\delta >> l$. In this case the electric filed that the electrons see between scattering events does not vary significantly and this yields a linear relationship between J and E. This is known as local limit.

However, δ decreases with increasing frequency (see Equation 2.3.2.1), and l increases with going to lower temperatures [3]. In this case σ is of the same order of magnitude of l, and the electric field varies rapidly between scattering events and the velocities of the electrons is now dependent on the previous states. Therefore, at high frequencies

---

[3] Low temperature means reduced lattice vibrations, which in turn causes a longer mean free path.

and/or low temperatures Ohm's law stops to be valid, and the current density at a given point no longer depends on the electric field at this point, but it depends on the electric fields in the surrounding volume as well. This non-local relationship between J and E gives rise to what is called anomalous skin effect. At even higher frequencies, the phenomenon is named extreme anomalous effect.

Due to the anomalous skin effect phenomenon, the surface impedance is much higher than that obtained by applying the normal skin effect theory at higher frequencies and low temperatures. In the case of superconductors we replace the skin depth δ by the London penetration depth λ_L, and the mean free path l by the coherence length ζ_0. Therefore, when $\zeta_0 > \lambda_L$, the local J-E relation fails. This analogy was first realized by Pippared [45].

Just one year after the debut of the BCS Theory, Mattis and Bardeen [37] used the BCS theory to derive an expression that relates the current density $J(r)$ at any point r to the magnetic vector potential $A(r)$ of a superconductor. This expression is general. It takes into account the superconductivity gap and the non-local electrodynamics of the superconductor. It is valid for all temperatures $< T_c$ and for all frequencies even those higher than the gap energy $\hbar\omega > 2\Delta$. Mattis-Bardeen Theory allows calculating the complex surface impedance of a thin film as done by Pöpel [46], however, those equations are cumbersome. Fortunately, approximations are possible. Pöpel found that if the film thickness is larger than the penetration depth by at least three times, then bulk limit is a very good approximation. Those calculations can be simplified further when considering Mattis-Bardeen Theory in the extreme anomalous limit. For Nb at 300 mK, λ_L is roughly 50 μm, and for high quality films, l is in the range of 100-1000 μm, therefore the extreme anomalous limit is applicable here. For this approximation, it is convenient to introduce a complex conductivity $\sigma_s = \sigma_1 - i\sigma_2$, which is a function of temperature and temperature, and is given by [46]

$$\frac{\sigma_1}{\sigma_n} = \frac{2}{\hbar\omega}\int_{\Delta}^{\infty}[f(E) - f(E+\hbar\omega]g(E)\,dE + \frac{1}{\hbar\omega}\int_{\Delta-\hbar\omega}^{-\Delta}[1 - 2f(E+\hbar\omega]g(E)\,dE \tag{4.6.1.1}$$

$$\frac{\sigma_2}{\sigma_n} = \frac{1}{\hbar\omega}\int_{\Delta-\hbar\omega,-\Delta}^{\Delta}\frac{[1-2f(E+\hbar\omega)][E^2+\Delta^2+\hbar\omega E]}{(\Delta^2-E^2)^{1/2}[(E+\hbar\omega)^2-\Delta^2]^{1/2}}\,dE \tag{4.6.1.2}$$

where σ_n is the normal state conductivity, $f(E)$ is the Fermi distribution, and $g(E)$ is given by

$$g(E) = \frac{E^2+\Delta^2+\hbar\omega E}{(E^2-\Delta^2)^{1/2}[(E+\hbar\omega)^2-\Delta^2]^{1/2}} \tag{4.6.1.3}$$

The second integral in Equation 4.6.1.1 is set to zero for sub-gap frequencies $\hbar\omega < 2\Delta$. The lower limit on the integral of Equation 4.6.1.2 is $-\Delta$ for $\hbar\omega > 2\Delta$. Figure 4.11 shows the computed results for σ_1 and σ_2 for Nb at 500 mK.

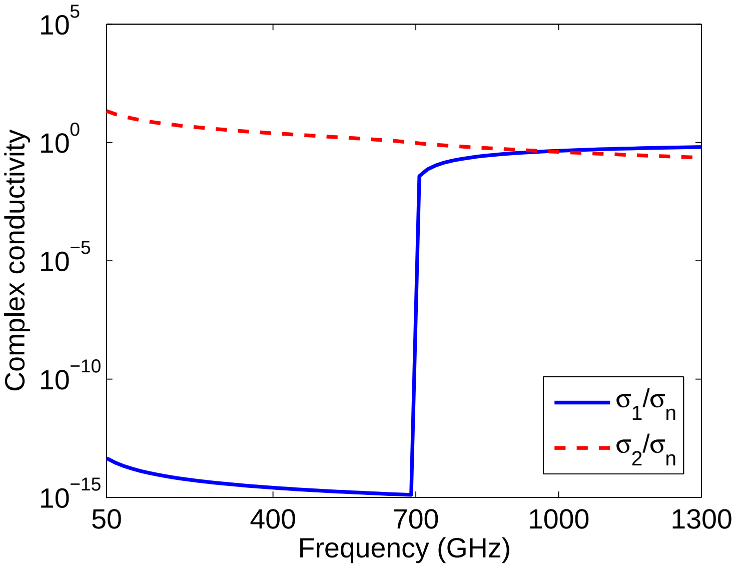

Figure 4.11 – Calculated complex conductivity of Nb film having a thickness of 400 nm at a temperature of 500 mK. For Nb, T_c=9.2 K and $\Delta_0 = 1.8K_BT_c$.

To calculate the surface impedance, the following equation can be used [36]

$$Z_s = (i\omega\mu_0/\sigma)^{1/2}coth[(i\omega\mu_0\sigma)^{1/2}d] \tag{4.6.1.4}$$

where d is the film thickness, and μ_0 is the free space permeability. Figure 4.12 shows the calculated of the real and the imaginary parts of the surface impedance. Nb has a gap energy that corresponds to 700 GHz. Above this frequency, the real part of the surface impedance becomes much higher and losses are introduced. Below this frequency losses are negligible; however, the imaginary part of the surface impedance is significant and gives rise to the kinetic inductance of the superconductor. These values of surface impedance will be used in simulating the superconductor in electromagnetic simulation programs as described in the next subsection.

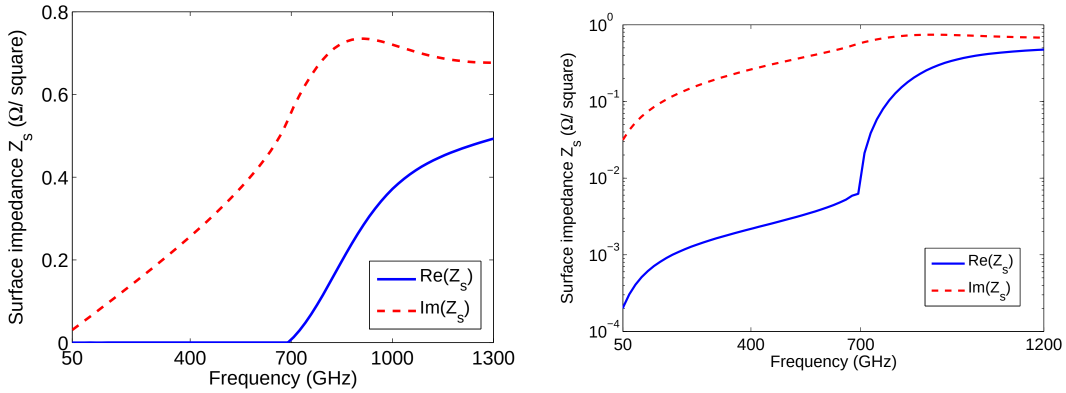

(a) **(b)**

Figure 4.12 – The real and imaginary parts of the complex surface impedance of Nb film of thickness 400nm, and at a temperature of 500 mK. (a) Linear scale. (b) Logarithmic scale.

4.6.2 Simulation Setup in EM Simulators

The characteristics of superconducting thin film microstrip lines depend on the surface impedance of the film. Surface impedance calculations usually encompass complicated numerical computations, such as solution of integral equations or numerical integration. Those calculations are not available in commercial electromagnetic software packages, and so those packages do not provide a means for simulating superconductors directly. Superconductors cannot be represented by just a perfect conductors with zero resistance. The kinetic inductance associated with the superconductors will cause a significant deviation from the expected performance. To obtain accurate results, surface impedances should be computed first then imported into standard microwave programs as a look-up table over the required range of frequencies.

Appendix A.4 presents a MATLAB script that is used to generate frequency-dependent surface impedance tables to be used in electromagnetic simulation. It calculates the surface impedance of Nb thin film using Mattis-Bardeen Theory in the extreme anomalous limit, as was described in the previous subsection, for given material parameters.

In this thesis, two software packages (HFSS [20] and Sonnet em [22]) are used to simulate the superconducting Nb microstrip lines.

This page intentionally contains only this sentence.

Chapter 5

Antenna Design and Simulation

This chapter deals with the design and simulation of the antenna that is coupled to the bolometer. The antenna is needed to couple the radiation to the bolometer since the device is much smaller than the operating wavelength. As we mentioned in the introduction chapter, planar antennas solve many of the problems of horn antenna, however, the field of view of a single antenna is wide and it is needed to restrict the field of view of the detectors to reduce pickup of stray radiation and to correctly couple the detector to the telescope lenses and mirrors. Antenna arrays solves this problem since they could produce narrow beams.

We will begin this chapter by some antenna definitions that we will regularly use. Then, the requirements of the antenna are presented. After that, the design and simulation of the proposed antenna element will be treated. The next natural step, which is making an array out of the antenna element, is then shown.

5.1 Antenna Basic Definitions

5.1.1 Radiation Pattern

The radiation pattern of an antenna is defined as the distribution of the radiated electric field intensity over a sphere having the antenna in its center. The field is considered only as a function of two coordinates (θ and ϕ), while the radial distance remains constant.

Figure 5.1 shows the coordinate system for pattern analysis. Shown also is a typical 3D radiation pattern.

The pattern consists of a main beam in the direction of maximum radiation (called main lobe). There is also some smaller lobes (called side lobes). Cuts through this pattern in various planes are usually used to represent patterns. Those cuts are often made for fixed ϕ values, making the pattern only a function of θ. Those cuts are usually made in both E and H-planes. The E-plane is the plane containing the electric field vector

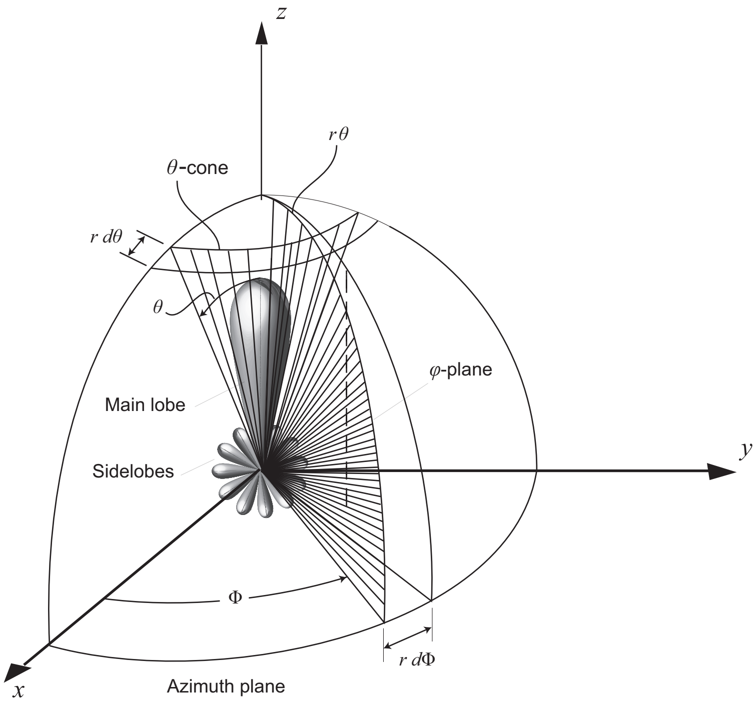

Figure 5.1 – Spherical coordinate system for representing an antenna radiation pattern.

in the direction of the main beam, while the H-plane is perpendicular to the E-plane and containing the magnetic field vector in the direction of the main beam.

At a very large distance r from the antenna [1], the field dependence on distance r and direction (θ, ϕ) is separable and can be expressed as

$$\vec{E}(r,\theta,\phi) = A\frac{e^{-jk_0 r}}{r}\vec{G}(\theta,\phi) \tag{5.1.1.1}$$

where A is a constant related to the excitation of the antenna, the factor $(\frac{1}{r})$ indicates that field decays with distance from the antenna, k_0 is the wave-number in free space, $e^{-jk_0 r}$ is a phase factor, and $\vec{G}(\theta,\phi)$ is the element radiation pattern function. Therefore, to construct the field at any point far from the antenna for a given amplitude and phase, we need only to know its direction dependence $\vec{G}(\theta,\phi)$.

---

[1] This region is known as the farfield region, where $r >> \lambda_0$, where λ_0 is the wavelength in free space.

5.1.2 Directivity and Beam Width

Directivity is the antenna characteristic that tells how much it concentrates energy in one direction compared to other directions. Directivity D is defined as the ratio of the power radiated per unit solid angle in a certain direction to the power radiated by an isotropic radiator that radiates an equal amount of power in all directions. Usually the directivity is expressed in units of dBi, where “i” stands for isotropic. For example, if the directivity of an antenna is 3 (4.77 dBi), it receives 3 times more power in its peak direction than an isotropic radiator would receive.

For an antenna with the effective area “effective aperture” A, the maximum directivity is given by

$$D_{max} = \frac{4\pi}{\lambda^2}A \tag{5.1.2.1}$$

One representation of the beam width is what is called Full Width at Half Maximum (FWHM), which is the angular width at which the power is equal to half of its maximum value, as shown in Figure 5.2.

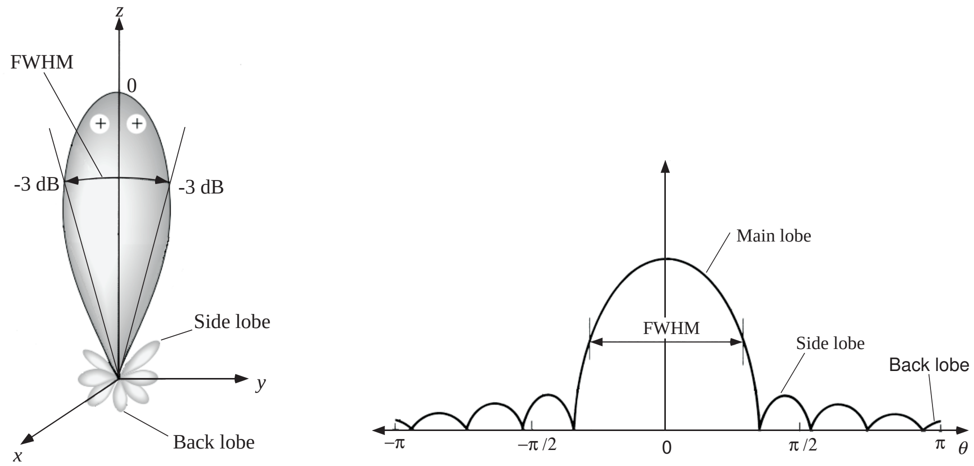

(a) **(b)**

Figure 5.2 – Two-dimensional normalized power pattern to illustrate the beamwidth. (a) Polar plot. (b) Linear plot.

A measure for how much power is concentrated in the main beam compared to the side lobe is the “side lobe level”. It is defined as the ratio between the maximum pattern value of a side lobe to the maximum pattern value of the main beam, and is usually expressed in dB.

5.1.3 Co-polarization and Cross-polarization

As mentioned in subsection 5.1.1, the antenna field has two orthogonal components along θ and ϕ. The co-polarization vector is defined as the preferred electric field vector. The cross-polarization vector is orthogonal to co-polarization vector and represents the undesired polarization. Both the co-polarization vector and the cross-polarization vectors are orthogonal to direction of propagation. The selection of the preferred polarization direction is arbitrary, however, we will follow Ludwig's second definition [35] [2]. According to this definition, the co-polarization and cross-polarization components of the field at a point (θ , ϕ) are defined as

$$\boldsymbol{E}_{\text{co}}(\theta,\phi) = \boldsymbol{E}(\theta,\phi)\,.\left(\frac{\sin\phi\,\cos\theta\,\hat{\theta} + \cos\phi\,\hat{\phi}}{\sqrt{1-\sin^2\theta\,\sin^2\phi}}\right) \tag{5.1.3.1a}$$

$$\boldsymbol{E}_{\text{cross}}(\theta,\phi) = \boldsymbol{E}(\theta,\phi)\,.\left(\frac{\cos\phi\,\hat{\theta} - \cos\theta\,\sin\phi\,\hat{\phi}}{\sqrt{1-\sin^2\theta\,\sin^2\phi}}\right) \tag{5.1.3.1b}$$

Figure 5.3 shows those two components for easier visualization.

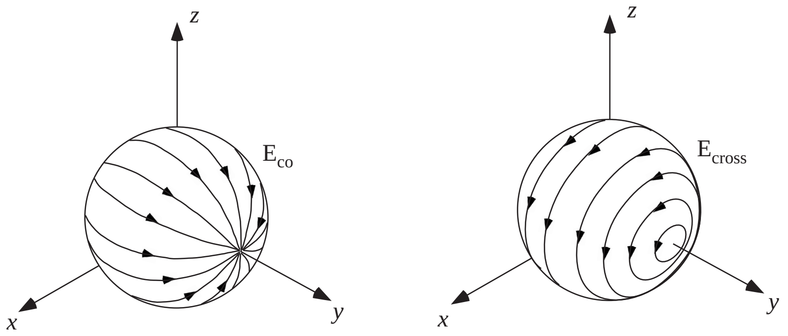

Figure 5.3 – The co-polarization and cross-polarization components according to Ludwig second definition.

According to the "IEEE Standard Definition of Terms for Antennas" , we define the cross-polarization level (CPL) as

$$CPL \equiv \frac{|\boldsymbol{E}_{\text{cross}}|_{max}}{|\boldsymbol{E}_{\text{co}}|_{max}} \tag{5.1.3.2}$$

The cross polarization level is usually specified in negative dB, indicating how many decibels the undesired polarization is below the desired polarization. For our detector,

---

[2] On the other hand, Ludwig's third definition has more practical significance since it is easier to measure practictice. However, since we are doing simulations here and no pattern measurements are carried out, we will follow the second definition which is more meaningful.

having a low cross-polarization is crucial.

5.1.4 Input Impedance

The radiation resistance for an antenna is defined as the resistance that dissipates the same amount of power as the antenna radiated power, if the antenna was replace by this resistance. In this situation, the transmitter sees exactly the same thing either with the antenna or with the radiation resistor. However, while the energy dissipated in an ohmic resistance is converted to heat, the energy dissipated by radiation resistance is converted to electromagnetic radiation. Generally, the input impedance is complex, with the real part (resistance) related to the radiated power, and the imaginary part (reactance) related to the energy stored by fields in the vicinity of the antenna. Both influence the matching between the antenna and the feeding structure, and hence affecting the antenna efficiency.

5.2 Simulation Methods and Software Packages

In this thesis, simulations were carried out using a combination of commercial packages (Ansys HFSS [20], CST Microwave Studio [21], Sonnet em [22]).

Generally, electromagnetic simulators are divided into two types: (i) three-dimensional solvers, such as HFSS and CST, which divide the structure to three-dimensional mesh, and solve Maxwell's equations in each mesh element, and (ii) two-dimensional solvers, like Sonnet, which divides the conducting surfaces to two-dimensional mesh and uses method of moment to solve for the currents. Furthermore, the three-dimensional solvers are divided to frequency domain solvers (e.g. HFSS), and time domain solvers (e.g. CST).

The advantage of using different solvers is double fold. Firstly, depending on the structure, some solvers are more appropriate than the others. For instance, for planar circuits, 2-D simulators can produce accurate results much faster and with much lower memory requirements than 3-D solvers. Secondly, the use of different packages based on different theoretical methods (time and frequency domain for example) provides a means to judge the quality of simulation results. If the results are in good agreement, then the results are trustable, otherwise, further investigations are necessary.

5.3 Slot Antenna

5.3.1 Rectangular Slot Antenna

A rectangular slot is a narrow opening in a large conductive sheet known as the ground plane as shown in Figure 5.4.

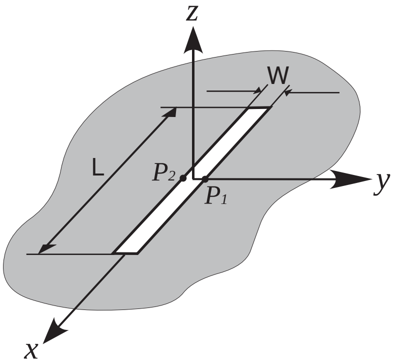

Figure 5.4 – Slot antenna on an infinite ground plane.

The key motivations for choosing a slot antenna are:

- The ground plane isolates the incoming radiation and feeding circuit, which prevents the feeding structure from degrading the cross-polarization level. This also allows for independent design procedures for the antenna and the complicated feeding network required in arrays.
- Narrow slots are intrinsically polarization sensitive.
- cheap and accurate to manufacture.

When $W << \lambda$, the semi-infinite ground planes along the slot length can be considered as a section of two-wire transmission line [13]. Those two lines are being shorted at both ends of the slot. When the slot is excited by connecting a source to points P1 and P2, the excited voltage propagates towards the slot's short-circuited ends. This wave gets reflected by the slot termination. When the slot length L is odd multiple of half wave length ($\lambda/2$), the two waves reflected by both ends create a standing wave on the slot. A current standing wave also exists. Since the slot end is shorted, the voltage at the end is zero, while the current is maximum. The current and voltage standing waves for lambda/2 slot are shown in Figure 5.5.

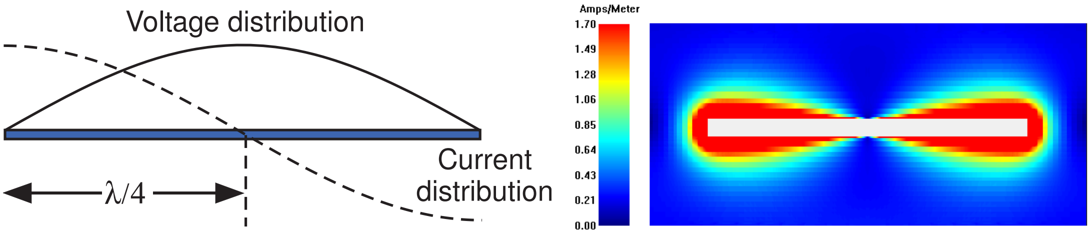

(a) **(b)**

Figure 5.5 – (a)Standing voltage and current waves in a slot. (b) Simulated current distribution using Sonnet package. The figure shows two current maximums at both ends of the slot and a current null at the center.

The slot can also be conceived as a short waveguide, whith the thickness of the ground plane acts as the length of this wave guide. For narrow ($W << \lambda$) half wavelength slot, the E-field distribution over the slot is reasonably approximated by the TE_{10} mode of the rectangular waveguide [24]. For an x-directed slot having the origin of the coordinate system in its center, the slot field becomes

$$\boldsymbol{E}_{\text{slot}}(x, y) = E_0 \cos\left(\frac{\pi}{L} x\right) \hat{\boldsymbol{y}} \tag{5.3.1.1}$$

Figure 5.6a shows the E-field distribution on the slot. The E-field can be replaced by an equivalent magnetic currents M [3].

$$\boldsymbol{M} = \boldsymbol{E}_{\text{slot}} \times \hat{\boldsymbol{z}} = E_0 \cos\left(\frac{\pi}{L} x\right) \hat{\boldsymbol{x}} \tag{5.3.1.2}$$

The equivalent magnetic current is shown in Figure 5.6b. This fact can be exploited to speed up the simulation of a slot antenna. Instead of solving for the currents in the ground plane, we can just remove the ground plane and replace the slot by its magnetic current.

This E-field in the slot (or equivalently the magnetic current along the slot) radiates equally into both sides of the slot. The radiation pattern resembles the well-known ”doughnut” shaped pattern of a dipole antenna. Figure 5.7 shows the simulated radiation pattern of a slot if free space. The field pattern has $cos(\theta)$ dependence in H-plane, and constant in E-plane.

---

[3] Magnetic current is a fictitious current that results from the symmetry of Maxwell’s equations. While an electric current gives rise to a magnetic field, a magnetic current gives rise to an electric field.

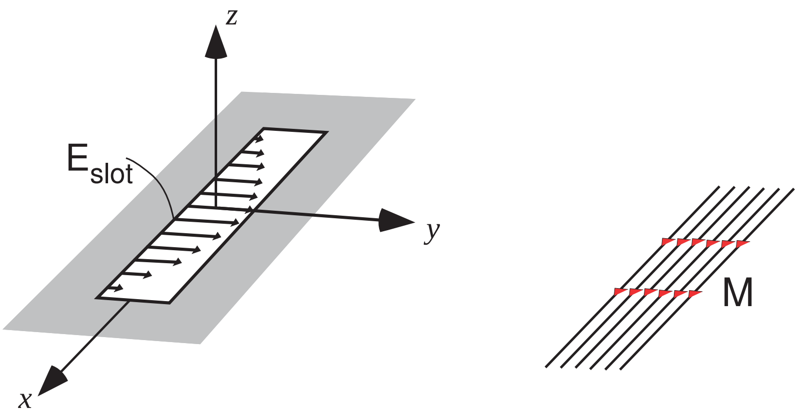

(a) **(b)**

Figure 5.6 – (a) Electric field distribution across the slot. (b) The equivalent magnetic current.

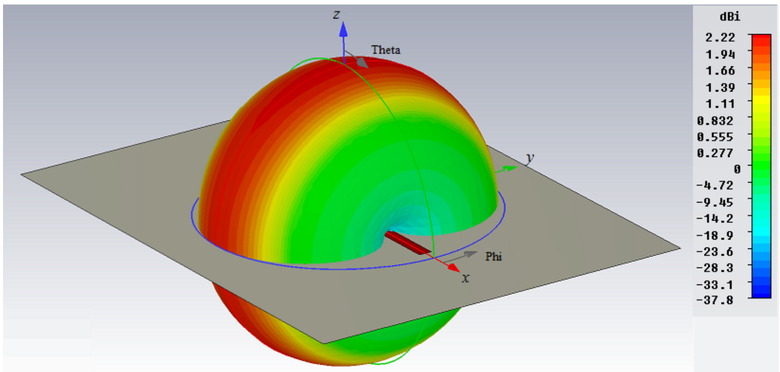

Figure 5.7 – Radiation Pattern of slot antenna in free space simulated using CST.

The E plane is the yz-plane, while the H plane is the xz-plane.

5.3.2 Offset Feeding

A center-fed half-wavelength slot has high input impedance because at the center the current is minimum while the voltage is maximum. A center-fed slot on a dielectric substrate has a typical input impedance of 500 - 600 ohm [47]. This makes it difficult to match the antenna to the bolometer and the feeding network. A solution to this problem is to shift the feeding point from center towards the edge as suggested by [59]. This technique is called “offset feeding”.

5.3.3 Microstrip Feeding of Slot Antenna

Since the final goal is to design an array of slot antennas, a feeding mechanism that allows summing the signals from all the antennas should be used. The best method to

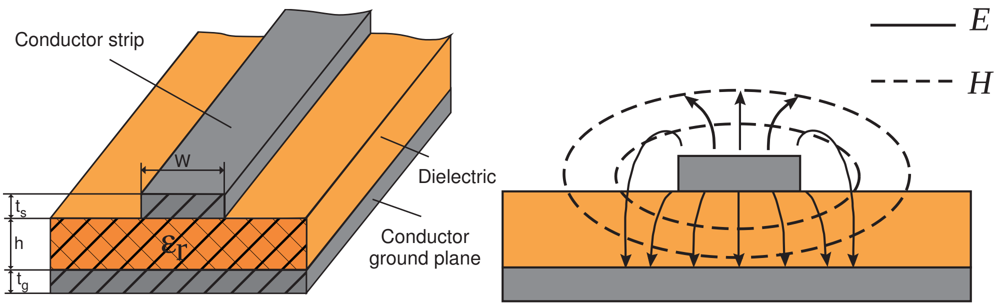

(a) **(b)**

Figure 5.8 – The microstrip line. (a) Geometry. (b) Distribution of the fields

do this is to feed the slot from beneath using a microstrip line. The slot electric field distribution is hardly affected by the type of excitation [24].

Figure 5.8a a shows the geometry of a microstrip line. It consists basically of a conductor of width W printed on a thin, grounded dielectric substrate. The relative permittivity of the substrate is ε_r and its thickness d . Figure 5.8b shows the fields distribution.

Since most of the field lines are in the dielectric region (because of its high dielectric constant compared to the air above the microstrip), and some fraction in the air above the microstrip, we have what is called the effective dielectric constant ε_{eff}. It depends on the substrate relative permittivity, the substrate thickness, the conductor width, and the frequency, and is given by [48]

$$\varepsilon_{eff} = \frac{\varepsilon_r + 1}{2} + \frac{\varepsilon_r - 1}{2}\frac{1}{\sqrt{1 + 12d/W}}$$

It could be thought of as the dielectric constant of the homogeneous medium that could replace both the substrate material and the air above it.

The characteristic impedance Z_0 of a uniform transmission line is defined as the ratio of the magnitude of voltage and current of a single wave propagating along the line, i.e. in absence of reflection. By voltage we mean the potential difference between the line and the ground, and by current we mean the surface current flowing in the microstrip line. This ratio is a constant which is independent of the location, and for a lossless tansmission line, it is given by the following relation

$$Z_0 = \sqrt{\frac{L}{C}}$$

where L is the line inductance per unit length, and C is the shunt capacitance per unit length. In our particular case of a superconductor microstrip, L is replaced by L_{kin}, the kinetic inductance of the superconductor, which is frequency dependent.

The current flowing in a microstrip line induces a current in the ground plane in the opposite direction. This induced current is cut by the slot. When this current goes around the slot to continue to its desired direction, it acts as an excitation for the slot and radiation occurs. In the receive mode, the current induced around the slots couple to the microstrip lines.

5.3.4 The Effect of the Substrate

Planar antennas has to be printed on a substrate. Antennas on substrates radiate most of their energy into the dielectric. The slot radiates power more strongly into the dielectric than into the air by a factor of $\varepsilon_r^{3/2}$ [54]. Therefore, it is desirable to have a substrate of high dielectric constant. In our design we use silicon with $\varepsilon_r = 11.8$ as a substrate material.

Unfortunately, antennas on planar dielectric substrates lose power to what is called substrate modes. As shown in Figure 5.9, all the energy radiated above the critical angle experiences total internal reflection and is trapped in the substrate as surface waves.

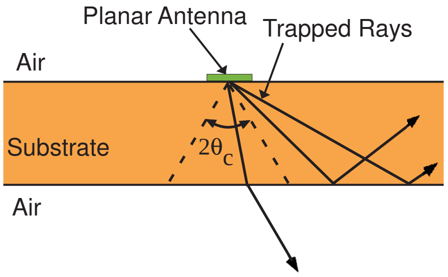

Figure 5.9 – A planar antenna on a dielectric substrate and the power loss due to substrate modes.

It is favorable to choose the substrate thickness near odd multiples of a quarter wavelength in the dielectric to minimize the trapped power in the substrate.

Another issue concerning the substrate, especially those having a high dielectric constant, is that power get reflected at the interface between the substrate and the air due to the large difference between the refractive index. To circumvent this problem, usually a layer of anti-reflection (AR) coating is used. An anti-reflection coating is a material having a refractive index between that of the air and the substrate. For silicon substrate, a quartz layer ($\varepsilon_r = 3.7$) is usually used.

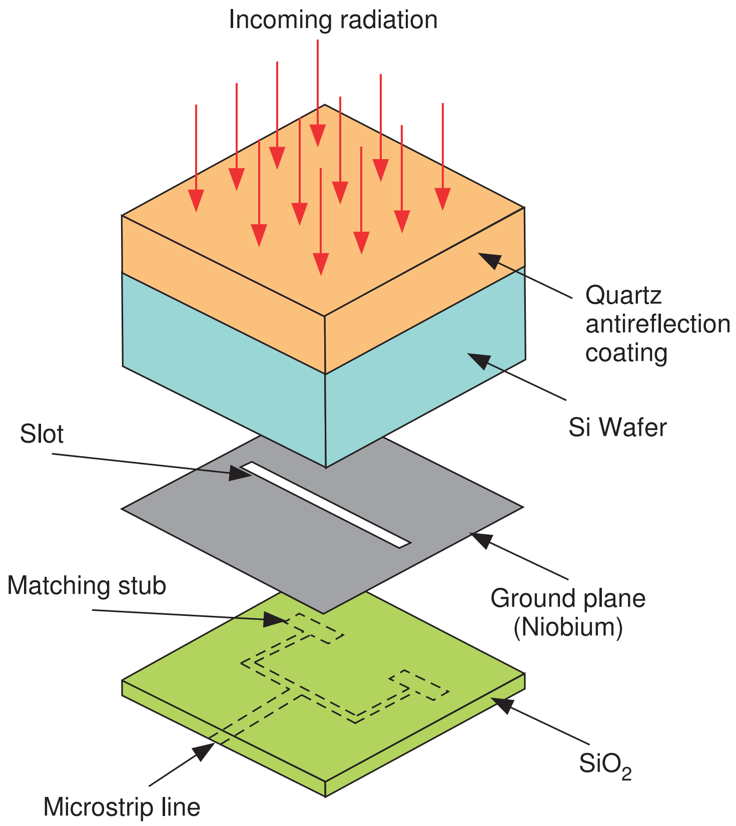

Figure 5.10 – A 3D view of the slot antenna and microstrips.

5.4 Slot Antenna Design and Simulation

In this section we will explain the design procedures along with the simulation results for both of the slots operating at 75 GHz and 105 GHZ. Figure 5.10 shows a 3D view of the slot antenna we want to design.

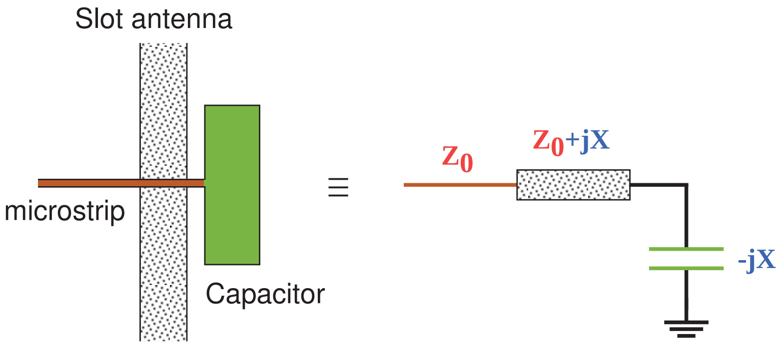

Figure 5.11 – The coupling capacitor used for impedance matching.

The antenna is fabricated on a silicon substrate. The radiation comes through the AR-coating and the substrate to take advantage of the strong radiation in this side. A voltage difference is excited across the slot. A coupling capacitor (knows as stub) , see

Figure 5.11, is used to cancel out the inductive reactance of the offset-fed slot antenna so that the slot input impedance is purely real and could be matched to the real impedance of the microstrip line.

The silicon dioxide that couples the microstrip to the niobium ground plane is chosen to be electrically very thin ($h << \lambda$, see Figure 5.8a) for two reasons. Firstly, to reduce the frequency dependence of the line and to suppress the non-TEM modes, so the fields are quasi-TEM [48]. So it becomes possible to use simple transmission line theory and its numerical analysis techniques. And secondly, to reduce the radiation from the microstrip lines. A microstrip line acts like an antenna. If the line is close to the ground plane, the radiated wave at a large distance generated by the current in the line tends to cancel the radiated wave from the opposite current excited in the ground plane. The thickness of this layer is chosen to be 0.3 μm.

5.4.1 Choosing Slot Dimensions

For a slot to resonate at the desired frequency, its length should be nearly half wavelength. It is the guided wavelength in the medium (λ_g) that should be considered here, not the wavelength in free space (λ_0). They are related by $\lambda_g = \lambda_0/\sqrt{\varepsilon_{eff}}$, where ε_{eff} is the effective dielectric constant of the medium surrounding the slot. In our case, the slot lies on the interface between the silicon substrate and the air [4]. When a wave propagates along a metal at a dielectric interface, it propagates at an intermediate velocity between the velocity of the wave into the dielectric and the velocity of the wave into the air, as it was verified in [6]. Usually the velocity is close to the velocity in a medium whose dielectric constant is the mean of the two mediums. Therefore, the slot guided wavelength is roughly given by

$$\lambda_g = \lambda_0/\sqrt{(\varepsilon_{r,Si} + \varepsilon_{r,Air})/2} \tag{5.4.1.1}$$

At this point of the design, we use CST MWS to find the slot length. For this purpose it is adequate at simulate only the slot without the microstrip lines or the coupling capacitors, by feeding the slot by a voltage source from the center.

For the 75 GHz slot, Equation 5.4.1.1 was evaluated to find the slot length, which gave very good initial value for the slot length. Further tuning shows that the required slot length is 720 μm. This is verified by viewing the real part of the input impedance since at resonance, the real part of the impedance peaks, as shown in Figure 5.12.

---

[4] the 0.3 μm SiO_2 layer is neglected here since its thickness is much smaller than the wavelength.

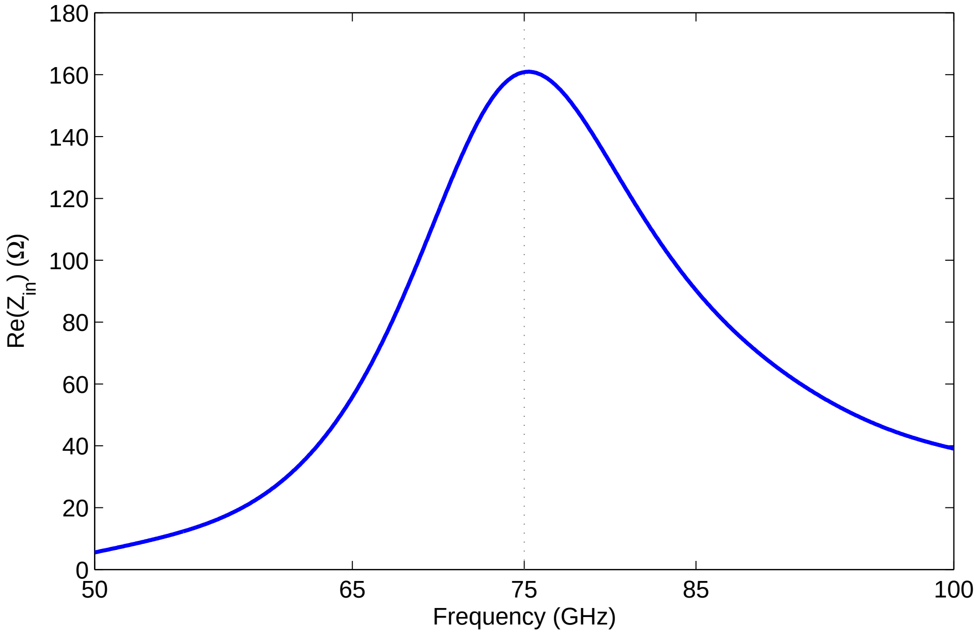

Figure 5.12 – The real part of the input impedance of a slot of length 720 μm simulated with CST MWS. At this length, the slot resonates at 75 GHz and the input impedance has a peak.

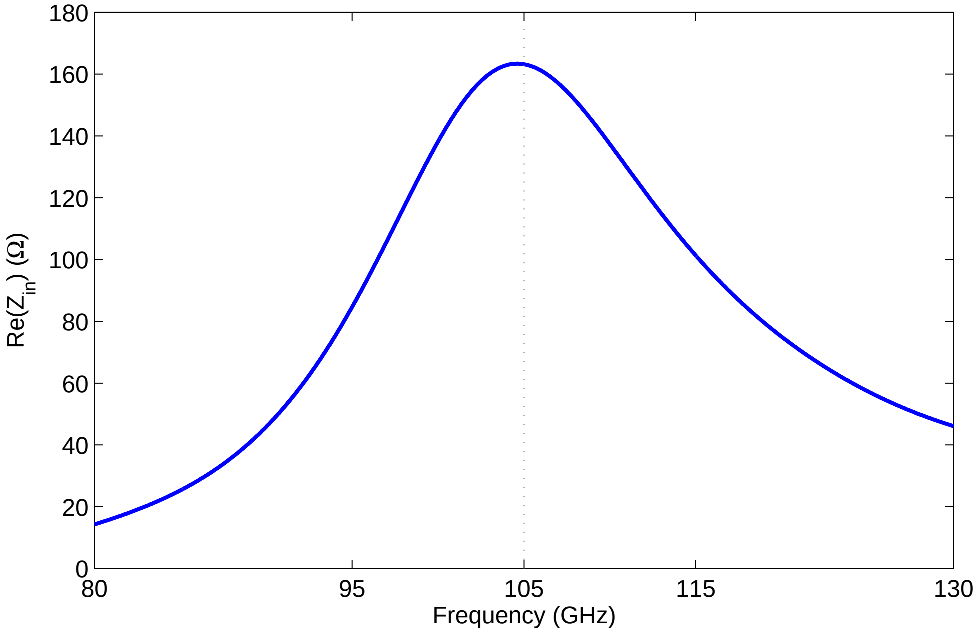

Figure 5.13 – The real part of the input impedance of a slot of length 525μm simulated with CST MWS. At this length, the slot resonates at 105 GHz and the input impedance has a peak.

The slot width W is chosen such that ($W << \lambda$) to excite single mode and have low cross polarization. A narrow slot could also be very well represented by the magnetic current across the slot. We choose the width of the slot to be 22 μm.

The same procedures were followed for the 105 GHz slot. The slot length at this frequency is found to be 525 μm. Figure 5.13 shows the real part of the input impedance. The width of the slot is chosen to be 16 μm.

5.4.2 Choosing Feed Offset

As was mentioned earlier, a center-fed slot has a high input impedance and offset feeding solves this problem (see subsection 5.3.2). We want to find the offset distance, see Figure 5.14, at which the real part of the input impedance is 50 Ω, so the antenna is matched to the impedance of the microstrip line, which will be designed to have Z_0=50 Ω as well.

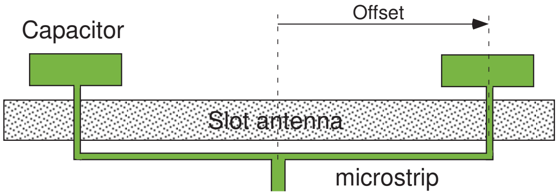

Figure 5.14 – Offset feeding the slot antenna.

HFSS is used for this purpose since it was able to account accurately for the superconducting microstrip line characteristic impedance. A problem arises when trying to find the input impedance of the microstrip-fed slot; the problem is that we have to use the coupling capacitor for correct operation, however, this capacitor will alter the input impedance. To overcome this problem, we make use of a dummy capacitor. We fist simulate an auxiliary capacitor having dimensions of 50x10 μm on a grounded 0.3 μm SiO_2 layer in the desired range of frequency, as shown in Figure 5.15. The input impedance changes with the length of the transmission line. To get the reactance of the capacitor excluding the transmission line, we “de-embed” the port as represented by the blue arrow in Figure 5.15. De-embedding means excluding the effect of the transmission line when calculating the impedance of the structure under test, which is analogous to eliminating the effect of probes during measurements in the lab.

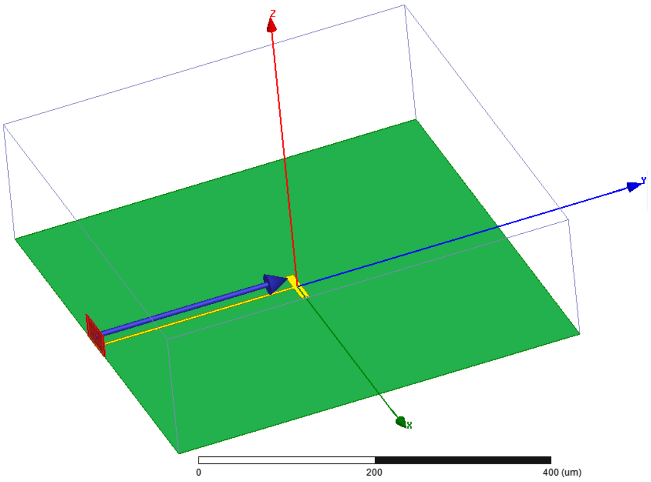

Figure 5.15 – HFSS simulation setup for the auxiliary capacitor. The port “red rectangle” feeds the structure. To get the reactance of the capacitor we de-embed the port. The head of the blue arrow points at the point at which the impedance is calculated.

After obtaining the reactance of the auxiliary capacitor, we then simulate the slot with this known capacitor and find the input impedance of the whole structure (de-embedding is also applied here). Then the reactance of this known capacitor is subtracted from the total input impedance to yield the input impedance of the slot itself. The simulation setup is shown in Figure 5.16.

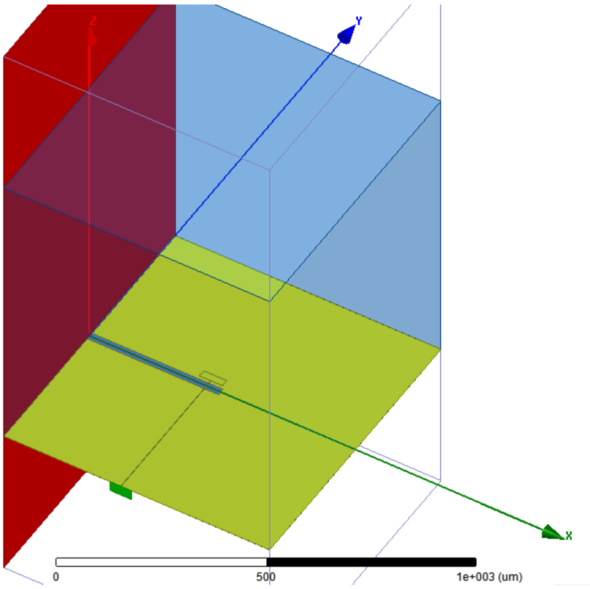

Figure 5.16 – HFSS simulation setup for calculating the input impedance of the slot. The auxiliary capacitor in Figure 5.15is used. The red plane is a magnetic symmetry plane that enforce symmetric solution and save simulation time.

To save simulation time, we make use of the fact that the structure is symmetric by simulating only one half of the structure. This is implemented by using what is called symmetry planes in the electromagnetic simulation software packages. The type of the symmetry plane we should use here is magnetic symmetry plane (the red plane in Figure 5.16). Magnetic symmetry plane means that the magnetic field is perpendicular to it. Since the magnetic field is parallel to the magnetic current, magnetic symmetry plane is also perpendicular to the magnetic current of the slot.

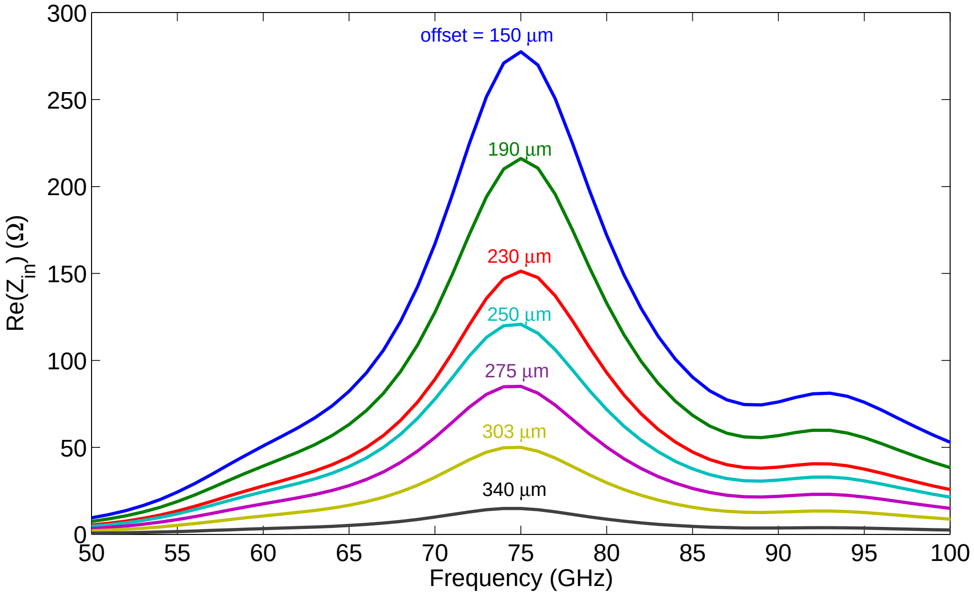

(a)

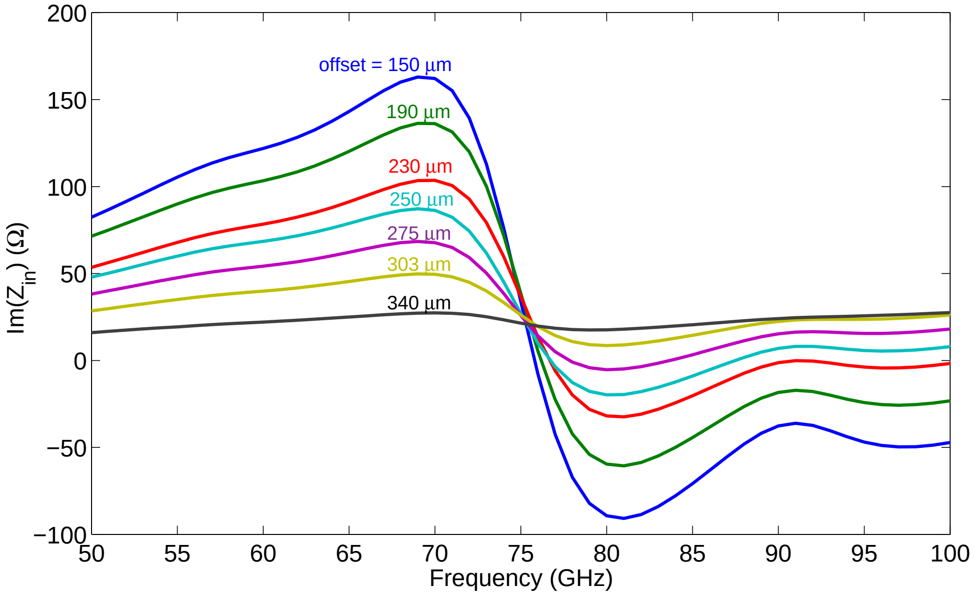

(b)

Figure 5.17 – Simulated input impedance of the 75 GHz slot for different offset feeding distances. (a) The real part. (b) The imaginary part.

A sweep is performed on the offset distance to find the required distance that gives 50 Ω real input impedance. Fig Figure 5.17 shows the result of this sweep for the 75 GHz slot, while Figure 5.18 shows the sweep result for the 105 GHz slot.

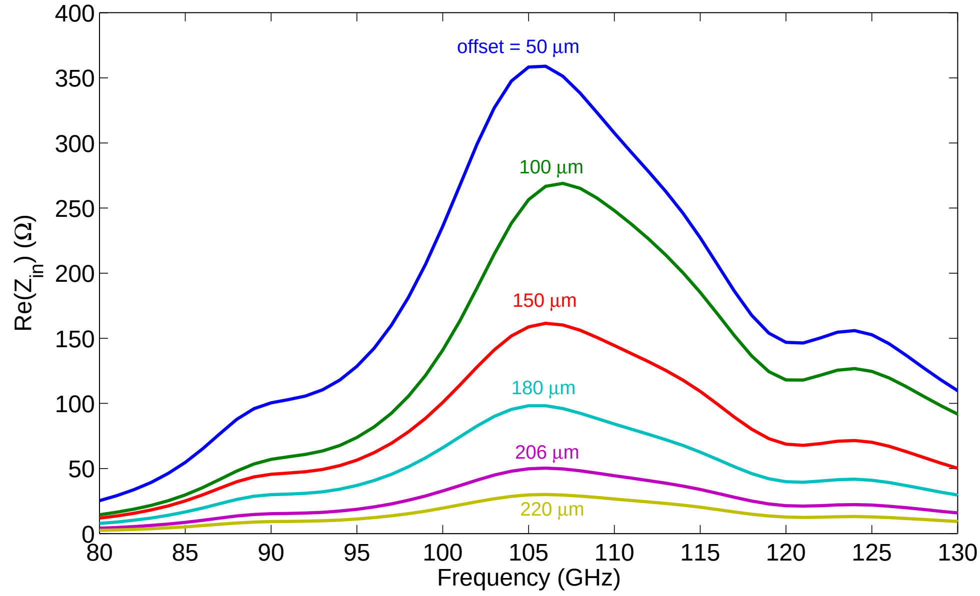

(a)

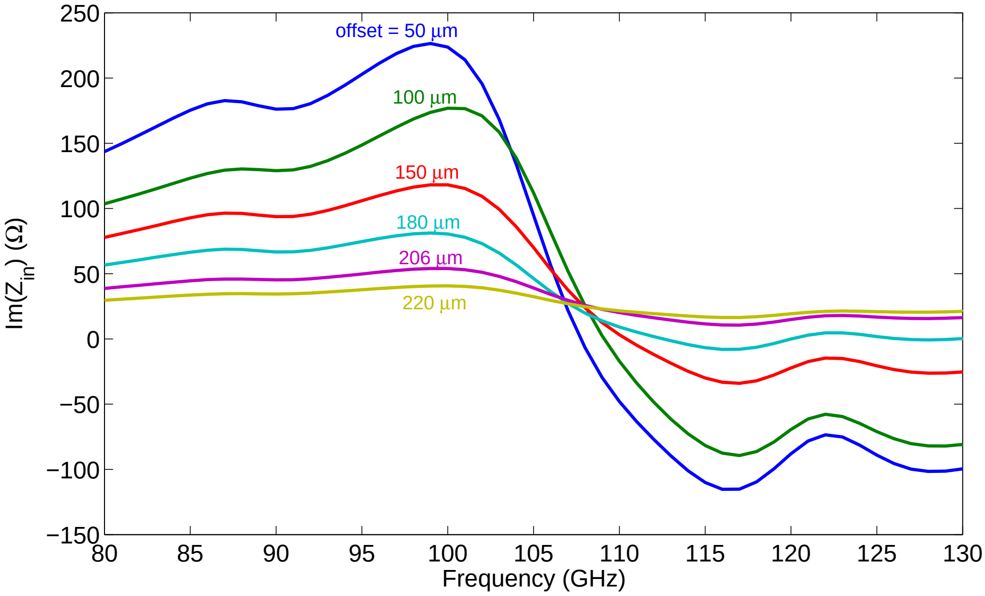

(b)

Figure 5.18 – Simulated input impedance of the 105 GHz slot for different offset feeding distances. (a) The real part. (b) The imaginary part.

This input impedance behavior is in accord with that theoretically calculated using the moment method [26, 47], the “complex radiated power and discontinuity in the modal voltage” method [10, 49], network modeling [2, 25], and experimentally measured [59].

According to Figure 5.17 and Figure 5.18, an offset distance of 303 μm gives an input resistance of 50 Ω for the 75 GHz slot, while an offset distance of 206 μm gives an input resistance of 50 Ω for the 105 GHz slot.

5.4.3 Matching

The process of matching the slot to the feeding network involves both choosing the correct dimensions of the coupling capacitor to compensate the inductive reactance of the slot, and choosing the width of the microstrip line that feeds the slot.

As seen in the input impedance curves (Figure 5.17 and Figure 5.18), the slot has two resonances. The first resonance corresponds to a high input resistance whereas the second resonance corresponds to a low one. The second resonance is associated with a quiet constant real part of the input impedance. This leads to a wideband behavior around the second resonance, but here we choose to operate at the first resonance since it results in shorter slots, which is suitable for arrays.

According to Figure 5.17 and Figure 5.18, the imaginary part of the 75 GHz slot is +j26 Ω, whereas the imaginary part of the 105 GHz slot is +j39 Ω at resonance. To design the capacitors that will match this reactance, a simulation setup like that was shown in Figure 5.15 is used but with varying the dimensions of the capacitor till achieving the required result at the frequency of operation. For the 75 GHz slot, a capacitor of dimensions 59x11 μm was found to have a reactance of –j26 Ω at 75 GHz as shown in Figure 5.19a, while a capacitor of dimensions 31x10 μm was found to have a reactance of –j39 Ω at 105 GHz to match the 105 GHz slot as shown in Figure 5.19b.

To simulate the superconducting Nb microstrip line, we follow the procedures explained in subsection 4.6.2. To find the width of the superconducting Nb microstrip line that has an impedance of 50 Ω on top of 0.3 μm thick SiO_2 layer, we do a sweep of the line width at the intermediate frequency of 90 GHz. Figure 5.20a shows that a line of width 0.9 μm has the required characteristic impedance. Even though the line is designed at 90 GHz, its characteristic impedance does not change a lot over the operation frequency band, as shown in Figure 5.20b.

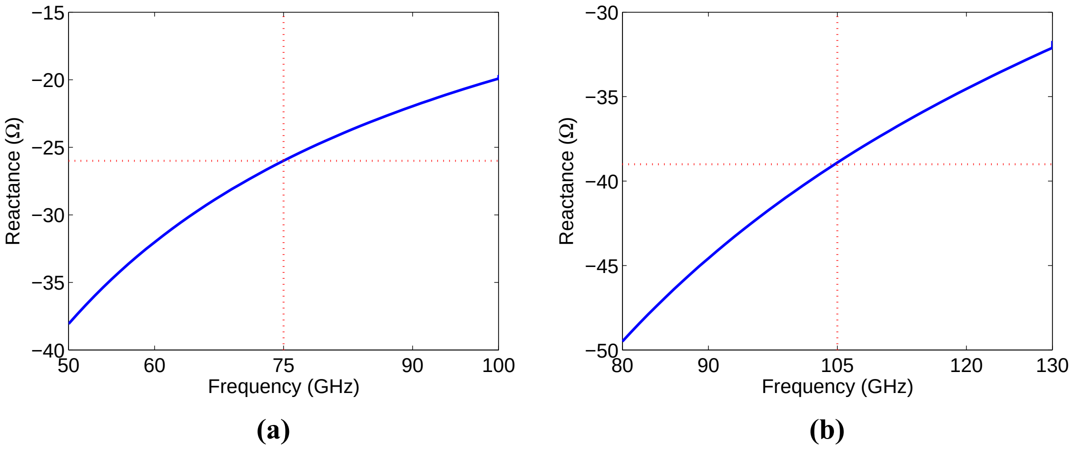

Figure 5.19 – Simulated reactances of the coupling capacitors to achieve matching. (a) A capacitor of dimensions 59x11 μm has a reactance of –j26 Ω at 75 GHz. (b) A capacitor of dimensions 31x10 μm has a reactance of –j39 Ω at 105 GHz.

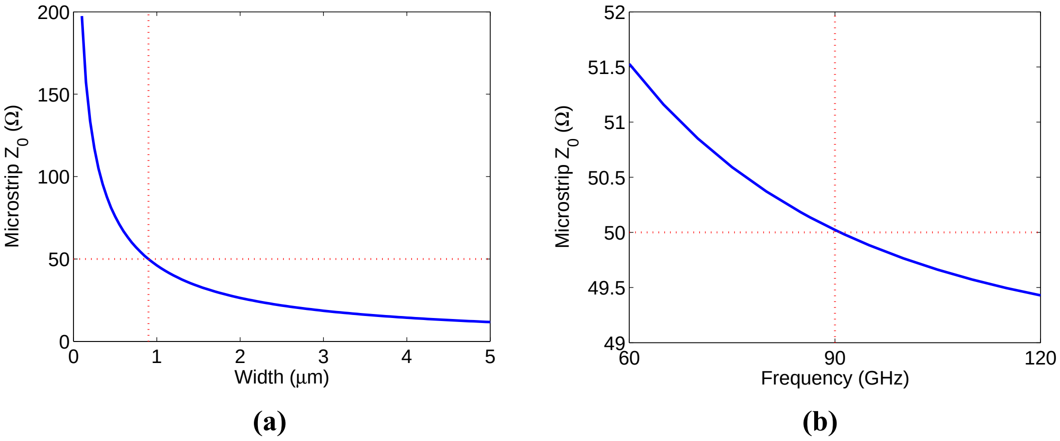

Figure 5.20 – Characteristic impedance of superconducting Nb microstrip line on top of 0.3 μm SiO_2 layer. (a) As a function of width at 90 GHz. (b) 0.9 μm line as a function of frequency.

The results for matched slots are shown in Figure 5.21.

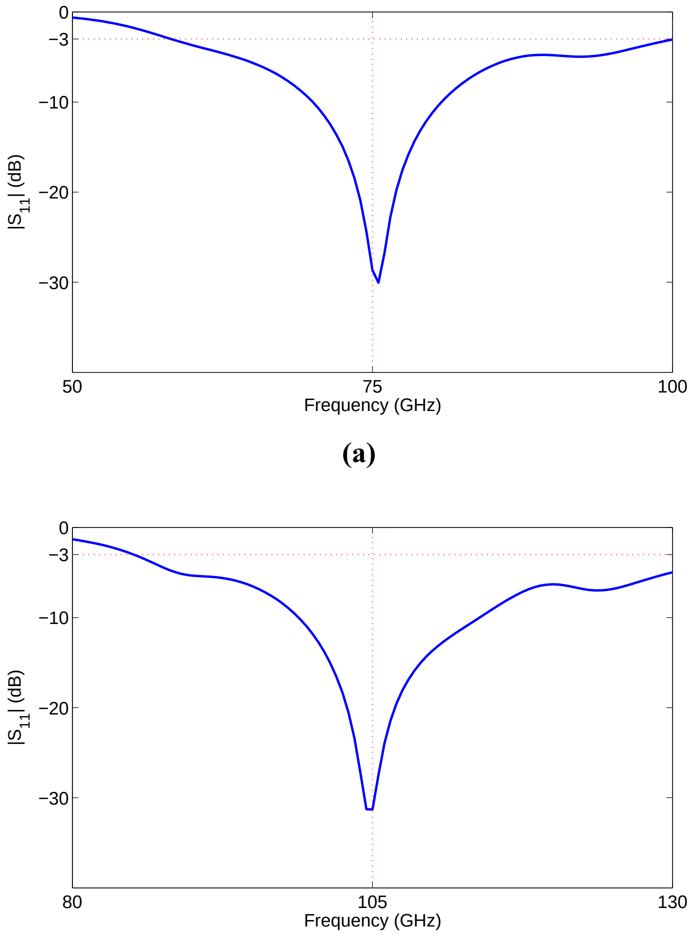

(a)

(b)

Figure 5.21 – Reflection coefficient for matched slots. (a) For the 75 GHz slot. (b) For the 105 GHz slot. The bandwidth at -3 dB level is quiet large.

5.4.4 Choosing the Substrate Thickness

It was mentioned in subsection 5.3.4 that to reduce the trapped power in the substrate, the thickness of the substrate should be odd multiple of quarter wavelength in the dielectric. The problem here is that we have two frequencies on the same substrate. Here we choose the substrate thickness to be 1445 μm. This thickness satisfies the aforementioned condition for both frequencies of 75 GHz and 105 GHz. It is five times quarter wavelength at 75 GHz in silicon, and it is seven times the quarter wavelength at 105 GHz in silicon.

5.5 Antenna Arrays

A phased array antenna is a regular arrangement of identical radiating elements. The field radiated by an antenna array is therefore the superposition of the individual element fields. The main goal of using an array is to have a very directive pattern, i.e. the antenna radiates very strongly in one direction. This is achievable by making the fields from the elements interfere constructively in the desired directions and interfere destructively in the remaining of the space. Referring to Equation 5.1.2.1, we will find that the directivity of the array is much larger than that of a single element since an array provides much larger radiating area A. Therefore, the array beam width is much smaller than the element beam width.

The pattern of an array depends on the following parameters:

- The pattern of the individual elements.
- The elements' geometrical arrangement (linear, rectangular, circular, etc.).
- The number of elements.
- The relative displacement between the elements.
- The excitation amplitudes of the elements.
- The excitation phases of the elements.

The radiation pattern function $\vec{G}(\theta, \phi)$ of an element described in Equation 5.1.1.1 gives the radiation pattern of the element when the origin of the coordinate system is at the center of the element. However, if the element is moved by a distance r_0 relative to the original coordinate system, as shown in Figure 5.22, the new pattern is then given by [24]

$$\vec{G}'(\theta, \phi) = \vec{G}(\theta, \phi) e^{jk_0 r_0 . \hat{r}} \tag{5.5.0.1}$$

Now consider a planar 2D array as shown in Figure 5.23. The element spacing in x-direction is d_x, and d_y in y direction.

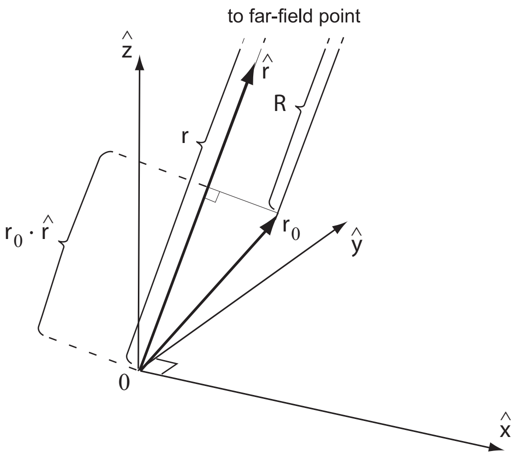

Figure 5.22 – Moving the element from the origin to a point r_0.

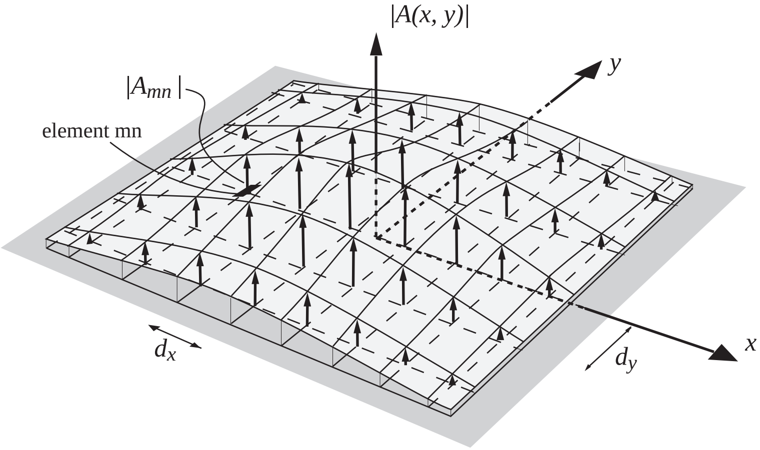

Figure 5.23 – Planar rectangular antenna array. Shown also the complex excitation amplitude A of the elements.

From Equation 5.5.0.1 and using superposition, the far-field function of the whole array at a far point r can be written as

$$\vec{G}_{Array}(\theta,\phi) = \sum_{n=1}^{N}\sum_{m=1}^{M} A_{mn}\vec{G}(\theta,\phi)e^{jk_0 r_{mn}\cdot\hat{r}} \tag{5.5.0.2}$$

where A_{mn} is the complex excitation (amplitude and phase) of the element mn and r_{mn} is the displacement of the element mn relative to the origin.

This equation can be rearranged and written as

$$\vec{G}_{Array}(\theta,\phi) = \vec{G}(\theta,\phi)\sum_{n=1}^{N}\sum_{m=1}^{M} A_{mn}e^{jk_0 r_{mn}\cdot\hat{r}} = \vec{G}(\theta,\phi)AF(\theta,\phi) \tag{5.5.0.3}$$

where AF is what is called the array factor. Therefore, the far-field of the array can be obtained by multiplying the field of the single element by the array factor. This process of factoring the array pattern into an element pattern multiplied by an array factor is known as pattern multiplication principle.

Figure 5.24 shows the normalized array factor of a linear broadside [5] array of 6 elements for different element spacing. When the spacing is equal or greater than λ, another main lobes start to appear in the pattern. Such undesired lobes are called grating lobes.

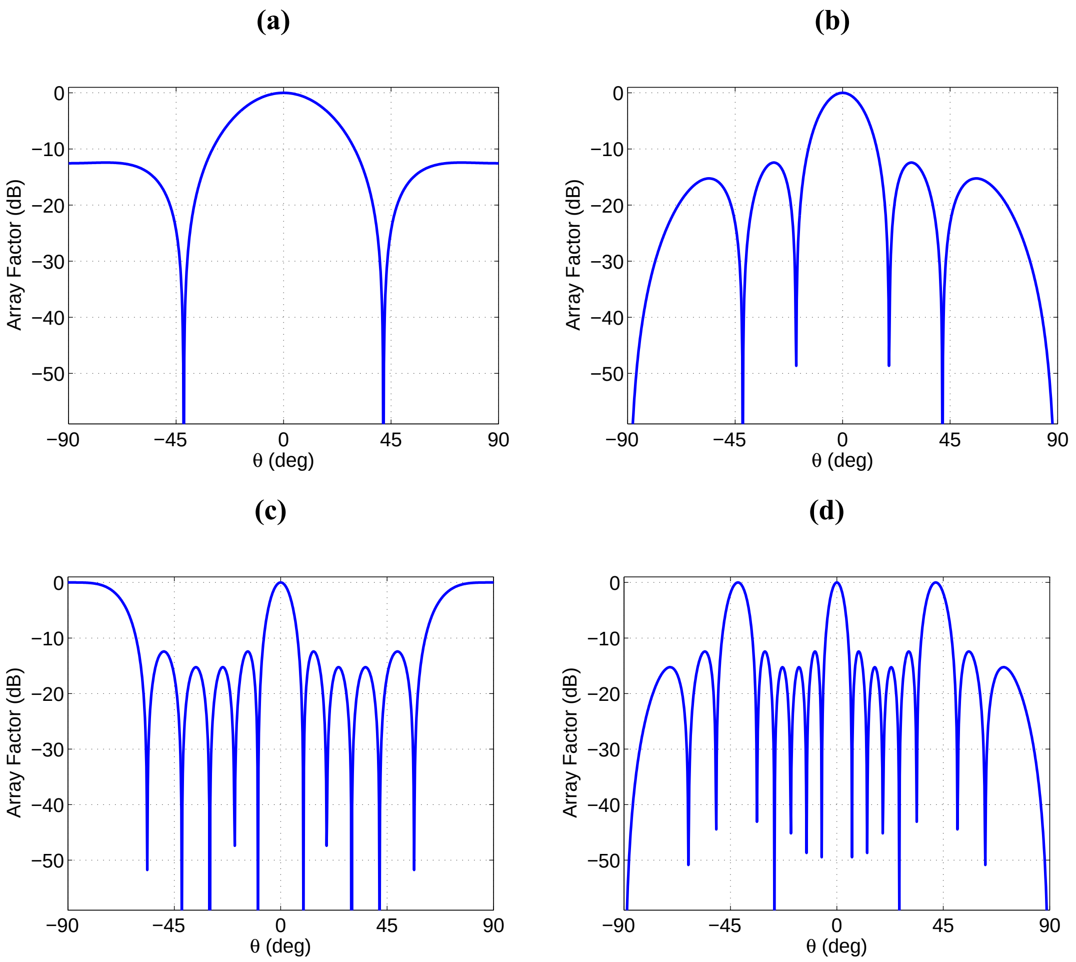

Figure 5.24 – Normalized array factor of linear broadside array of 6 elements for different element spacing d. (a) $d = 0.25\lambda$. (b) $d = 0.5\lambda$. (c) $d = \lambda$. (d) $d = 1.5\lambda$. For $d \geq \lambda$, grating lobes start to appear.

Therefore, to avoid grating lobes for a broadside array, the necessary condition is that the element spacing should be less than one wavelength.

---

[5] Broadside means that the main beam is directed normal to the array.

5.6 Antenna Array Design and Simulation

In this section, we present the design and simulation of the proposed dual-polarized multi-frequency pixel that is candidate for use in multi-pixel focal planes. The pixel itself consists of an antenna array. We are looking for a design that provides co-located dual-polarization detection at both 75 GHz and 105 GHz. The cross polarization level should be below -20 dB. Two architectures are proposed: the rectangular and the triangular lattice array. The simulation of the arrays was done in CST, since it has the ability to excite all the antenna elements simultaneously. This saves a lot of time.

5.6.1 Required Beam Width and Array Size

As mentioned before, the motive behind using an antenna array is to obtain a narrow beam that can be matched to telescope optics. Figure 5.25 shows a simple model of a telescope lens having a diameter D and a focal length f. The antenna array is mounted in the focal plane of the lens. The telescope f-number is defined as the ratio between the focal length f and the diameter D. In our case, the f-number is 2.5, which corresponds to a beam width of $2 \times tan^{-1}\frac{1}{2\times \text{f-number}} = 22.5°$.

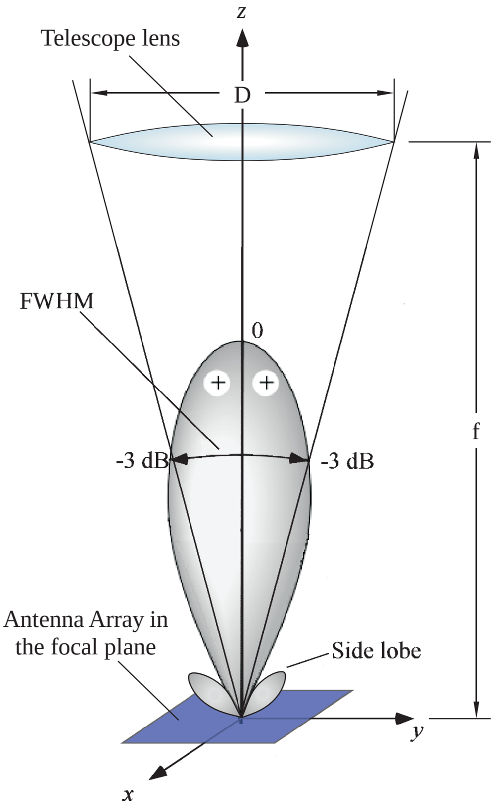

Figure 5.25 – Matching the beam to the telescope optics. The telescope f-number is defined as the ratio between the focal length f and the diameter D.

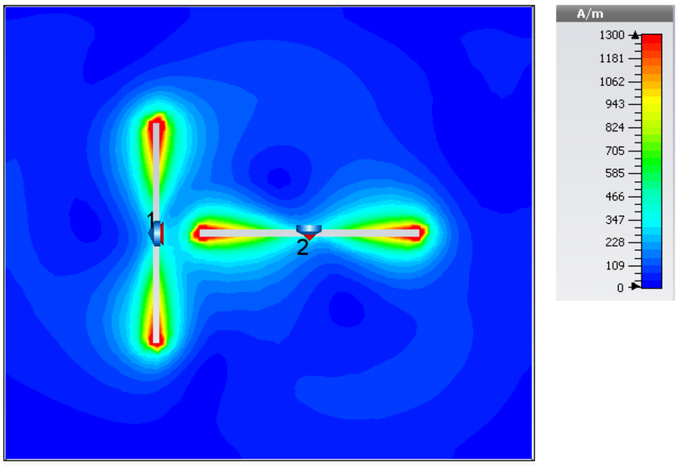

Figure 5.26 – Current distribution of the 75 GHz perpendicular slots in the unit cell. The distance between the slots is chosen to allow enough room for the current around the slots.

5.6.2 Rectangular Lattice Array

Figure 5.27a shows the unit cell of the array and its dimensions. It consists of four slots, two of which operate at 75 GHz (one for the horizontal polarization and the other for the vertical polarization). The other two operate at 105 GHz and also captures both polarizations, (see section 5.4 for the design of the slots themselves). It is expected that the perpendicular slots (slot 1 and slot 2) will be weakly coupled because the pattern of one slot exhibits a null in the direction of the other slot (see Figure 5.7 for the radiation pattern of single slot). The distance between those two slots is chosen to allow enough room for the current around the slots as shown in Figure 5.26.

Similarly, the coupling between the perpendicular 105 GHz slots (slot 3 and slot 4) is very small. Intuitively, it is expected that the parallel slots will couple strongly because they are illuminated by pattern maxima.

To make sure that grating lobes are not excited, the period p of the array is chosen such that $p < \lambda_{min}$, where λ_{min} is the shortest wavelength in medium surrounding the slot (see Equation 5.4.1.1) corresponding to the highest operating frequency in the passband.

Figure 5.27b shows a 4x4 rectangular array constructed from this unit cell. The required beam width (see subsection 5.6.1) was found to correspond to an array of size 8x8. The complete 8x8-cell array as modeled in CST is shown in Figure 5.27c. Figure 5.28 shows the simulation results for the rectangular array. The beam width is 23° and the cross-polarization level is -40 dB.

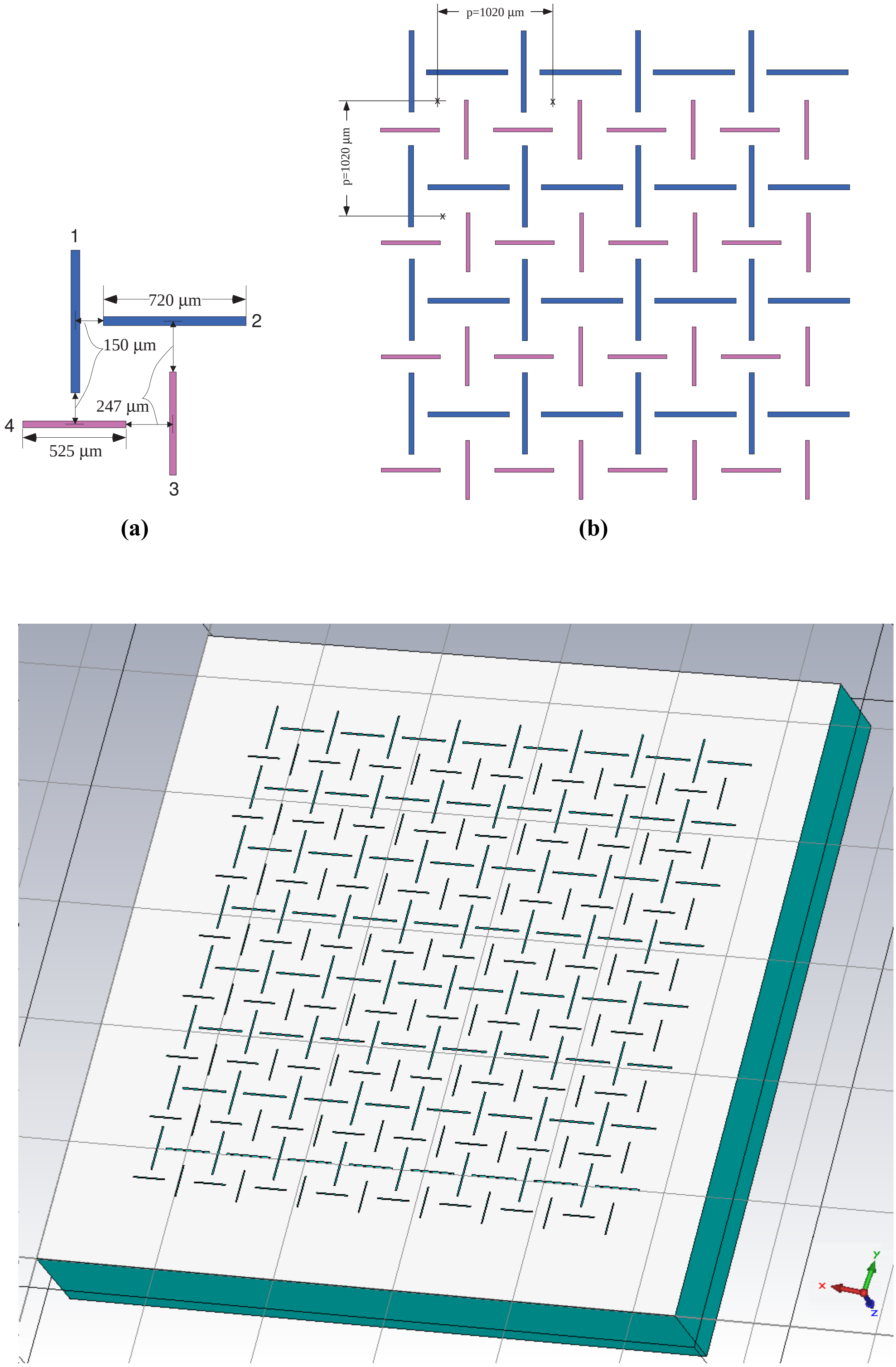

(a) **(b)**

(c)

Figure 5.27 – Dual polarized dual frequency rectangular antenna array of slot antennas. (a) The unit cell. (b) A 4x4 array for concept demonstration. (c) The complete 8x8 array model in CST MWS simulation package.

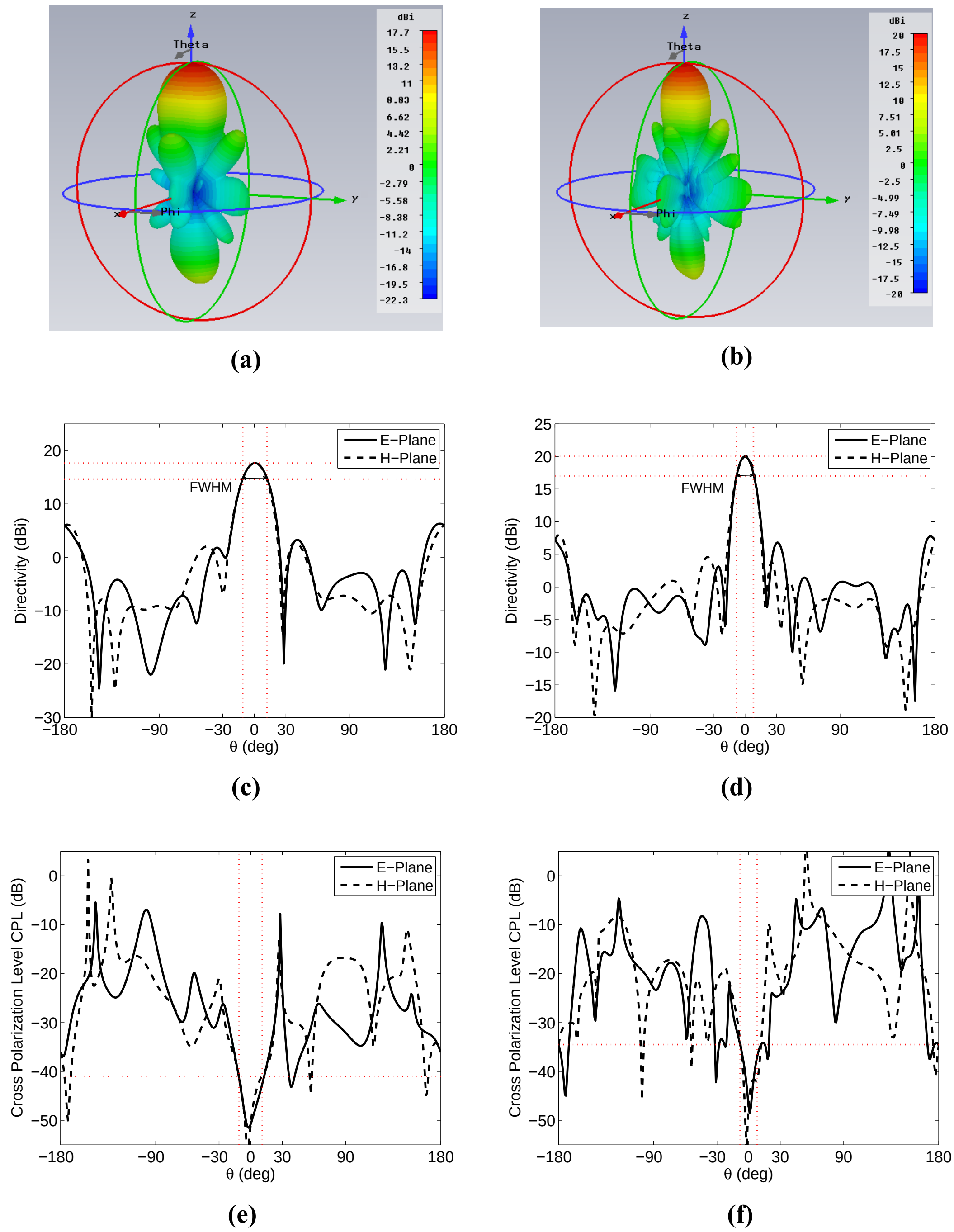

Figure 5.28 – Simulation results for the rectangular array. (a) and (b) 3D beam patterns for 75 GHz and 105 GHz respectively. (c) and (d) Beam patterns in both E and H planes for 75 GHz and 105 GHz respectively. (e) and (f) Cross polarization levels in both E and H planes for 75 GHz and 105 GHz respectively.

The array radiates nearly in one direction because of the high dielectric constant of the substrate. The back lobe is quiet small because the substrate has thickness of quarter wavelength at both frequencies.

5.6.3 Triangular Lattice Array

The unit cell of the array is shown in Figure 5.29a along with the dimensions. The array has a triangular lattice. Triangular grids have several advantages. Firstly, it provide an efficient spatial sampling of the field since the array is more uniformly illuminated. Secondly, it reduce coupling between elements, especially between parallel slots. Thirdly, it allows larger element spacing for nonexistence of a grating lobe: for a square grid array, the element spacing should be less than λ to avoid grating lobes, however, for a triangular lattice, the element spacing should be less than $\lambda/\sin\gamma$ (see Figure 5.29b). Here $\gamma \approx 60°$.

In order to form a triangular lattice, the elements in the second row (element 3 and element 4) have to be shifted from the original square lattice position. Figure 5.30 shows the simulation results of this array.

5.6.4 Performance Comparison

Table 5.1 shows a comparison between the two arrays at both frequencies.

Table 5.1 – Performance comparison of the 8x8 rectangular and triangular arrays.

	Rectangular array		**Triangular array**	
	75 GHz	105 GHz	75 GHz	105 GHz
FWHM (degree)	25	17.5	25	15
Side lobe level (dB)	-14.5	-14.7	-12	-13.7
Back lobe level (dB)	-11.5	-12	-11	-10.5
Cross-polarization level (dB)	-40	-35	-23	-13

It is noted that the triangular array have a highr level of cross polarization. This could be understood by viewing the current distribution of both the arrays. Figure 5.31a shows the current distribution of the rectangular array when the 75 GHz slots are excited. The horizontal slots nearly do not couple to the vertical ones, which gives high polarization purity. On the other hand, the horizontal slots of the triangular array couple to the vertical ones, as shown in Figure 5.31b, deteriorating the cross polarization.

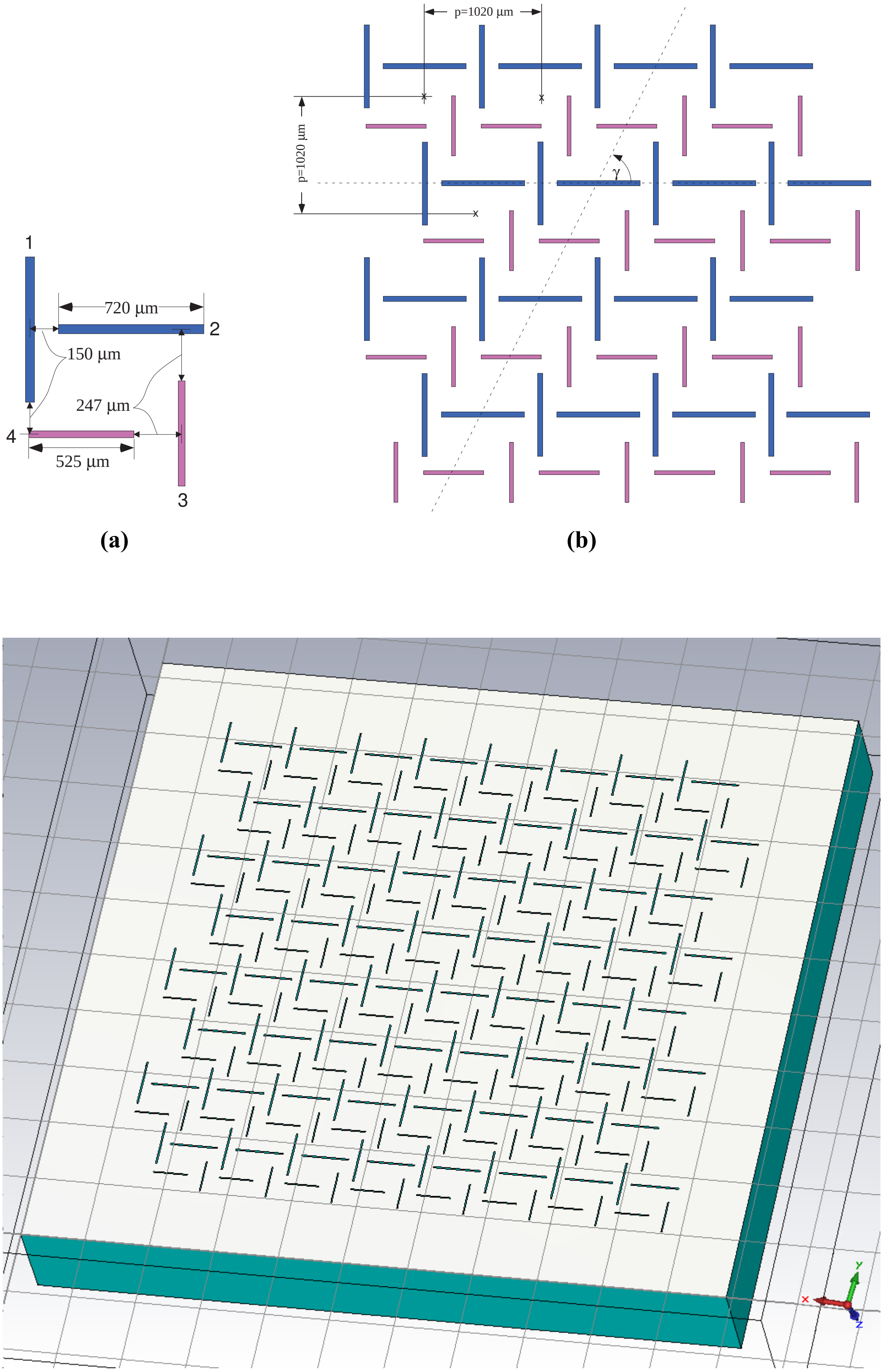

(a) (b)

(c)

Figure 5.29 – Dual polarized dual frequency triangular antenna array of slot antennas. (a) The unit cell. (b) A 4x4 array for concept demonstration. (c) The complete 8x8 array model in CST MWS simulation package.

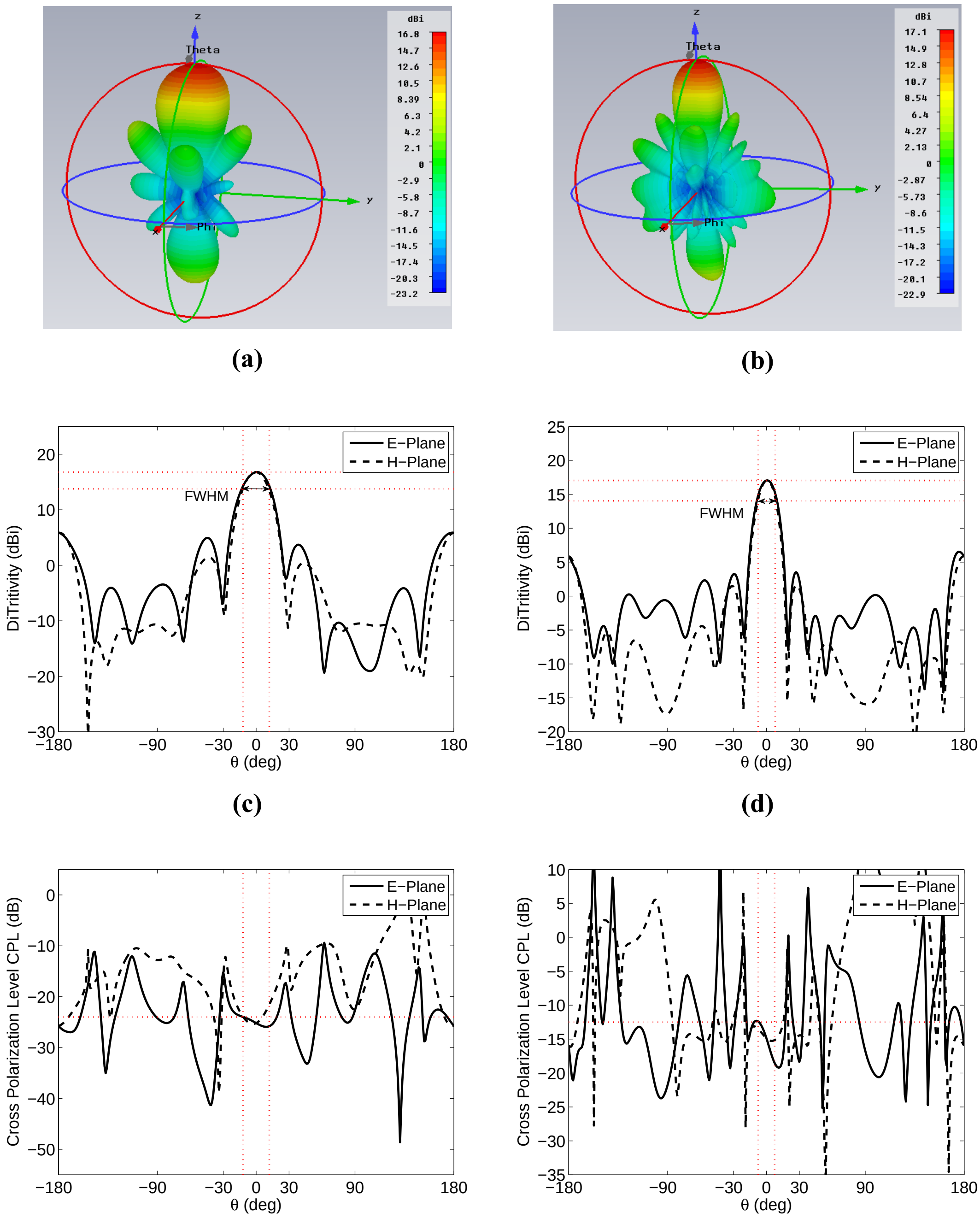

(a) (b)

(c) (d)

(e) (f)

Figure 5.30 – Simulation results for the triangular array. (a) and (b) 3D beam patterns for 75 GHz and 105 GHz respectively. (c) and (d) Beam patterns in both E and H planes for 75 GHz and 105 GHz respectively. (e) and (f) Cross polarization levels in both E and H planes for 75 GHz and 105 GHz respectively.

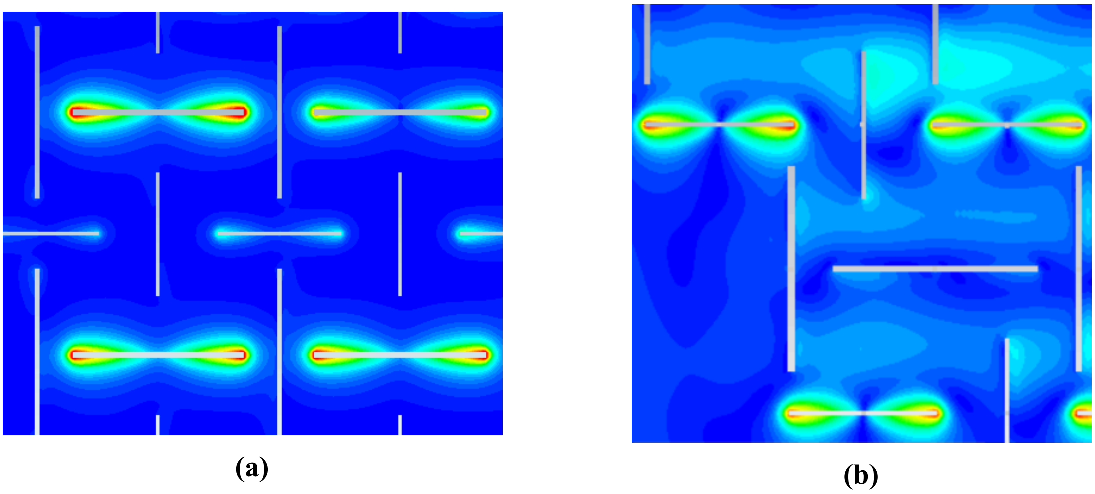

Figure 5.31 – Current distribution of the arrays. (a) Current distribution of the rectangular array, only the horizontal 75 GHz slots are excited. (b) Current distribution of the triangular array, only the horizontal 75 GHz slots are excited.

5.7 Feed Network

To sum all slots in phase to form the beam, a summing network of niobium microstrip lines is used, as shown in Figure 5.32. This kind of feeding is known as corporate feeding, where the network divides into two branches, then each branch divides, and so on. This way, the distance from the detector to each antenna element is the same and slots are summed in phase. Since we have two independent polarization, we have also two sets of networks for each polarization. At the end of each network, the two frequencies are split and detected by the detector.

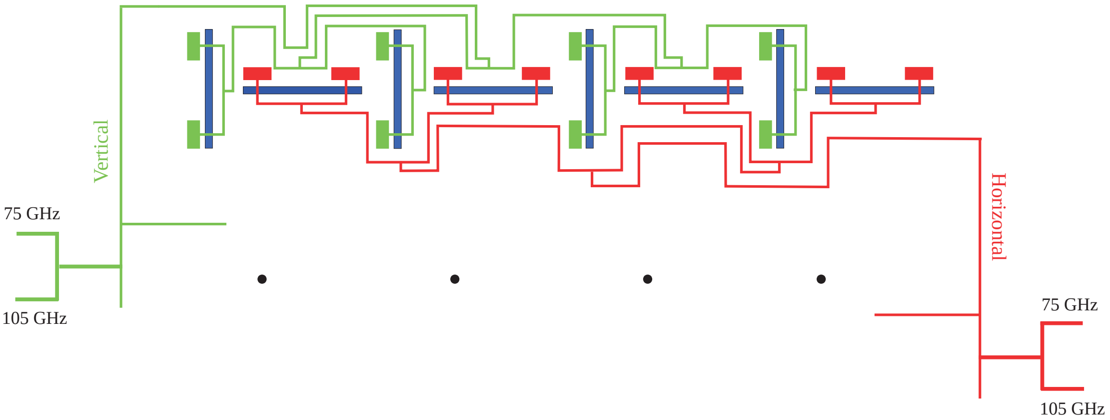

Figure 5.32 – The summing network that collects the signal from the slot in phase. Shown only is the first row of a 4x4 rectangular array. Two networks separate the two polarizations. Each network carries two frequencies that are separated at the end by the internal filtering feature of the detector.

The full network has not been designed yet, however, in this section we address some issues that will help in the design of the complete network. Namely, the issues of microstrip bends.

5.7.1 Microstrip Bends

The summing network has a lot of bends along the microstrip lines. Three problems are associated with the right angle bend (Figure 5.33a). Firstly, the bend introduces a discontinuity leading to a parasitic capacitance due to the increased area of the conductor at the corner of the bend. This in turn incurs reflection. Secondly, electromagnetic energy is radiated into the surrounding from right angle bends since the electric field lines can bulge at the bend. And finally, when the current goes around the bend, most of the current flows on the inside corner, which leads to changing the effective length of the transmission line, skewing the circuit from the intended performance.

The effect of the bend can be mitigated by by making a smooth “curved ” bend as that shown in Figure 5.33b. It was shown that if the right angel bend is replaced by a curve whose radius is at least 3 times the width of the microstrip, the microstrip line does not experience a change in the characteristic impedance [33]. Figure 5.33c shows the simulated reflection coefficient for both right hand bend and curved bend. The simulation was carried out using Sonnet em package with two ports at the two ends of the line.

The curved bend is less lossy. For high performance, the microstrip network should be designed such that it deliver the maximum power at the frequency of operation. Given that there are many of such bends in the network, a curved bend is expected to minimize the loss significantly.

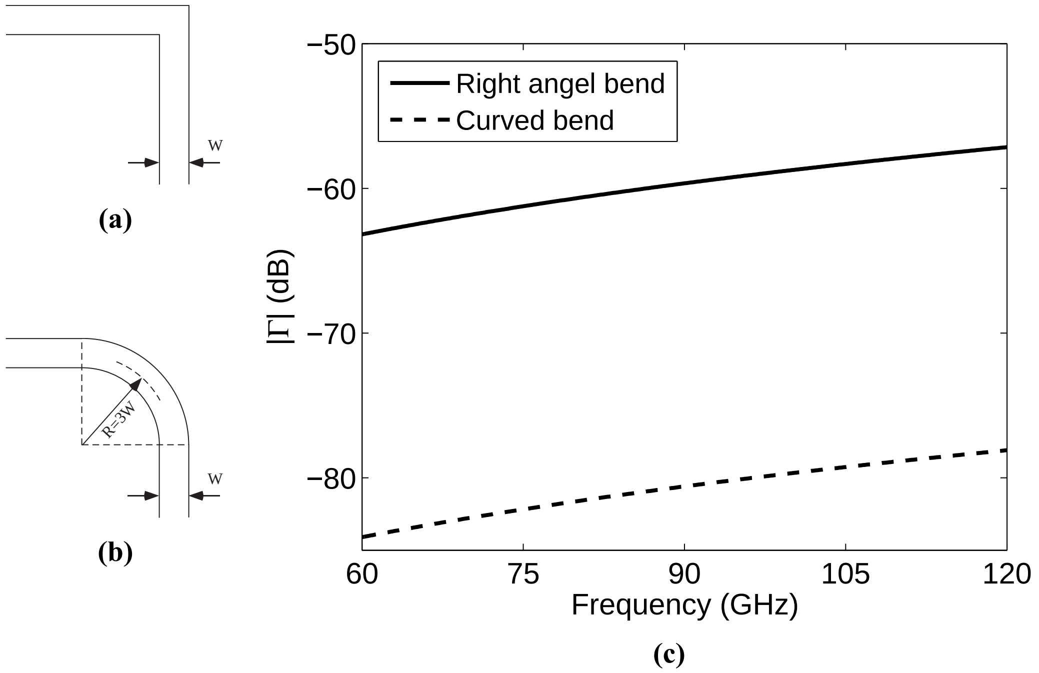

Figure 5.33 – Microstrip bends. (a) Right angel bend. (b) Curved bend with bend radius equal three times the line width. (c) Reflection coefficient of both bends simulated using Sonnet *em* package.

This page intentionally contains only this sentence.

Chapter 6

Conclusions and Future Work

We argued in Chapter 1 that the detection of CMB B-mode will open new venues in science. The detection requires unprecedented levels of sensitivity and polarization separation. The Cold-Electron Bolometer (CEB) is a potential candidate for future CMB missions and competes directly with current technologies. As shown through the device modeling presented in Chapter 4, it has excellent performance in terms of the Noise Equivalent Power (NEP) and sensitivity. To achieve high polarization purity for B-mode detection and multi-frequency operation needed for galactic foreground removal, we proposed a pixel structure consisting of a phased array of narrow perpendicular slots operating at two different frequencies and two orthogonal polarizations. The simulation results shows that the array has an excellent performance in terms of cross polarization and beam width required for coupling the antenna to the telescope optics. This pixel structure could be a candidate for future European Space Agency (ESA) multi-pixel system for B-mode detection.

6.1 Future Work

6.1.1 Feeding Network

The most important step in future work of this system is the design of the microstrip feeding network. The design has many challenges on both design and fabrication levels. On design level, the microstrip line (MSL) width has to be maintained at an acceptable value. Each T-connection means that the MSL at its input would be twice wider to achieve twice lower impedance for matching as shown in Figure 6.1. This means that if the narrowest line is 1 μm wide, the widest one that is in contact with the detector at the end of the network will be $\sim$ 128 μm wide. To avoid this difficulty and keep nearly the same width and impedance, tapering the line between different T-junctions is usually used.

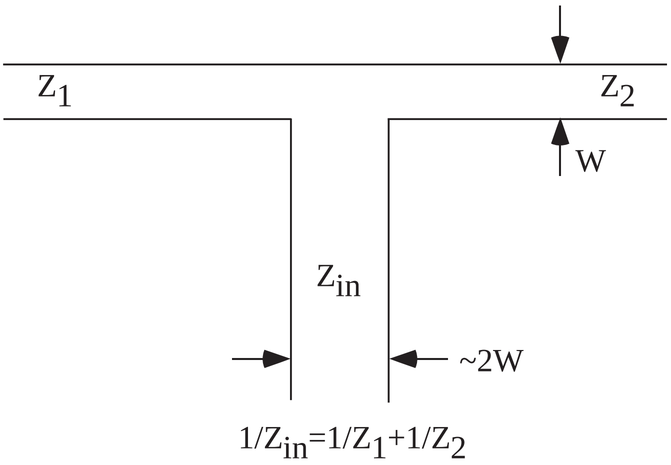

Figure 6.1 – The T-junction used in signal distribution. The main line is nearly twice wider than the branch lines.

Another problem is that the lines carrying different polarizations run close to each other. Therefore, the coupling between them has to be studied carefully.

On the fabrication level, roughness in the dielectric (SiO_2) surface and non-uniformity in the microstrip thickness and width could give rise to variation in phase velocity of the signal carried by the lines. This will cause a phase difference between the signals arriving at the input ports of the antennas, causing the main beam to squint.

6.1.2 Increasing the Number of Frequency Bands

We have shown dual frequency operation (75 GHz and 105 GHz). However, it is possible to increase the number of frequency bands up to four bands using the same structure by making each slot operate at two adjacent frequencies. It was shown in Chapter 5 that the slot has two resonances. Matching the slot in somewhere between those two resonances gives a wideband that can accommodate two frequency bands per slot.

6.1.3 Side lobe Reduction

In the current design all the antenna elements are supposed to be excited equally by the microstrip network. It is possible to lower the side lobe level by non-uniform excitation of the slots. The side lobes could be decreased by about -5 dB when using Gaussian distribution of excitation by controlling the design of the T-junctions power dividers to achieve this excitation distribution.

Appendix A

Mesurement Setup

The device IV characteristics were tested in a He^3 pulse tube cryostat at a bath temperature of 280 mK. The measurement setup is shown in Figure A.1. The device was measured in current biased mode. A two inch wafer coated with a resistive layer of NiC_2 was used as a black body source. When DC current is injected in this layer, power is radiated. This power is coupled to the device through a horn antenna. A thermistor is used to measure the temperature of the black body. A membrane made of Zitex is used to filter out the infrared and allow only far infrared to pass through. Bakelite is used to isolate the black body radiator from the cold metal body of the horn.

Figure A.2 shows the cryostat used in measurements.

To measure the normal state resistance of NIS junction,R_n, the sample is heated.

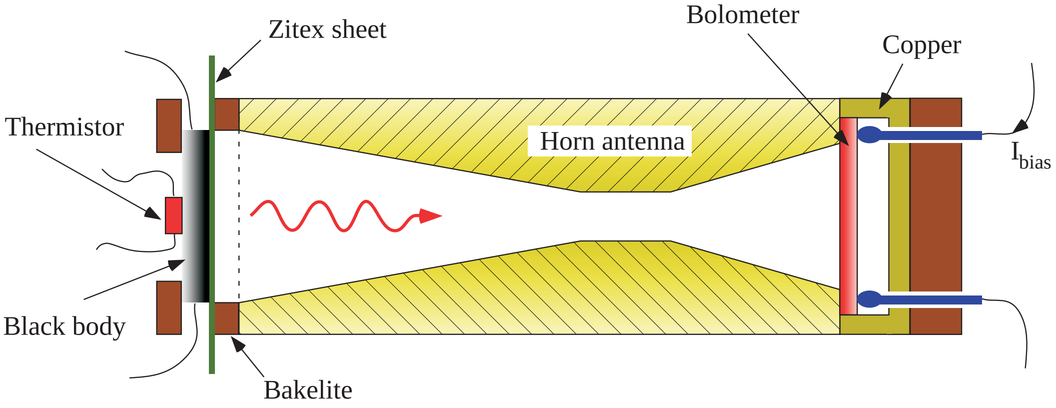

Figure A.1 – The measurement setup for the bolometer IV curve. The black body is heated to illuminate the detector by small amount of power.

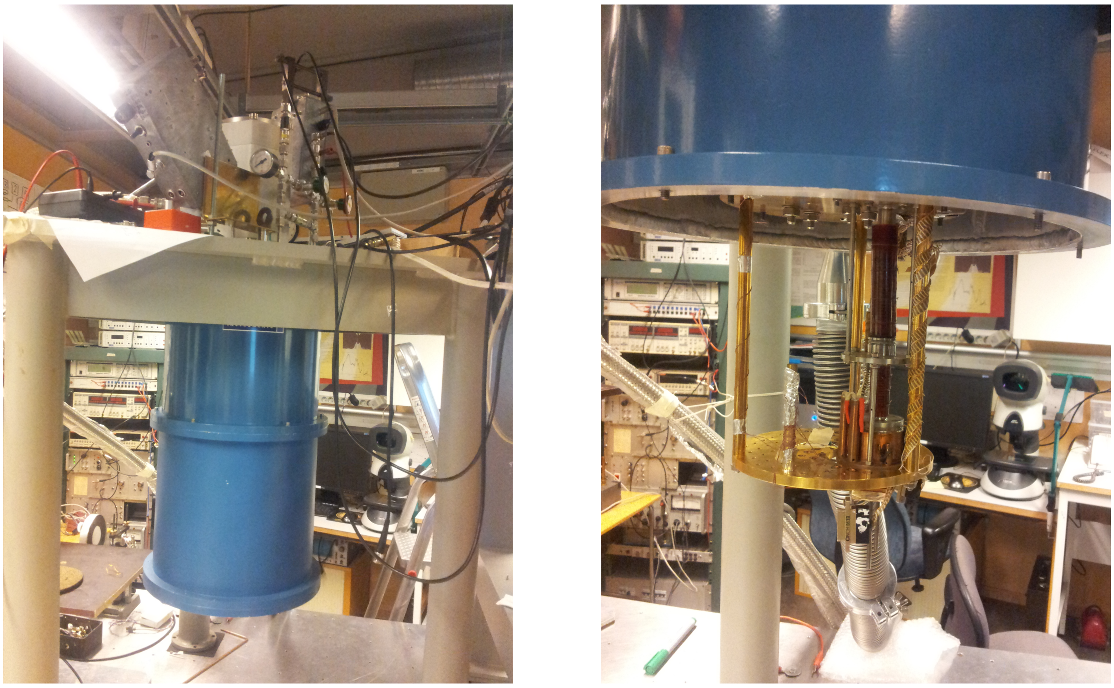

(a)

(b)

Figure A.2 – The pulse tube cryostat used for measuring bolometer IV curve at 280 mK.

Appendix B

MATLAB Routines

B.1 Solving Heat balance Equations

```
%Physics Constants
e=1.602e-19;
KB=8.6173324e-5;  %Boltzmann Constant in eV/K

%Fitting Parameters
gam=0.006;   %gamma, Dynes smearing parameter
Beta=0.15;   %fraction of returning power
Pbg = 0.2;   %Incident power in pW, for all the bolometers
VolS = 2;    %Superconductor volume in um^3

%Measured and Experimental Parameters
Tc=1.62; %Superconductor transition temperature in K
Delta0=1.764*KB*Tc; %Gap at zero temperature, in eV
DeltaN=1; %Delta0 normalized
VolN = 0.02; %The volume of the normal metal electrode in um^3
ZN = 1; ZS = 0.3; %Sigma for normal and supercon. in nW/K^5/um^3
Tp = 0.28; %Phonon bath temp in K
Rabs = 225/2; %Absorber resistance Ohm. The absorber has 2 strips in
    parallel
Ib = 1.4; %Biasing current for electron cooling in nA
M=12;   %12 bolometers in series
MP=1;  %in parallel

%Dependent parameters
KBN=KB/Delta0; %KB Normalized to Delta0
Pbg = Pbg/M/MP; %Incident power per 1 bolometer (pW)
R1bol = 68e3/M*MP; %Measured resistance per one bolo (2 NIS +
    absorber)
Rn=(R1bol-Rabs)/2; % Normal resistance per one NIS
```

```

% Functions
DeltaT = @(Ts) sqrt(cos((pi/2)*(Ts/Tc)));   %Temp. dependence of normalized Delta
DOSSmearT= @(E,gam,Ts) abs(real((E-1i*gam)./(sqrt((E-1i*gam).^2-DeltaT(Ts).^2)))); %Normalized DOS with Dynes smearing and temp. dependence

integrandi=@(E,V,Tn,gam,Ts) DOSSmearT(E,gam,Ts).*((1./(1+exp((E-V)./(KBN*Tn))))-(1./(1+exp((E)./(KBN*Ts))))); %Current integrand
I= @(V,Tn,gam,Ts) Delta0/Rn*quadgk(@(E) integrandi(E,V,Tn,gam,Ts),-Inf,Inf); %Current, in A

integrandpcool=@(E,V,Tn,gam,Ts) DOSSmearT(E,gam,Ts).*(E-V).*((1./(1+exp((E-V)./(KBN*Tn))))-(1./(1+exp((E)./(KBN*Ts))))); %Pcool integrand
Pcool=@(V,Tn,gam,Ts) 1e12*Delta0^2/Rn*quadgk(@(E) integrandpcool(E,V,Tn,gam,Ts),-Inf,Inf); %Cooling power, in pW

integrandps=@(E,V,Tn,gam,Ts) DOSSmearT(E,gam,Ts).*E.*((1./(1+exp((E-V)./(KBN*Tn))))-(1./(1+exp((E)./(KBN*Ts))))); %Ps integrand
PS=@(V,Tn,gam,Ts) 1e12*Delta0^2/Rn*quadgk(@(E) integrandps(E,V,Tn,gam,Ts),-Inf,Inf); %Power deposited in SC, in pW

Pabs= @(V,Tn,gam,Ts) 1e12*Rabs*I(V,Tn,gam,Ts).^2; %Ohmic power in absorber, in pW

Pepn=@(Tn) 1e3*ZN*VolN*(Tn.^5-Tp^5);  %Electron-phonon power in normal metal, in pW

Peps=@(Ts,VolS) 1e3*(ZS*VolS*(Ts.^5-Tp^5).*exp(-DeltaT(Ts)/(KBN*Ts))); %Electron-phonon power in SC, in pW

NHBE=@(V,Tn,gam,Ts,Beta,Pbg) (Pepn(Tn)+2*Pcool(V,Tn,gam,Ts)-Pabs(V,Tn,gam,Ts)-2*Beta*PS(V,Tn,gam,Ts)-Pbg/M/MP); %Heat balance eqution in normal metal

SHBE=@(V,Tn,gam,Ts,Beta,VolS) (Peps(Ts,VolS)-(1-Beta).*PS(V,Tn,gam,Ts)); %Heat balance eqution in SC

% solving the heat balance equations
j=1; %counter for the loop
Vmax=2;
Vmin=-2;
step=0.01;

```

```
TeVector=zeros(1,(Vmax-Vmin)/step+1); %electrons temp. vector
TsVector=zeros(1,(Vmax-Vmin)/step+1); %quasiparticles temp. vector
VVector=zeros(1,(Vmax-Vmin)/step+1); %voltage vector
IVector=zeros(1,(Vmax-Vmin)/step+1); %cuttent vector

for V=Vmin:step:Vmax  %V is normalized in terms of Delta0
     for n=1:4
       Tn = fzero(@(Tn) NHBE(V,Tn,Ts),[0 Tc]); %solve HBE in normal
       Ts = fzero(@(Ts) SHBE(V,Tn,Ts),[0 Tc]); %solve HBE in SC
     end

TeVector(j)=Tn;
TsVector(j)=Ts;
VVector(j)=V;
IVector(j)=I(V,Tn,Ts);
j=j+1;
end
```

B.2 Fitting the Experimental IV Curve

```
%%%%%%%%%%%%%%%%%%%%%%%%%%%%%%%%%%%%%%%%%%%%%%%%%%%%%%%%%%%%
%        Code in B.1 should be included here first          %
%%%%%%%%%%%%%%%%%%%%%%%%%%%%%%%%%%%%%%%%%%%%%%%%%%%%%%%%%%%%

VMin=0; VMax=2; VStep=0.1;
VVector=VMin:VStep:VMax;

%range of fitting parameters around the initial values
gamMin=4.5e-3; gamMax=5.5e-3; gamStep=0.5e-3;
BetaMin=0.15; BetaMax=0.25; BetaStep=0.05;
VolSMin=2; VolSMax=8; VolSStep=1; %in um^3;
PbgMin=0.4; PbgMax=0.7; PbgStep=0.1; %in pW

load('exp_data_L43_41_FullRange.mat') %load the experimental data

%4D matrix having indeces of all the possible combinations, and the
    elements are the least squares
MetricsMatrix=zeros(int16((gamMax-gamMin)/gamStep+1),int16((BetaMax-
    BetaMin)/BetaStep+1),int16((VolSMax-VolSMin)/VolSStep+1),int16((
    PbgMax-PbgMin)/PbgStep+1));

IVector=zeros(1,(VMax-VMin)/VStep+1);

%Search for parameters that gives the best fit
gamindex=1;
```

```
for gam=gamMin:gamStep:gamMax

    Betaindex=1;
    for Beta=BetaMin:BetaStep:BetaMax

            VolSindex=1;
            for VolS=VolSMin:VolSStep:VolSMax

                    Pbgindex=1;
                    for Pbg=PbgMin:PbgStep:PbgMax

                        Ts=0.3;
                        j=1;
                        for V=VMin:VStep:VMax

                            for n=1:3
                            Tn = fzero(@(Tn) NHBE(V,Tn,gam,Ts,Beta,Pbg),[0 Tc]);
                            Ts = fzero(@(Ts) SHBE(V,Tn,gam,Ts,Beta,VolS),[0 Tc]);
                            end

                        IVector(j)=I(V,Tn,gam,Ts);

                        j=j+1;
                        end

                        error=sum(abs(Iinterpolated-IVector)); %error is the accumulated difference between the experimental IV and the fitted one at each bias voltage. The error is evaluated for each combination of the parameters
                        MetricsMatrix(gamindex,Betaindex,VolSindex,Pbgindex)=error;

                    Pbgindex=Pbgindex+1;
                    end

            VolSindex=VolSindex+1;
            end

    Betaindex=Betaindex+1;
    end

gamindex=gamindex+1;
end
```

```
[minVal,MinIndex] = min(MetricsMatrix(:));
[I,J,K,L] = ind2sub(size(MetricsMatrix),MinIndex);

%print the optimun values
gamma=gamMin+(I-1)*gamStep
Beta=BetaMin+(J-1)*BetaStep
VolS=VolSMin+(K-1)*VolSStep
Pbg=PbgMin+(L-1)*PbgStep
```

B.3 Figures of Merit

```
%%%%%%%%%%%%%%%%%%%%%%%%%%%%%%%%%%%%%%%%%%%%%%%%%%%%%%%%%%%
%       Code in B.1 should be included here first         %
%%%%%%%%%%%%%%%%%%%%%%%%%%%%%%%%%%%%%%%%%%%%%%%%%%%%%%%%%%%

%% responsivity functions
%dIdT
integranddIdT=@(E,V,Tn) DOSNoSmear(E).*(1./(1+exp((E-V)./(KBN*Tn)))).^2.*((E-V)./(KBN*Tn.^2)).*exp((E-V)./(KBN*Tn));
dIdT=@(V,Tn) Delta0/Rn*quadgk(@(E) integranddIdT(E,V,Tn),-20,20); %in A/K

%dIdV
integranddIdV=@(E,V,Tn) DOSNoSmear(E).*(1./(1+exp((E-V)./(KBN*Tn)))).^2.*(1./(KBN*Tn)).*exp((E-V)./(KBN*Tn));
dIdV=@(V,Tn) 1/Rn*quadgk(@(E) integranddIdV(E,V,Tn),-20,20); %in A/V

%dPdT
integranddPdT=@(E,V,Tn) DOSNoSmear(E).*(E-V).*(1./(1+exp((E-V)./(KBN*Tn)))).^2.*((E-V)./(KBN*Tn.^2)).*exp((E-V)./(KBN*Tn));
dPdT=@(V,Tn) Delta0^2/Rn*quadgk(@(E) integranddPdT(E,V,Tn),-20,20); % in W/K

%dPdV
integranddPdV=@(E,V,Tn) DOSNoSmear(E).*((E-V).*(1./(1+exp((E-V)./(KBN*Tn)))).^2.*(1./(KBN*Tn)).*exp((E-V)./(KBN*Tn))-((1./(1+exp((E-V)./(KBN*Tn))))-(1./(1+exp((E)./(KBN*Ts))))));
dPdV=@(V,Tn) Delta0/Rn*quadgk(@(E) integranddPdV(E,V,Tn),-20,20); %in W/V

Si=@(V,Tn) 1e-3*(dIdT(V,Tn))./(1e-9*5*ZN*VolN*Tn.^4+dPdT(V,Tn)); % voltage biased mode responsivity in nA/pW

```

```
Sv=@(V,Tn) 1e-6*((-1*dIdT(V,Tn))./(dIdV(V,Tn)))./(1e-9*5*ZN*VolN*Tn.^4+dPdT(V,Tn)-(dIdT(V,Tn)./dIdV(V,Tn)).*dPdV(V,Tn)); %current biased mode responsivity in uV/pW


%% NEP functions

integrandISD=@(E,V,Tn) DOSNoSmear(E).*((1./(1+exp((E-V)./(KBN*Tn))))+(1./(1+exp((E)./(KBN*Ts))))-2*(1./(1+exp((E-V)./(KBN*Tn)))).*(1./(1+exp((E)./(KBN*Ts)))));
ISD=@(V,Tn) 2*e*Delta0/Rn*quadgk(@(E) integrandISD(E,V,Tn),-Inf,Inf);

integrandPSD=@(E,V,Tn) DOSNoSmear(E).*(E-V).^2.*((1./(1+exp((E-V)./(KBN*Tn))))+(1./(1+exp((E)./(KBN*Ts))))-2*(1./(1+exp((E-V)./(KBN*Tn)))).*(1./(1+exp((E)./(KBN*Ts)))));
PSD=@(V,Tn) 2*e*Delta0^3/Rn*quadgk(@(E) integrandPSD(E,V,Tn),-Inf,Inf);

integrandCorrSD=@(E,V,Tn) DOSNoSmear(E).*(E-V).*((1./(1+exp((E-V)./(KBN*Tn))))+(1./(1+exp((E)./(KBN*Ts))))-2*(1./(1+exp((E-V)./(KBN*Tn)))).*(1./(1+exp((E)./(KBN*Ts)))));
CorrSD=@(V,Tn) 2*e*Delta0^2/Rn*quadgk(@(E) integrandCorrSD(E,V,Tn),-Inf,Inf);

NEP2NISv=@(V,Tn) PSD(V,Tn)-2*(CorrSD(V,Tn))./(1e3*Si(V,Tn))+(ISD(V,Tn))./(1e6*Si(V,Tn).^2); %NEP_NIS^2 in voltage biased mode in W^2/Hz
NEP2epv=@(Tn) 1e-9*10*KBSI*ZN*VolN*(Tn.^6-Tp^6);
NEP2Ampv=@(V,Tn) (0.05e-12./(1e3*Si(V,Tn))).^2; %Amplifier NEP in voltage biased mode

NEP2NISi=@(V,Tn) PSD(V,Tn)-2*(CorrSD(V,Tn))./(dIdV(V,Tn).*1e6*Sv(V,Tn))+(ISD(V,Tn))./((dIdV(V,Tn).*1e6*Sv(V,Tn)).^2); %NEP_NIS^2 in current biased mode in W^2/Hz
NEP2epi=@(Tn) 1e-9*10*KBSI*ZN*VolN*(Tn.^6-Tp^6);
NEP2Ampi=@(V,Tn) (3e-9./(1e6*Sv(V,Tn))).^2;


%% Time constant functions

gamma=9.77e-17; %J/um^3K^2
tau_inv_vbias=@(V,Tn) (1./(gamma*Tn*VolN)).*(1e-9*5*ZN*VolN*Tn.^4+dPdT(V,Tn));
tau_inv_ibias=@(V,Tn) (1./(gamma*Tn*VolN)).*(1e-9*5*ZN*VolN*Tn.^4+dPdT(V,Tn)-(dIdT(V,Tn)./dIdV(V,Tn)).*dPdV(V,Tn));
```

B.4 Mattis-Bardeen Nb Surface Impedance Calculator

```
global hbar mu0 Delta0 DeltaN KBN vf l Z0 H N prefactor
global d %film thickness to use in SurfImp
global sigN %the normal conductivity of Nb

hbar=1.05457172647e-34;
mu0=1.2566370614e-6; %vacuum permeability
KB=1.3806488e-23/hbar;  %Boltzmann const. normalized in terms of hbar

Tc=9.2;
d=200e-9; %200nm film thickness
sigN=2e7;
Delta0=1.8*KB*Tc; %Delta0 in units of angular frequency, "i.e.
    normalized in terms of hbar"
DeltaN=1; %Normalized in Delta0
KBN=KB/Delta0; %KB Normalized to (hbar*Delta0)

% now energy is normalized with hbar*Delta0, and omega is normalized
    in terms of Delta0.

omegamin=0.1;
omegamax=4;
step=0.05;
omegaVector=zeros(1,int16(omegamax-omegamin)/step+1);
sig1Vector=zeros(1,int16(omegamax-omegamin)/step+1);
sig2Vector=zeros(1,int16(omegamax-omegamin)/step+1);
SurfImpVector=zeros(1,int16(omegamax-omegamin)/step+1);

T=0.5; %500mK

j=1;
for omega=omegamin:step:omegamax

omegaVector(j)=omega;
sig1Vector(j)=sig1(omega,T);
sig2Vector(j)=sig2(omega,T);
SurfImpVector(j)=SurfImp(omega,sig1Vector(j),sig2Vector(j));

j=j+1;
end

%Generating HFSS tab files for Zs
%HFSS takes two separate files for real and imaginary
freqVector=omegaVector'*Delta0/(2*pi);
```

```
RVector=(real(SurfImpVector))';
XVector=(imag(SurfImpVector))';
RvsfreqVector=[freqVector,RVector];
XvsfreqVector=[freqVector,XVector];
save Rvsfreq.tab RvsfreqVector -ASCII -tabs
save Xvsfreq.tab XvsfreqVector -ASCII -tabs

%Generating Sonnet CSV comma separated file for Zs
%Sonnet accepts one file with three colums Freq, Real, Imag
csvwrite('ZsXSonnet.csv',XvsfreqVector)

---------------------------------------------------------------------
%A function to calculate sigma1, the real part of the complex conductivity
function [out] = sig1(omega,T)

global hbar Delta0 DeltaN KBN;

%% functiond definitions

Delta1=@(E) sqrt(E.^2-DeltaN^2); %Note that both E and Delta here are  normalized in terms of hbar*Delta0, so multiply by this factor whenever you use Delta1
Delta2=@(E,omega) sqrt((E+omega).^2-DeltaN^2); %Note that both E and Delta here are normalized in terms of hbar*Delta0, so multiply by this factor whenever you use Delta2
g=@(E,omega) (E.^2+DeltaN^2+omega.*E)./(Delta1(E).*Delta2(E,omega));

sig1_kernel1=@(E,omega,T) ((1./(1+exp((E)./(KBN*T))))-(1./(1+exp((E+omega)./(KBN*T))))).*(g(E,omega));
sig1_kernel2=@(E,omega,T) (1-2*(1./(1+exp((E+omega)./(KBN*T))))).*(g(E,omega));
sig1_subgap= @(omega,T) (2./omega)*quadgk(@(E) sig1_kernel1(E,omega,T),DeltaN,Inf);
sig1_abovegap=@(omega,T) (2./omega)*quadgk(@(E) sig1_kernel1(E,omega,T),DeltaN,Inf) + (1./omega)*quadgk(@(E) sig1_kernel2(E,omega,T),DeltaN-omega,DeltaN);

if omega<=2
    out=sig1_subgap(omega,T);
else
    out=-1*sig1_abovegap(omega,T);
end
end

```

```
----------------------------------------------------------------------
%A function to calculate sigma1, the real part of the complex conductivity
function [out] = sig2(omega,T)

global hbar Delta0 DeltaN KBN;

%% functiond definitions

Deltan1=@(E) sqrt(DeltaN^2-E.^2); %Note that both E and Delta here are normalized in terms of hbar*Delta0, so multiply by this factor whenever you use Delta1
Delta2=@(E,omega) sqrt((E+omega).^2-DeltaN^2); %Note that both E and Delta here are normalized in terms of hbar*Delta0, so multiply by this factor whenever you use Delta2
gn=@(E,omega) (E.^2+DeltaN^2+omega.*E)./(Deltan1(E).*Delta2(E,omega));

sig2_kernel=@(E,omega,T) (1-2*(1./(1+exp((E+omega)./(KBN*T))))).*(gn(E,omega));
sig2_subgap= @(omega,T) (1./omega)*quadgk(@(E) sig2_kernel(E,omega,T),DeltaN-omega,DeltaN);
sig2_abovegap= @(omega,T) (1./omega)*quadgk(@(E) sig2_kernel(E,omega,T),-DeltaN,DeltaN);

if omega<=2
    out=sig2_subgap(omega,T);
else
    out=sig2_abovegap(omega,T);
end
end

----------------------------------------------------------------------
%A function to calculate the complex surface impedance Zs
function [Zs] = SurfImp(omega,sig1,sig2)

global hbar Delta0 DeltaN KBN mu0 sigN d;

sig=(real(sig1)-1i*sig2)*sigN;

Zs=sqrt(1i*Delta0*omega*mu0/sig)*coth(sqrt(1i*Delta0*omega*mu0*sig)*d);

%Another equation for Zs. Gives exactly the same result
```

```
%delta=sqrt(2/(mu0*Delta0*omega*sig));
%lambda2=(1+1i)/delta;
%Zs=(lambda2/sig)*coth(lambda2*d);

end
```

Bibliography

[1] P. a. R. Ade, R. W. Aikin, D. Barkats, S. J. Benton, C. a. Bischoff, J. J. Bock, J. a. Brevik, I. Buder, E. Bullock, C. D. Dowell, L. Duband, J. P. Filippini, S. Fliescher, S. R. Golwala, M. Halpern, M. Hasselfield, S. R. Hildebrandt, G. C. Hilton, V. V. Hristov, K. D. Irwin, K. S. Karkare, J. P. Kaufman, B. G. Keating, S. a. Kernasovskiy, J. M. Kovac, C. L. Kuo, E. M. Leitch, M. Lueker, P. Mason, C. B. Netterfield, H. T. Nguyen, R. O'Brient, R. W. Ogburn, A. Orlando, C. Pryke, C. D. Reintsema, S. Richter, R. Schwarz, C. D. Sheehy, Z. K. Staniszewski, R. V. Sudiwala, G. P. Teply, J. E. Tolan, a. D. Turner, a. G. Vieregg, C. L. Wong, and K. W. Yoon. "Detection of B-Mode Polarization at Degree Angular Scales by BICEP2". In: *Physical Review Letters* 112.24 (June 2014), p. 241101.

[2] A. Axelrod, M. Kisliuk, and J. Maoz. "Broadband Microstrip-fed Slot Radiator". In: *Microwave Journal* 32 (1989), 81, 82, 84 (4 ff.)

[3] D. Barkats, C. Bischoff, P. Farese, T. Gaier, J. O. Gundersen, M. M. Hedman, L. Hyatt, J. J. McMahon, D. Samtleben, S. T. Staggs, E. Stefanescu, K. Vanderlinde, and B. Winstein. "Cosmic Microwave Background Polarimetry Using Correlation Receivers with the PIQUE and CAPMAP Experiments". In: *The Astrophysical Journal Supplement Series* 159.1 (July 2005), pp. 1–26.

[4] C. Barnes, M. Limon, L. Page, C. Bennett, S. Bradley, M. Halpern, G. Hinshaw, N. Jarosik, W. Jones, A. Kogut, S. Meyer, O. Motrunich, G. Tucker, D. Wilkinson, and E. Wollack. "The Map Satellite Feed Horns". In: *The Astrophysical Journal Supplement Series* 143 (2002), pp. 567–576.

[5] M. A. Biondi and M. P. Garfunkel. "Millimeter Wave Absorption in Superconducting Aluminum. II. Calculation of the Skin Depth". In: *Physical Review* 116.4 (1959).

[6] C. R. Brewitt-Taylor, D. J. Gunton, and H. D. Rees. "Planar Antennas on a Dielectric Surface". In: *Electronics Letters* 17.20 (1981), pp. 729–731.

[7] D. Chouvaev. "Normal Metal Hot-Electron Microbolometer with Superconducting Andreev Mirrors". PhD thesis. Chalmers University of Technology, 2001.

[8] P.N. Chubov, V.V. Eremenko, and Yu. A. Pilipenko. “Dependence of the Critical Temperature and Energy Gap on the Thickness of Superconducting Aluminum Films”. In: *Journal of Experimental and Theoretical Physics* 28.3 (1969), pp. 189–195.

[9] P. J. B. Clarricoats and A. D. Olver. *Corrugated Horns for Microwave Antennas*. London: IEE Electromagnetic Waves, Series 18, 1984.

[10] B. N. Das and K. K. Joshi. “Impedance of a Radiating Slot in the Ground Plane of a Microstripline”. In: *IEEE Transactions on Antennas and Propagation* AP-30 (1982), pp. 922–926.

[11] R. C. Dynes, V. Narayanamurti, and J. P. Garno. “Direct Measurement of Quasiparticle-Lifetime Broadening in a Strong-Coupled Superconductor”. In: *Physical Review Letters* 41.21 (1978), pp. 1509–1512.

[12] E. M. Leitch, J. M. Kovac, C. Pryke, J. E. Carlstrom, N. W. Halverson, W. L. Holzapfel, M. Dragovan, B. Reddall, and E. S. Sandberg. “Measurement of Polarization with the Degree Angular Scale Interferometer”. In: *Nature* 420 (2002), pp. 763–771.

[13] R. S. Elliott. *Antenna Theory and Design*. John Wiley & Sons, 2003.

[14] P. a. Fisher, J. N. Ullom, and M. Nahum. “High-power On-chip Microrefrigerator Based on a Normal-metal / Insulator / Superconductor Tunnel Junction”. In: *Applied Physics Letters* 74.18 (1999), pp. 2705–2707.

[15] I. Giaever. “Energy Gap in Superconductors Measured by Electron Tunneling”. In: *Physical Review Letters* 5.4 (1960), pp. 147–148.

[16] D. Golubev and L. Kuzmin. “Nonequilibrium Theory of a Hot-Electron Bolometer with Normal Metal-Insulator-Superconductor Tunnel Junction”. In: *Journal of Applied Physics* 89 (2001), pp. 6464–6472.

[17] S.R. Golwala, J. Jochum, and B. Sadoulet. “Noise considerations in Low Resistance NIS Tunnel Junctions”. In: *7th International Workshop on Low Temperature Detectors*. 1997, pp. 64–65.

[18] D. Hanson, S. Hoover, A. Crites, P. a. R. Ade, K. a. Aird, J. E. Austermann, J. a. Beall, a. N. Bender, B. a. Benson, L. E. Bleem, J. J. Bock, J. E. Carlstrom, C. L. Chang, H. C. Chiang, H-M. Cho, A. Conley, T. M. Crawford, T. de Haan, M. a. Dobbs, W. Everett, J. Gallicchio, J. Gao, E. M. George, N. W. Halverson, N. Harrington, J. W. Henning, G. C. Hilton, G. P. Holder, W. L. Holzapfel, J. D. Hrubes, N. Huang, J. Hubmayr, K. D. Irwin, R. Keisler, L. Knox, a. T. Lee, E. Leitch, D. Li, C. Liang, D. Luong-Van, G. Marsden, J. J. McMahon, J. Mehl, S. S. Meyer,

L. Mocanu, T. E. Montroy, T. Natoli, J. P. Nibarger, V. Novosad, S. Padin, C. Pryke, C. L. Reichardt, J. E. Ruhl, B. R. Saliwanchik, J. T. Sayre, K. K. Schaffer, B. Schulz, G. Smecher, a. a. Stark, K. T. Story, C. Tucker, K. Vanderlinde, J. D. Vieira, M. P. Viero, G. Wang, V. Yefremenko, O. Zahn, and M. Zemcov. "Detection of B-Mode Polarization in the Cosmic Microwave Background with Data from the South Pole Telescope". In: *Physical Review Letters* 111.14 (Sept. 2013), p. 141301.

[19] J. R. Hinderks, P. Ade, J. Bock, M. Bowden, M. L. Brown, G. Cahill, J. E. Carlstrom, P. G. Castro, S. Church, T. Culverhouse, R. Friedman, K. Ganga, W. K. Gear, S. Gupta, J. Harris, V. Haynes, B. G. Keating, J. Kovac, E. Kirby, a. E. Lange, E. Leitch, O. E. Mallie, S. Melhuish, Y. Memari, A. Murphy, A. Orlando, R. Schwarz, C. O' Sullivan, L. Piccirillo, C. Pryke, N. Rajguru, B. Rusholme, a. N. Taylor, K. L. Thompson, C. Tucker, a. H. Turner, E. Y. S. Wu, and M. Zemcov. "QUaD: A High-Resolution Cosmic Microwave Background Polarimeter". In: *The Astrophysical Journal* 692.2 (Feb. 2009), pp. 1221–1246.

[20] *http://www.ansys.com/*.

[21] *http://www.cst.com/*.

[22] *http://www.sonnetsoftware.com/*.

[23] W. C. Jones, R. S. Bhatia, J. J. Bock, and A. E. Lange. "A Polarization Sensitive Bolometric Detector for Observations of the Cosmic Microwave Background". In: *Proceedings of SPIE 4855, Millimeter and Submillimeter Detectors for Astronomy*. 2003, pp. 227–238.

[24] P. Kildal. *Foundations of Antennas*. 2nd ed. 2014.

[25] J. P. Kim and W. S. Park. "Network Modeling of an Inclined and Off-Center Microstrip-Fed Slot Antenna". In: *IEEE Transactions on Antennas and Propagation* 46.8 (1998).

[26] M. Kominami and D. M. Pozar. "Dipole and Slot Elements and Arrays on Semi-Infinite Substrates". In: *IEEE Transactions on Antennas and Propagation* AP-33.6 (1985), pp. 600–607.

[27] L. Kuzmin. "On the Concept of a Hot-Electron Microbolometer with Capacitive Coupling to the Antenna". In: *Physica B: Condensed Matter* 284-288 (2000), pp. 2129–2130.

[28] L. Kuzmin. "Optimization of the Hot-Electron Bolometer and A Cascade Quasiparticle Amplifier for Space Astronomy". In: *Proceedings of the International Workshop on Superconducting Nano-Electronics Devices*. 2002, pp. 145–154.

[29] L. S. Kuzmin. “A Resonant Cold-Electron Bolometer With a Kinetic Inductance Nanofilter”. In: *IEEE Transactions on Terahertz Science and Technology* 4.3 (2014), pp. 314–320.

[30] J. Lamarre. “Planck Pre-Launch Status: The HFI Instrument, From Specification to Actual Performance”. en. In: *Astronomy and Astrophysics* 520 (Sept. 2010), A9.

[31] J.M. Lamarre, J. L. Puget, M. Piat, P. A. R. Ade, A. Lange, A. Benoit, P. De Bernardis, F. R. Bouchet, J. Bock, F. X. Desert, R. Emry, M. Giard, B. Maffei, A. Murphy, J. P. Torre, R. Bhatia, R. Sudiwala, and V. Yourchenko. “The Planck High Frequency Instrument, a 3rd Generation CMB Experiment and a Full Sky Submillimeter Survey”. In: *Proc. SPIE 4850*. 2002, pp. 730–739.

[32] A. Lee, P. Richards, S. Nam, B. Cabrera, and K. Irwin. “A Superconducting Bolometer with Strong Electrothermal Feedback”. In: *Applied Physics Letters* 69 (1996), pp. 1801–1803.

[33] T. Lee. *Planar Microwave Engineering*. Cambridge University Press, 2004.

[34] MM Leivo, JP Pekola, and DV Averin. “Efficient Peltier Refrigeration by a Pair of Normal Metal/Insulator/Superconductor Junctions”. In: *Applied physics letters* 68.14 (1996), pp. 1996–1998.

[35] A. Ludwig. “The Definition of Cross Polarization”. In: *IEEE Transactions on Antennas and Propagation* 21.1 (1973), pp. 116–119.

[36] R. E. Matick. *Transmission Lines for Digital and Communication Networks*. IEEE Press, 1969.

[37] DC Mattis and J Bardeen. “Theory of the Anomalous Skin Effect in Normal and Superconducting Metals”. In: *Physical Review* 111.2 (1958).

[38] D. G. McDonald. “Novel Superconducting Thermometer for Bolometric Applications”. In: *Applied Physics Letters* 50.12 (1987), pp. 775–777.

[39] P.B Miller. “Surface Impedance of Superconductors”. In: *Physical Review* 118.4 (1960), pp. 928–934.

[40] M. Nahum, TM. Eiles, and JM. Martinis. “Electronic Microrefrigerator Based on a Normal-Insulator-Superconductor Tunnel Junction”. In: *Applied physics letters* 65.24 (1994), pp. 3123–3125.

[41] M. Nahum and J.M. Martinis. “Ultrasensitive Hot-Electron Microbolometer”. In: *Applied Physics Letters* 63.22 (1993), pp. 3075–3077.

[42] G. C. O’Neil. “Improving NIS Tunnel Junction Refrigerators: Modeling, Materials, and Traps”. PhD dissertation. University of Colorado, 2011.

[43] P. M. Echternach, M. R. Thoman, C. M. Gould, and H. M. Bozler. “Electron-Phonon Scattering Rates in Disordered Metallic Films Below 1 K”. In: *Physical Review B* 46.16 (1992), p. 10339.

[44] S. Padin, M. C. Shepherd, J. K. Cartwright, R. G. Keeney, B. S. Mason, T. J. Pearson, a. C. S. Readhead, W. a. Schaal, J. Sievers, P. S. Udomprasert, J. K. Yamasaki, W. L. Holzapfel, J. E. Carlstrom, M. Joy, S. T. Myers, and A. Otarola. “The Cosmic Background Imager”. In: *Publications of the Astronomical Society of the Pacific* 114.791 (Jan. 2002), pp. 83–97.

[45] A. B. Pippard. “An Experimental and Theoretical Study of the Relation Between Magnetic Field and Current in a Superconductor”. In: *Proceedings of the Royal Society* A216 (1953), pp. 547–568.

[46] P. Pöpel. “Surface Impedance and Reflectivity of Superconductors”. In: *Journal of Applied Physics* 66.12 (1989), p. 5950.

[47] D. M. Pozar. “A Reciprocity Method of Analysis for Printed Slot and Slot-Coupled Microstrip Antennas”. In: *IEEE Transactions on Antennas and Propagation* AP-34.12 (1986), pp. 1439–1446.

[48] D. M. Pozar. *Microwave Engineering*. 4th. John Wiley & Sons, 2011.

[49] J. S. Rao and B. N. Das. “Impedance Characteristics of Transverse Slots in the Ground Plane of a Stripline”. In: *Proceedings of the Institution of Electrical Engineers*. Vol. 125. 1978, pp. 29–31.

[50] J. Reitz, F. Milford, and R. Christy. *Foundations of Electromagnetic Theory*. 4th. 2008.

[51] P. Richards. “Bolometric Detectors for Space Astrophysics”. In: *Far-IR, Sub-mm & MM Detector Technology Workshop, held 1-3 April 2002 in Monterey, CA. Organized and Sponsored by NASA/Ames & USRA/SOFIA*. 2002.

[52] P. L. Richards. “Bolometers for Infrared and Millimeter Waves”. In: *Journal of Applied Physics* 76 (1994), pp. 1–36.

[53] M. Roukes, M. Freeman, R. Germain, R. Richardson, and M. Ketchen. “Hot Electrons and Energy Transport in Metals at Millikelvin Temperatures”. In: *Physical Review Letters* 55.4 (1985), pp. 422–425.

[54] D. B. Rutledge, D. P. Neikirk, and D. P. Kasilingam. “Integrated-Circuit Antennas”. In: *Infrared and Millimeter Waves, Vol. 10: Millimeter Components and Techniques*. Ed. by Kenneth Button. Chap. 1.

[55] J. N. Ullom, P. A. Fisher, and M. Nahum. “Measurements of Quasiparticle Thermalization in a Normal Metal”. In: *Physical Review B* 61 (2000), p. 14839.

[56] J.N. Ullom and P. A. Fisher. “Quasiparticle Behavior in Tunnel Junction Refrigerators”. In: *Physica B: Condensed Matter* 284 (2000), pp. 2036–2038.

[57] F. C. Wellstood, C. Urbina, and J. Clarke. “Hot-Electron Effects in Metals”. In: *Physical Review B* 49.9 (1994), pp. 5942–5955.

[58] A. K. M. Wennberg, S. N. Ytterboe, C. M. Gould, and H. M. Bozler. “Electron Heating in a Multiple-Quantum-Well Structure Below 1 K”. In: *Physical Review B* 34.6 (1986), pp. 4409–4411.

[59] Y. Yoshimura. “A Microstripline Slot Antenna”. In: *IEEE Transactions on Microwave Theory and Techniques* MTT-20 (1972), pp. 760–762.